
**Max-Planck-Institut für Metallforschung**
Stuttgart

# The effect of capillary forces on adhesion of biological and artificial attachment devices

Emerson Jose de Souza

Dissertation
an der
**Universität Stuttgart**

Bericht Nr. 202
September 2007

# The effect of capillary forces on adhesion of biological and artificial attachment devices

Von der Fakultät für Chemie der Universität Stuttgart
zur Erlangung der Würde eines Doktors der
Naturwissenschaften (Dr. rer. nat) genehmigte Abhandlung

Vorgelegt von
**Dipl. Phys. Emerson Jose de Souza**
aus Sao Paulo, Brasilien

| | |
|---|---|
| Hauptberichter: | Prof. Dr. phil. Eduard Arzt |
| Mitberichter: | Prof. Dr. rer. nat. Joachim P. Spatz |
| Tag der mündlichen Prüfung | 06.09.2007 |

Institut für Metallkunde der Universität Stuttgart
und
Max Planck-Institut für Metallforschung Stuttgart

Stuttgart, September 2007

***He has made everything beautiful in its time. He has also set eternity in the hearts of men; yet they cannot fathom what God has done from beginning to end. I know that there is nothing better for men than to be happy and do good while they live.***

**(Ecclesiastes, 3:11-12)**

***Modern science cannot answer as many questions as we would like,***
***but it can extend our eagerness for knowledge***
***and show us how strange and exciting nature can be***
***just below the surface of observable things.***

## Acknowledgements

There are many people, to whom I would like to express my sincere words of acknowledgments but I am sure that the subjective expressions will never allow me to reflect the exact feeling that I have when I thank them. I will try.

I thank Prof. Dr.phil. E. Arzt, for the opportunity he gave me to work in his group at the Max Planck Institut in Stuttgart for Metals Research and for the fascinating subject of research on capillary forces in the context of biological and artificial attachment systems. It gave me not only joy when working on it, but opened doors and new horizons for investigations in many others fields. I thank him also for his friendly way to motivate me, disposability for talking and many fruitful discussions whenever I needed him. I always felt free to discuss my ideas with him and he always guided me without changing my own creativity.

I am also very grateful to Dr. C. Mohrdieck for her immediate supervision of my studies, her interest and curiosity on the details of every sentence that I wrote, not neglecting any calculation or result that I obtained and supporting my motivation over these three years with her endless patience. I thank her also for many technical help in different situations. I thank Dr. M. Brinkmann for the many discussions that we conducted per telephone, for his orientations, critics and important help on the development of the model. I thank him for the good moments of work that he promoted with his friendly way when I was in Göttingen.

I also thank Prof. Dr. A. Crosby of the University Massaschussetts, Amherst, MA, USA, for the collaboration with his group to perform experimental investigations of capillary forces. I thank him for his help and inspection in the Laboratory when I performed the experiments, and not only for the professional support but also for the good time that he offered me during my stay in Amherst.

I am grateful to Prof. J. P. Spatz for his interest in my work and for being a member of the advisor committee of this thesis.

I thank Dr. S. Gorb who was the first to be interested in my studies before I started my PhD and who practically introduced me to the Arzt- Department through his enthusiastic discussions about gecko adhesion and Prof. Dr. R. Spolenak for his interest and assistance during the beginning of my investigations.

I could never forget any member of the Department Arzt, who helped me a lot with their smile providing a wonderful atmosphere of work and their indirect help, which became essential in the success of my research. In particular, I thank also Christian Greiner for the nice time that we shared together in the same office, for the many small good things of our daily work, which we sometimes do not realize once, but remember when we are

far away. I learned a lot about dry adhesion and we enriched each other's knowledge with many fruitful discussions.

Besides the people that I encountered during the doctoral work, I remember with happiness in my heart those who helped me to get here. Thus, I am very grateful to Dr. med. Sabine Neiss and Prof. Dr. med. Wolfram Neiss for supporting my immigration from Brazil to Germany, for their advise and many beautiful moments that we spent together making me feel among them and their children as in my own family.

I also thank Prof. Dr F. Krause, professor for mathematics of the University of Wuppertal, who was always available to me at any time and any circumstance during the beginning of my graduation, with his ceaseless energy explaining n-times one and the same subject of physics or mathematics. It was very difficult for me to work for my living and to study simultaneously, but Prof. Krause found time to motivate and help me always when he realized that I was getting very tired.

Tambem agradeco o Paulo Moreno, que confiou no meu semblante e riscou se pelo meu bem em um momento da minha vida quando ninguem pode ajudar me. Tambem agradeco a familia Ferreira, pelo carinho e amor que sempre recebi naquela casa, pelos varios finais de semana felizes que passamos juntos depois do santo culto, assim como tambem agradeco o Ruben Marinho, pessoa que contribuiu significantemente para a minha felicidade durante os meus anos de graduacao e pelas muitas viajens de fim de semana que fizemos junto para a reuniao de mocidade na Franca, momentos que nunca mais esquecerei.

Impossivel esquecer o agradecimento aos meus pais Jose De Souza e Bertina Figueira que com pouca condicao concedeu me tudo o que eu precisava durante a minha infancia: o amor! Eu curti muita alegria como crianca e mesmo sei muito conhecimento eles sempre deram suporte para a minha fantasia, sem a qual eu nao chegaria onde cheguei hoje. Agradeco por terem sido otimo exemplo de boa conduta, carisma, coragem, esperanca e fe.

I thank also my girlfriend Lida Ghassemzadeh, who gave new light and color in my life with her wonderful smile. We shared difficult and good times and she has been my right hand in everything so that I cannot possibly say in few words how much I would like to thank her.

Now, to Him who has the power to do much more than we, beyond what we can imagine and construct by our hands, according to His spirit inside us, to Him I am grateful for the inspiration and strength during my whole life and in particular for His help during my doctoral work.

# Index

INDEX ..... 7

ABSTRACT ..... 10

SYMBOLS AND ABBREVIATIONS ..... 14

1 INTRODUCTION ..... 15

**1.1 Biological Motivation ..... 15**

**1.2 Literature review and missing investigations ..... 16**

1.2.1 Literature review ..... 16

1.2.2 Missing investigations ..... 21

**1.3 Basic concepts of capillarity ..... 23**

2 ENHANCEMENT OF CAPILLARY FORCES BY MULTIPLE LIQUID BRIDGES ..... 27

**2.1 Abstract ..... 27**

**2.2 Introduction ..... 27**

**2.3 Methods ..... 31**

**2.4 Results ..... 33**

2.4.1 Capillary force as a function of distance $d$ and contact angle $\theta$ ..... 33

2.4.2 Capillary force as a function of number of bridges $n$ and contact angle $\theta$ ..... 34

2.4.3 Required substrate area and stress ..... 38

2.4.4 Work of separation ..... 41

**2.5 Discussion ..... 43**

2.5.1 Capillary force as a function of distance and contact angle ..... 43

2.5.2 Capillary force as a function of the number of bridges and the contact angle ..... 43

2.5.3 Minimum contact area and stress ..... 45

2.5.4 Work of separation ..... 46

2.5.5 Stability of multiple bridges ..... 46

2.5.6 Comparison with biological systems and with van der Waals forces ..... 48

**2.6 Conclusions ..... 51**

## 3 CAPILLARY FORCES BETWEEN CHEMICALLY DIFFERENT SUBSTRATES .53

**3.1 Abstract** ..... **53**

**3.2 Introduction** ..... **53**

**3.3 Methods** ..... **54**

**3.4 Results** ..... **55**

3.4.1 Review of the symmetric case: $\theta_1 = \theta_2$ ..... 55

3.4.2 Effect of contact angle asymmetry: $\theta_1 \neq \theta_2$ ..... 56

3.4.3 Stability and rupture of liquid bridges ..... 61

3.4.4 Application of the model to experiments ..... 63

**3.5 Discussion** ..... **66**

3.5.1 Review of the symmetric case: $\theta_1 = \theta_2$ ..... 66

3.5.2 Effect of contact angle asymmetry: $\theta_1 \neq \theta_2$ ..... 67

3.5.3 Stability and rupture of liquid bridges ..... 69

3.5.4 Application of the model to experiments ..... 69

**3.6 Conclusions** ..... **70**

## 4 EFFECT OF CONTACT ANGLE HYSTERESIS ON THE MEASUREMENT OF CAPILLARY FORCES ..... 71

**4.1 Abstract** ..... **71**

**4.2 Introduction** ..... **71**

**4.3 Methods** ..... **73**

4.3.1 Theoretical model ..... 73

4.3.2 Experimental method ..... 75

**4.4 Results** ..... **78**

4.4.1 Measurement of capillary forces between two parallel plates ..... 78

4.4.2 The effect of contact angle hysteresis ..... 80

4.4.3 Comparison between capillary force and contact angle methods ..... 81

**4.5 Discussion** ..... **82**

4.5.1 Measurement of capillary forces between two parallel plates ..... 82

4.5.2 The effect caused by the contact angle hysteresis ..... 83

4.5.3 Comparison between force and standard methods ..... 84

4.5.4 Volume evaporation and viscosity ..... 85

**4.6 Conclusions** ..... **86**

**5 CAPILLARY FORCE BETWEEN SPHERE AND PLATE** ..... **87**

**5.1 Abstract** ..... **87**

**5.2 Introduction** ..... **87**

**5.3 Methods** ..... **89**

**5.4 Results** ..... **90**

5.4.1 Force versus displacement for fixed sphere radii ..... 90

5.4.2 Force versus radius for fixed separations ..... 94

5.4.3 Laplace pressure and surface tension for flat and spherical geometries ..... 96

5.4.4 Extended maps of multiple liquid bridges ..... 100

**5.5 Discussion** ..... **103**

5.5.1 Forces-displacement curves for large and small separations ..... 103

5.5.2 Fitting results ..... 105

5.5.3 Laplace pressure and surface tension for flat and spherical geometry ..... 105

5.5.4 Map of total force and stress ..... 107

**5.6 Conclusions** ..... **108**

**6 SUMMARY AND OUTLOOK** ..... **110**

**DEUTSCHE ZUSAMMENFASSUNG** ..... **114**

**REFERENCES** ..... **124**

**APPENDIX** ..... **133**

**Emerson Jose de Souza:**

**The effect of capillary forces on adhesion of biological and artificial attachment devices**

Institut of Physical Metallurgy, University of Stuttgart and

Max Planck Institute for Metals Research, Stuttgart, 2007

# Abstract

The presence of a liquid meniscus can cause far greater adhesion between a particle and a surface than occurs under dry conditions. Recent studies on biological attachment systems have highlighted the unique and important effect of liquid capillarity at the micro- and nanometer scale. The results demonstrate that macroscopic considerations of the classic meniscus theory must be modified to take into account new scaling laws and geometric relationships. A general description of wetting and capillary condensation as it applies to interfaces of small scales and to arbitrary substrates is clearly desirable but remains an unsolved challenge.

In this work, I have performed numerical simulations of wet adhesion under less restrictive conditions then has been done before. In particular, I calculated the capillary force as a function of the distance between two substrates for the general case of different properties and different geometries of the substrates. The results are in excellent agreement with analytical results and with measurements of the capillary force. They allow us to propose a novel, effective method to evaluate the contact angle hysteresis of a liquid bridge between arbitrary substrates. The numerical calculations also include the effect of contact splitting which has proven to be a powerful mechanism in many biological attachment systems that are based on dry adhesion. Our results show that this mechanism does in principle also apply

to wet adhesion and that splitting of one large bridge into many smaller ones enhances the capillary forces for all possible contact angles. This results in new scaling laws of the capillary force as a function of the number of liquid bridges. They predict, for example, an unexpected maximal force for moderately hydrophilic surfaces (i.e. contact angles around 70 degrees) and a maximal force per contact area for cylindrical bridges. These novel scaling laws lead to a deeper basic understanding of wet adhesion and can also serve as an important guideline as to how artificial attachment devices can be engineered to have specific properties.

**Emerson Jose de Souza:**

**The effect of capillary forces on adhesion of biological and artificial attachment devices**

Institut of Physical Metallurgy, University of Stuttgart and

Max Planck Institute for Metals Research, Stuttgart, 2007

# Abstract

Eine flüssige Brücke kann zwischen einem Teilchen und einer Oberfläche eine weitaus größere Haftkraft vermitteln als dies in trockenem Zustand der Fall ist. Arbeiten über biologische Haftsysteme haben die wichtige Rolle dieser Kapillarkraft in Mikro- und Nanometer großen Dimensionen hervorgehoben. Die Ergebnisse machen deutlich, dass das makroskopische Bild der klassischen Theorie flüssiger Menisci modifiziert werden muss und neue Skalierungsgesetze sowie Geometrieeffekte einschließen muss. Eine allgemeine Beschreibung von Benetzungsphänomenen und Kapillarität, die auch in kleinen Dimensionen und für beliebige Substratoberflächen Gültigkeit hat, ist zwar sehr wünschenswert aber noch nicht realisierbar.

In der vorliegenden Arbeit präsentiere ich numerische Simulationen der Haftung basierend auf Kapillarität für allgemeinere Bedingungen als dies bisher getan worden ist. Dazu gehört, dass die Kapillarkraft als Funktion des Abstandes zwischen zwei Substraten für den allgemeinen Fall berechnet wurde, dass die Substrate unterschiedliche Eigenschaften und unterschiedliche Geometrien besitzen. Die Resultate stimmen hervorragend mit analytischen Ergebnissen überein und mit Messungen der Kapillarkraft. Sie gestatten uns, eine neue, effektive Methode vorzuschlagen, um die Hysterese der Kontaktwinkel einer flüssigen Brücke zwischen beliebigen Substraten zu bestimmen. In den Simulationen wird auch das

Phänomen des Aufspaltens eines Kontaktes (contact splitting) in mehrere untersucht, das als wichtiger Haftmechanismus in vielen trockenen biologischen Systemen identifiziert worden ist. Unsere Ergebnisse zeigen, dass dieser Mechanismus prinzipiell auch in kapillargestützter Haftung auftritt und dass die Aufspaltung einer flüssigen Brücke in mehrere kleinere zu einer Erhöhung der Kapillarkraft für alle möglichen Kontaktwinkel führt. Daraus resultieren neue Skalierungsgesetzte der Kapillarkraft als Funktion der Anzahl der flüssigen Menisci. Sie sagen z.B. voraus, dass die Kraft ein unerwartetes Maximum für schwach hydrophile Substrate (d.h. Kontaktwinkel ungefähr 70°) aufweist und die Kraft pro Kontaktfläche maximal ist für zylindrische Brücken. Diese neuen Skalierungsgesetze führen zu einem tieferen Verständnis der Haftung basierend auf kapillaren Effekten, und sie können auch als Grundlage benutzt werden, um künstliche Haftsysteme so zu konstruieren, dass sie bestimmte Eigenschaften besitzen.

# Symbols and Abbreviations

## Symbols:

| | | |
|---|---|---|
| $\gamma_{lv}$ | Surface tension energy between liquid and vapor phases | $[N/m^2]$ |
| $\gamma_{ls}$ | Surface tension energy between liquid and solid phases | $[N/m^2]$ |
| $\gamma_{sv}$ | Surface tension energy between solid and vapor phases | $[N/m^2]$ |
| $A_{lv}$ | Area between the liquid-vapor phases | $[m^2]$ |
| $A_{ls}$ | Area between the liquid-solid phases | $[m^2]$ |
| $A_{sv}$ | Area between the solid-vapor phases | $[m^2]$ |
| E | Absolute total interfacial energy | $[N/m^2]$ |
| F | Absolute total force | [N] |
| D | Absolute distance | [m] |
| V | Volume of the liquid bridge | $[m^3]$ |
| s | Length scale set by the radius of a liquid sphere of volume V | [m] |
| $\theta$ | Contact angle of a droplet on a solid surface | [Deg] |
| $R_1$ , $R_2$ | Principal radii of curvatures of the liquid bridge | [m] |
| H | Mean curvature | [1/m] |
| $\Delta P$ | Laplace pressure | [1/m] |
| $R_{sub}$ | Liquid-solid contact radius on the flat substrate | [m] |
| $R_{sph}$ | Liquid-solid contact radius on the sphere | [m] |
| R | Radius of a sphere | [m] |
| y(x) | Parameterization of the surface profile | |
| $l_{cap}$ | Capillary length | [m] |
| $\Delta\rho$ | Difference between the liquid and vapor densities | $[Kg/m^3]$ |
| n | Number of liquid bridges | |

# 1 Introduction

## 1.1 Biological Motivation

Biomimetic concepts and their transfer to technical applications have become an increasingly important field of research during recent years. If it is possible to understand how functional mechanisms operate in nature and which design principles they employ, it may also be possible to replicate these principles in artificially made constructions.

Biological attachment systems constitute one example, among many others, of a natural functional system that is intensely studied in an attempt to copy its functional mechanisms in order to design and fabricate highly adhesive technological surfaces. The fact that different kinds of animals stick to a large variety of different surfaces requires optimized attachment organs that allow these animals not only to attach but also to detach fast and efficiently. To understand how this is accomplished is a very interdisciplinary field of research [1, 2] that involves different types of interactions between the organs and the substrates that act at different length and time scales. The study of these interactions has already triggered many subsequent investigations such as for example the patterning of functional polymeric surfaces or the study of smart polymeric structures.

Several recent studies have highlighted the contribution of capillarity, i.e. of wet adhesion, to the adhesion performance of some animals. Examples comprise the mm-sized adhesion pads of tree frogs [3-5], the µm-large attachment organs of flies [6-8] and the nm-scale hair-like spatulae with which geckos adhere to surfaces [9, 10]. Even though geckos are able to stick to hydrophobic surfaces, their attachment performance has been shown to be influenced by air humidity [11]. This finding suggests that a few monolayers of water that are always present on natural surfaces are sufficient to initiate the formation of liquid menisci between the animals' attachment organs and the substrate. To what extend these menisci contribute to the total

adhesion force of the animals is, however, unknown. Although well established models of dry molecular adhesion exist [12], a coherent description of capillarity and wetting phenomena at the nanometer scale is still missing. Such a description is necessary, however, to fully understand – and possibly mimic - the attachment mechanisms in animals and plants.

In this work, I combine numerical and experimental investigations of the capillary force to modify and enlarge the classical macroscopic picture of the theory of liquid menisci. Particular emphasis is put on the role of size effects and geometric conditions in capillarity since these are believed to be important parameters in natural adhesive systems. The results of my studies suggest new scaling laws of the capillary force and also comprise a novel experimental technique to measure, and thus to verify, the theoretical findings. In view of natural attachment systems, the results allow to make some interesting predictions about their functional mechanisms.

## 1.2 Literature review and missing investigations

### 1.2.1 Literature review

Because of the large body of literature on capillarity the following paragraph on literature is subdivided into several sections. The first one contains a short chronological overview over the development of research on capillarity and discusses some fundamental aspects of pioneering studies. Subsequent sections focus on the role of different geometrical configurations of the substrates that are related to our studies presented in chapters 2 to 5.

- **Chronological overview**

Capillary phenomena are known for a long time and are a multidisciplinary field of research. The mathematician Brook Taylor [13] first described the ascension of water between two glass

plates and gave an approximation of its shape in terms of hyperbolic functions. Later, Segner [14] introduced the notion of surface tension to explain the shape of a liquid interface. Laplace [15] created a quantitative basis for these ideas and related the mean curvature of a liquid-air interface to the pressure difference between the adjacent phases. In the absence of gravity, the liquid-air interface has a constant mean curvature. A second equilibrium condition is due to Young [16] and Dupre: The tangential components of all surface tensions acting on a three-phase contact line (between liquid, solid and air) have to balance in mechanical equilibrium. As a consequence, the liquid-air interface has to form a certain contact angle with the substrate which is fixed by the relative values of the respective surface tensions.

Gauss [17] first characterized the shape of a mechanically equilibrated liquid-air interface as having a minimal area determined by the interfacial and gravitational energies. Stable equilibrium configurations are identified with local minima of the total energy, which provides the basis for robust numerical schemes to compute equilibrium shapes of a liquid interface. It can be shown by use of variational calculus that any minimum-energy configuration of a liquid interface satisfies the condition of Laplace and Young-Dupre. Statements about the stability of a configuration, however, cannot be inferred from the conditions of mechanical equilibrium by Laplace and Young-Dupre. It may happen that a liquid shape is mechanically stable but represents a saddle point in the energy landscape. The stability of such a configuration has to be determined by further criteria, for instance, by use of the second variation of the energy.

Delaunay [18] first constructed the complete set of surfaces of revolution bearing a constant mean curvature. The generating curves have been termed unduloids and nodoids according to their wavy, and curly self-intersecting shapes, respectively. Undoloid and nodoid surfaces make up the family of Delaunay surfaces which contain the catenoid, the cylinder, and the

sphere as special limiting shapes. All these shapes can be employed to describe liquid bridges between parallel and chemically homogeneous plates in the absence of gravity. Plateau [19, 20] confirmed experimentally that shapes of a liquid bridge between two rings correspond qualitatively to those proposed by Delaunay and showed that the maximum length of a stable uniform cylinder of liquid roughly equals three diameters.

The literature on capillarity increased dramatically after these fundamental works. Besides constructing possible equilibrium shapes of liquid droplets and computing the Laplace pressure as function of the liquid volume, many scientists became interested in the force exerted between two substrates by means of a liquid bridge. These capillary forces have been investigated extensively for a variety of situations. The non-linearity of the capillary equation in combination with the variety of substrate geometries leads to a large number of particular solutions. In the following review, we will focus solely on literature dealing with theoretical calculations of liquid bridges between two solid plates with free contact lines characterized by the equilibrium contact angles between the liquid and the plates. We also discuss some experimental works to compare standard models with realistic results.

- **Models for plate-plate geometries**

Concus and Finn[21-24] performed the first rigorous mathematical study of the capillary equation for neutrally buoyant conditions and provided a proof for the existence of certain classes of solutions. In particular, they proofed the existence of a rotationally symmetric solution with an isolated singularity and discussed the procedure for constructing such a solution and an asymptotic power expansion for it. They mention that unduloids, which may describe the surface profile of a stretched liquid bridge, can be generated by rolling an ellipse without slip along an axis and rotating the resultant curve around this axis.

Vogel [25-27] and Langbein [28-30] formulated criteria for the stability of rotationally symmetric liquid bridges for arbitrary contact angles. A more detailed description of their studies is given in chapter 3. Lowry [31-33] gave a complete scheme to classify the local stability of solution branches from the corresponding curves in the pressure-volume plane. Local stability at fixed liquid volume, for instance, is lost or gained when passing a turning point in the pressure-volume diagram. All of the mathematical analyses mentioned above had fundamental impact on future work, but they are difficult to apply to experiments.

The stability of liquid bridges between coaxial circular disks was extensively investigated for boundary conditions with prescribed contact radii [34-38]. In this case, the equilibrium contact angle is not determined by surface tensions. Later investigations made by Fortes [39] and Carter [40] considered a free contact line on homogeneous and parallel substrates and obtained force-displacement curves for arbitrary but identical contact angles. Later, Zhou [41, 42] extended the results of Finn and Vogel showing that a unique stable liquid bridge exists between two plates of given separation for any value of the contact angles and for any liquid volume greater than or equal to a critical volume. Besides, she proved that Carter's stability criterion is also true for the general case in which the two contact angles are different.

- **Models for sphere-sphere and plate-sphere geometries**

Calculations of the capillary force have also been carried out for a liquid bridge between two spheres [43-46] and between a sphere and a plate [12, 47-69]. These geometries were frequently used in experimental studies since they are easier to design than perfectly flat and parallel plates. Solutions were obtained by applying different approximations and only few exact solutions of the capillary equation can be found in the literature, for instance in [70, 71] for sphere-sphere-configurations and in [72-74] for sphere-plate configurations. These results are either expressed in terms of elliptical integrals or dimensionless parameters, which is not convenient for the

analysis of experimental data. Consequently, most authors prefer to present their own calculation, which has led to a large variety of different approximations that often refer to special cases and conditions only.

Based on the investigations of McFarlane and Tabor [47] and O' Brien and Hermann [75] numerous research groups studied the effect of capillarity in the context of humidity-dependent forces [48-50, 54, 76] and measurements of capillary adhesion and friction by atomic force microscopy [64, 77-83]. Further expressions were proposed based on the circular approximation of the curvature of the liquid-vapor interface [60-62, 84-88] and on numerical computations of the curvature [72-74, 89]. The circular approximation was shown to be valid for small liquid bridges [72-74, 89]. Furthermore, the sphere-plane geometry was also frequently used to model capillary forces on rough surfaces [63, 90-97].

- **Experimental investigations**

After the experiments of Plateau [19, 20], capillarity gained attention in studies of adhesion between two bodies, which is a subject of large technological and industrial importance. Derjaguin [43-45] belongs to those who initialized orderly investigations of adhesion and calculated the meniscus force for two elliptical bodies, and in particular for two spheres with arbitrary contact angles between the spheres and the meniscus. At the same time, Stone [98] measured the influence of humidity on the adhesion between glass beads and suggested that the adhesion force depends on the surface tension of a thin liquid film between the beads, but he did not explicitly mention the formation of a liquid meniscus. Based on these ideas, McFarlane and Tabor [47] approximated the adhesion force between a sphere and a flat surface by $F = 4\pi\gamma_{lv} \cdot R\cos\theta$, where $R$ is the radius of the sphere, $\gamma_{lv}$ is the surface tension of the liquid-vapor interface and $\theta$ is the contact angle between the liquid and the substrates. Although the authors stressed that this equation applies strictly only if the thickness of the liquid film and the contact angle are very small, it became a standard formula that is widely referenced and

used in many different studies [12, 48, 49]. Israelachvili et al. [48], for example, used a surface force apparatus and observed that the formula by McFarlane and Tabor holds for a meniscus of cyclohexane in a relative humidity $RH > 0.1$ while for water it only holds for $RH > 0.9$. Besides the investigations of condensation, Maeda and Israelachvili [51, 52] also used the surface force apparatus to investigate the evaporation of hexadecane and dodecane and discussed the thermodynamic and mechanical stability of liquid bridges as well as the applicability of Kelvin's equation [99] of thermodynamic stability to very small liquid menisci. They compared their experiments to the numerical solutions of the capillary equation proposed by Willet [46] for liquid bridges between two spheres and found good agreement for the calculated and measured rupture distances.

The experiments made in [48, 49] were later reexamined by Christenson [50] who observed that the formula by McFarlane und Tabor only holds for $RH > 0.7$ and that at lower vapor pressures the adhesion force decreases gradually to its lower limit of dry adhesion which is given by $F = 4\pi\gamma_{lv} \cdot R$. This finding was also supported by Rabinovich [53]. Christenson carried out additional investigations [54, 55, 100] of capillary condensation of different solvents, investigated the kinetics of condensation [56] and performed several analyses of condensation for other solvents and mixtures of solvents [57-59]. Many experimental investigations have been performed in the context of different geometries [43-46, 68, 70-74], environmental conditions [47-59, 67, 101], and materials [60-64, 66, 69].

### 1.2.2 Missing investigations

Different models have been proposed to evaluate the force of one liquid bridge, but little attention has been paid to the case of multiple liquid bridges. The reason seems to be that the force of many bridges is intuitively assumed to be a multiple of the force of one bridge. However, the surface properties of the substrates have to be taken into account and it is not

clear how they affect the force exerted by multiple bridges. In this work I have therefore for the first time numerically calculated the capillary force as a function of the number of liquid bridges, their size and the contact angles that they form at the substrates. The dominant question to be answered is: is there a size effect in wet adhesive systems similar to the one that has been evaluated both theoretically [102] and experimentally [103] in dry adhesive systems? The results are presented in chapter 2.

Frequently, liquid bridges are assumed to exist between identical substrates. Consequently, most of the calculations and experimental studies were performed under the condition of equal contact angles at both substrates. But in natural and also in artificial systems this is rarely the case and a general understanding of how the capillary force is influenced by the chemistry of different substrates is lacking. I address the problem of asymmetric configurations in chapter 3 and evaluate the force between a very hydrophilic and a very hydrophobic substrate and the stability of the connecting liquid bridge. The answer to such questions helps to understand realistic cases and to assess the validity of models based on idealized assumptions.

Another aspect that is often neglected in the literature is the fact that contact angles can change depending on whether a liquid bridge is stretched or compressed, which is designated by the terms “dynamic contact angles” or “contact angle hysteresis”. This phenomenon plays a fundamental role in experiments, because it implies that the capillary force between two substrates can also depend on the *direction* of the relative motion of the substrates with respect to each other. Conversely, measurement of the capillary force for different relative motions of the substrates can be used as a means to determine in what way the surface properties change depending on whether the liquid meniscus is stretched or compressed. In a collaboration with Prof. A. Crosby from the University of Massachusetts/ Amherst, I

designed an experiment to measure the contact angle hysteresis for different substrates as well as the capillary force of a liquid bridge between plates. The experiment and the results and their comparison to the numerical force calculations are presented in chapter 4.

Another very important parameter affecting the capillary force is the geometry of the substrates. Although configurations of a liquid bridge between a plate and a sphere have been studied extensively, it is not known, for example, for which radius of the sphere, relative to the volume of the liquid bridge, the force-distance curve of a plate-sphere configuration corresponds to that of a plate-plate configuration. In chapter 5 I therefore present a quantitative analysis of this correspondence that provides insight into how large the geometric effect of a curved substrate is. I also study the effect of multiple bridges and compare the results to the situation of multiple bridges between two plates. This comparison allows to make novel and interesting suggestions concerning the adhesion on rough surfaces.

## 1.3 Basic concepts of capillarity

Two mathematically equivalent concepts can be used for describing and solving Problems related to capillarity: I) the older one is based on the surface tension as formulated by Laplace, Young and Dupre and II) the second one is Gauss'es concept of a liquid surface with a minimum energy for a given, fixed liquid volume. Therefore, a mechanically stable liquid bridge can be constructed either from a local equilibrium of forces acting on the liquid-vapor interface or by a direct minimization of the total interfacial free energy. This minimum of the total free energy is equivalent to a balance of forces under the condition that no irreversible energy losses occur such as losses due to the viscosity of the liquid, for example. Furthermore, the energy minimization requires the constraint of a constant volume. The equivalence of both methods, which we will briefly describe below, holds for all phenomena in capillarity.

- **The surface tension**

The capillary force can be expressed by the balance of forces on each element of the liquid-vapor interface. Each such element experiences a fluid-static pressure and a surface tension along its perimeter. The condition for a local mechanical equilibrium leads to the frequently used capillary equation [23, 104, 105] given by:

$$\Delta P = \gamma_{lv}\left(\frac{1}{R_1}+\frac{1}{R_2}\right) = \gamma_{lv}\left(\frac{y''}{(1+y'^2)^{\frac{3}{2}}} - \frac{y'}{x(1+y'^2)^{\frac{1}{2}}}\right), \tag{1.1}$$

where $\Delta P$ is the Laplace pressure that corresponds to the difference between the pressure in the vapor and in the liquid, $\gamma_{lv}$ is the surface tension of the liquid-vapor interface, $1/R_1$ and $1/R_2$ are the principal curvatures of the liquid bridge describing the curvatures along the circumference and along the meridian of the bridge, respectively and $y(x)$ is the parameterization of the surface profile of the liquid bridge along its meridian. For a constant mean curvature, $(1/R_1+1/R_2)$, the pressure difference does not depend on local properties of the liquid-vapor interface and for a given contour $y(x)$ of the bridge, the principal radii can also be expressed analytically [104]. As can be seen from Eqn. (1.1), the mean curvature of a rotationally symmetric bridge is given by a nonlinear partial differential equation of second order that describes the mechanical equilibrium between the bulk phases and the liquid-vapor interface in the absence of gravitational forces.

The curvature of a liquid-vapor interface is positive if the interface is convex when viewed from within the liquid. In the case of liquid spheres or liquid bridges between hydrophobic substrates, both curvatures, $1/R_1$ and $1/R_2$, are positive. The curvature is negative for concave surfaces. This situation occurs in pores, where $1/R_1$ and $1/R_2$ are negative while for liquid bridges between hydrophilic substrates only $1/R_2$ is negative. While the surface tension tries to reduce the curvatures, the Laplace pressure counteracts this tendency. Note that at a saddle

point on the interface the mean curvature and consequently also the Laplace pressure are zero. However, this occurs only at a particular separation between the substrates and for a suitable choice of the contact angles. If the length scale $s=(3V/4\pi)^{1/3}$, set by the radius of a sphere of the same volume $V$ as the liquid bridge, is small compared to the capillary length $l_{cap}=(\gamma_{lv}/g\Delta\rho)^{1/2}$ (where $g$ is the acceleration of gravity and $\Delta\rho$ the difference between the liquid and vapor densities), the influence of gravity is negligible and the liquid bridge has a constant mean curvature.

The shape of the bridge $y(x)$ can be calculated analytically by integration of Eqn. (1.1). The exact global solution of this equation always leads to expressions given in terms of elliptical integrals [23, 28, 39, 40, 74]. Neumann [106] made for the first time the frequently used circular approximation of the meridional profile of a liquid bridge for small separations of the substrates, which leads to closed solutions. However, this approximation can rarely be applied at large separations, which can be seen by inspection of some of the images in chapter 4.

The total capillary force can be obtained as the sum of forces arising from surface tension ($F_{tension}$) and the Laplace pressure ($F_{Laplace}$) in any plane of the bridge perpendicular to the axis of symmetry. The total force is independent of the particular choice of this plane but the relative magnitude of the two contributions may vary with the position of the plane. Here, we will refer to the limit that the reference plane coincides with one of the two planar substrate surfaces. We obtain for identical contact angles [74, 107]:

$$F_{total}(D) = F_{tension} + F_{Laplace} = 2\pi R(D)\gamma_{lv}\sin\theta + \pi R^2(D)\gamma_{lv}\left(\frac{1}{R_1(D)} + \frac{1}{R_2(D)}\right) \qquad (1.2)$$

where $F_{total}(D)$ is the total capillary force as a function of the distance $D$ between the substrates, $R(D)$ is the radius of the contact area between liquid and substrate and $\theta$ is the contact angle. Note that the principal curvatures and thus the Laplace pressure also depend on the separation between the substrates. Some recent studies are based on Eqn. (1.2) rather than

on Eqn. (1.1), however there is no common practice when it comes to the evaluation of the total capillary force and often it is only described by the contribution of the Laplace pressure neglecting the contribution from the surface tension[12].

- **Minimization of the total free energy**

Most studies on capillary forces are based on the analytical or numerical integration of the capillary equation (Eqn. 1.1) but the overall stability of a liquid bridge can only be determined by minimization of the total free energy. For this reason and to avoid having to use some of the approximations described in the last section, we have chosen the second approach, i.e. the minimization of the total free energy of the liquid bridge, to evaluate the capillary force. This is a flexible method because it allows to study very general situations, such as for example the case of different geometries and different contact angles of the two substrates. The concept of energy minimization is not a local concept, because the increase of the energy in one region of the liquid surface may be overcompensated by a decrease in another region. It can be shown that the capillary equation is equivalent to the Euler-Lagrange [30] equation resulting from the variation of the energy, where the Laplace pressure is equivalent to the Lagrange multiplier λ enforcing a constraint on the liquid volume.

The total energy of a liquid bridge is the sum of three contributions: the liquid-solid $(\gamma_{ls}A_{ls})$, the liquid-vapor $(\gamma_{lv}A_{lv})$ and the solid-vapor $(\gamma_{sv}A_{sv})$ interfacial energies, where $\gamma$ and $A$ denote the respective surface tensions and surface areas. Since the substrate is considered to be rigid, we can assume the total substrate area, $A_s=A_{ls} + A_{sv}$, to be constant throughout the wetting process. Because the total interfacial energy $E$ of the system is determined up to a constant, it can be written in the following way:

$$E = \gamma_{lv}A_{lv} + (\gamma_{ls} - \gamma_{vs})A_{ls}. \tag{1.3}$$

This expression can be calculated using different numerical approaches. In this work, we have used the software package Surface Evolver [108] to calculate $E$, which will be explained in more detail in the following chapter.

# 2 Enhancement of capillary forces by multiple liquid bridges

## 2.1 Abstract

Capillary forces can significantly contribute to the adhesion of micro- and nano-scale objects in biology and technology. In this chapter we study numerically the effect of meniscus size on the force between two homogeneous flat plates for different contact angles. The force distance curves show excellent quantitative agreement with previous investigations. The results for *n* menisci of equal total liquid volume reveal interesting scaling properties and an unexpected maximum force for moderately hydrophilic surfaces (i.e. contact angles around 70 degrees). Further, we calculate the minimum solid liquid area for multiple bridges, the stress (i.e. force per area) and the work required to separate the plates. The results are presented in two dimensional maps, which may be useful in the understanding of biological attachment structures and in the design of artificial contact systems.

## 2.2 Introduction

The first theories of capillary forces were established in the nineteenth century by Young [16], Laplace [15], and Poisson [109], to name some of the early founders of this large field of research. Their studies of the shape of liquid interfaces were based on phenomenological descriptions of the surface tension and on local conditions for a mechanical equilibrium. Gauss [17] introduced the principle of minimal surface energy and established the connection between capillarity and variational calculus. Based on these studies, later theories were refined to include the kinetic theory of matter [110], classical thermodynamics [111] and statistical mechanics of liquid-gas surfaces [112, 113]. This progress led to the concept of surface tension on a molecular basis and to an understanding of phenomena such as the dynamical behavior of condensation and evaporation [104, 105, 114].

One of the many interdisciplinary aspects of capillarity is its effect on adhesion. This topic was initiated by studies of wettability [115-117] that gained momentum when wet adhesion was recognized as a major contributor to hard disk crashes [65]. Recently, investigations of biological attachment systems and their transfer to technological applications have created new interest in the theory of capillarity. Examples that highlight its importance in biological systems are the toe pads of tree frogs [3], and the attachment terminals of some insects like beetles [7, 118], bugs [119], flies [6, 120] and ants [121]. Even the adhesive structures in geckos, which are known to exhibit dry adhesive systems [9, 10], have been shown to be affected by capillarity due to air humidity [11]. For dry adhesive systems, the calculation of adhesion design maps has shown that splitting of one contact element into many finely structured elements can result in enhancement of molecular adhesion [1, 102]. This raises the questions whether a similar size effect also exists in wet adhesive systems and what implications it may have for biological and bio-inspired adhesive systems.

The aim of this work is to explore how finely structured liquid bridges can affect the capillary force between two surfaces. To this end, we apply a numerical method [108] to calculate force-distance curves and shapes of liquid menisci between two substrates. The method is flexible in so far as it allows arbitrary geometries of the substrates to be studied, as well as symmetric and asymmetric configurations of the contact angles between the substrates and the liquid. It has been successfully applied to problems of capillary surfaces [122-124] but not specifically to liquid bridges between parallel plates. We therefore test it first by conducting numerical investigations of one liquid bridge between two rigid plates for different contact angles and compare the results with available analytical results. Subsequently, new calculations are performed by splitting the volume of one bridge into $n$ small bridges and recalculating the force-distance curves.

Before we introduce the applied numerical method in the next section, we briefly review the

state-of-the-art literature on force-distance curves of the capillary force. The capillary force can be expressed as the sum of forces arising from the surface tension ($F_{tension}$) and the Laplace pressure ($F_{Laplace}$) [74, 125]:

$$F_{total}(D) = F_{tension} + F_{Laplace} = 2\pi R_{sub}(D)\gamma_{lv}\sin\theta + \pi R_{sub}{}^{2}(D)\gamma_{lv}\Delta P \tag{2.1}$$

where $F_{total}(D)$ is the total capillary force as a function of the distance $D$ between the substrates, $R_{sub}(D)$ is the radius of the interface between liquid and solid, $\theta$ is the contact angle at the three phase contact line, and $\Delta P$ is the Laplace pressure defined as the pressure difference across the liquid-vapor interface. The Laplace equation [15] relates $\Delta P$ to the mean curvature of the liquid-vapor interface and expresses the mechanical equilibrium between the bulk phases and the curved liquid-vapor interface:

$$\Delta P = \gamma_{lv}\left(\frac{1}{R_1} + \frac{1}{R_2}\right). \tag{2.2}$$

Here, $\gamma_{lv}$ is the surface tension of the liquid-vapor interface and $1/R_1$ and $1/R_2$ are the two principal curvatures at a given point on this interface. Provided gravitational forces are negligible, $\Delta P$ is the same everywhere on the liquid-vapor interface which implies that this interface has a constant mean curvature $H = 1/2\left(1/R_1 + 1/R_2\right)$ in equilibrium.

The total capillary force has been determined both theoretically and experimentally for a variety of idealized conditions. An analytical approximation of the capillary force between identical spheres exists [126]. This approximation was later improved to yield exact expressions for the force and for the neck radius and the volume of a liquid meniscus between the spheres [127]. Experimentally, the force between two spheres has been evaluated as a function of their separation [128]. The geometric configuration of a liquid bridge between a sphere and a plate has also been investigated [73-75, 129]. In the first study, the equation for the surface profile of a liquid bridge with zero contact angles ($\theta_1=\theta_2=0$) is evaluated, while the other two present

approximations of the capillary force for nonzero and different contact angles. A more rigorous description of this case exists [74], but the results are expressed in terms of elliptical integrals and are therefore difficult to interpret.

A commonly used approximation [12] assumes a sphere of radius $R$ in contact with a plane, both with identical contact angles. Under theses conditions the resulting capillary force is:

$$F_{Laplace} \approx 4\pi R\gamma_{lv}\cos\theta\,. \tag{2.3}$$

This equation is frequently used, for example to calculate the capillary force between a flat substrate and the tips of a scanning tunneling [62] or an atomic force microscope [86]. Since it considers only the contribution of the Laplace pressure to the total capillary force, it may not always be applicable.

Analytical calculations of the force-distance relationship for a liquid bridge between two solid parallel plates with arbitrary but equal contact angles at both surfaces have been presented by Fortes [39] and Carter [40]. To test the energy minimization method used in this work, we chose the same geometric configuration as used by Carter [40] and numerically calculated the force-distance curves for the whole range of contact angles. Comparison with Carter's results [40] yields excellent agreement, which justifies the application of this method to new problems of capillary surfaces for which there are no analytical solutions. In spite of the large number of publications dealing with models of the capillary force between substrates of different geometries, a numerical evaluation for one liquid bridge between two planar surfaces has not previously been published.

Forces mediated by multiple bridges have been considered in studies dealing with the effect of surface roughness on adhesion. The contributions to wet adhesion from multiple-asperity

contacts have been evaluated by [63, 130] for different liquid levels. [90] estimated the wettable surface area fraction between rough substrates from the width of the distribution of distances between surface asperities. All studies give approximate expressions for the total adhesive force but do not analyze its functional dependence on the number of the contacts. The present work presents, for the first time, numerical solutions of the total capillary force as a function of the number $n$ of liquid bridges for different contact angles. As a result, an interesting size effect has been discovered theoretically and scaling properties have been evaluated that were not anticipated intuitively.

## 2.3 Methods

We assume two perfectly homogeneous flat substrates with equal contact angles $\theta$ and a constant liquid volume $V$ between them (Figure 2.1).

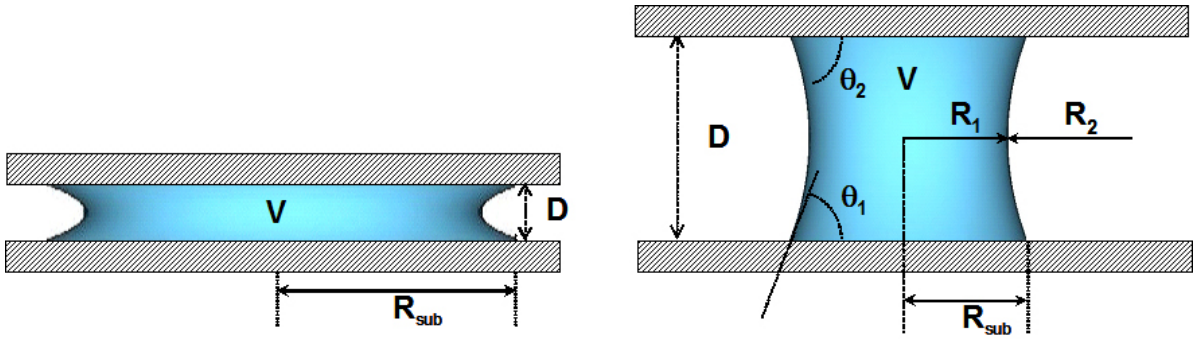


**Figure 2.1**: Schematic illustration of a liquid bridge which wets two planar parallel substrates with fixed contact angles $\theta_1$ and $\theta_2$. If the plates are pulled apart, the distance $D$ between them increases while the radius of the liquid-solid interface $R_{sub}$ decreases and the volume V of the liquid bridge remains constant. For large distances the liquid bridge ruptures. The radii $R_1$ and $R_2$ are the principal radii of a liquid bridge.

When the plates are close together, the liquid-vapor interface is small whereas the liquid-solid contact is large. When the plates are pulled apart, the liquid-vapor contact increases at the expense of the liquid-solid interface. At any moment, the capillary force depends on the

separation $D$ of the substrates, the surface tension $\gamma_{lv}$ of the liquid-vapor interface, $V$ and $\theta$. If the length scale $s=(3V/4\pi)^{1/3}$, set by the radius of a fictional liquid sphere of the same volume $V$ as the liquid bridge, is small compared to the capillary length $l_{cap}=(\gamma_{lv}/g\Delta\rho)^{1/2}$ (where $g$ is the acceleration of gravity and $\Delta\rho$ the difference between the liquid and vapor densities), the influence of gravity is negligible and the liquid-vapor interface of the bridge therefore has a constant mean curvature. The contour of an axially symmetric bridge can be calculated analytically by integration of equation (2.2).

The total energy of a liquid bridge is the sum of three contributions: the liquid-solid $(\gamma_{ls}A_{ls})$, the liquid-vapor $(\gamma_{lv}A_{lv})$ and the solid-vapor $(\gamma_{sv}A_{sv})$ interface energies, where $\gamma$ and $A$ denote the respective surface energies and surface areas. Since the substrate is considered to be rigid, we can assume the total substrate area to be constant throughout the wetting process. Because the total energy $E$ is determined up to a constant, it can be written in the following way:

$$E = \gamma_{lv}A_{lv} + (\gamma_{ls} - \gamma_{vs})A_{ls}. \tag{2.4}$$

In this work, this expression for the total energy of a liquid bridge was minimized using the software package Surface Evolver [108]. The liquid-vapor interface is represented by a mesh of triangles whose total area approximates the value of $A_{lv}$. The area of the wetted substrate is obtained by line integrals along the contact line. The constraint of constant volume is expressed by means of a surface integral over a suitably chosen vector field. With the help of this numerical minimization, it is possible to calculate the capillary force as a function of the separation of the substrates.

To directly compare our results with the analytical ones obtained by Carter [40], we introduce the following normalized quantities:

| | | |
|---|---|---|
| normalized separation: | $d = D/s$ | (2.5a) |
| normalized contact radius: | $r(d) = R_{sub}(d)/s$ | (2.5b) |
| normalized total energy: | $e(d) = E(d)/(\gamma_{lv}s^2)$ | (2.5c) |
| normalized total force: | $f(d) = F(d)/(2\pi\gamma_{lv}s)$, | (2.5d) |

where $R_{sub}$ is the absolute radius of contact between liquid and solid (Figure 2.1) and $F$ the absolute total force exerted by the liquid between the substrates. The forces are obtained from the first derivative of the total energy with respect to distance.

## 2.4 Results

### 2.4.1 Capillary force as a function of distance *d* and contact angle *θ*

Figure 2.2 shows the normalized force as a function of the normalized distance between the substrates for different contact angles.

The forces are attractive (positive) for $\theta \leq 90°$ (as schematically illustrated by liquid bridges with concave shapes in the meridional cross section) and decrease with increasing distances.

In the hydrophobic range the forces are repulsive (negative, bridges with convex shapes in the meridional cross section) for small and slightly attractive for large distances. With increasing values of $\theta$, repulsive forces increase while attractive forces decrease.

The maximum normalized distance, $d_{max}$, for a given contact angle, i.e. the end point of each curve, corresponds to the largest possible separation of the substrates for which the liquid bridge is still stable. Further increase of $d$ will result in rupture of the bridge. We stress that the value of $d_{max}$ depends on the contact angle $\theta$. The data show that in the hydrophilic range rupture occurs at smaller distances for smaller contact angles; for hydrophobic conditions the opposite is true.

Figure 2.2 shows that these force-distance curves (symbols) are in excellent agreement with the analytically calculated ones (solid lines) [40] over the entire range of distances and for all contact angles.

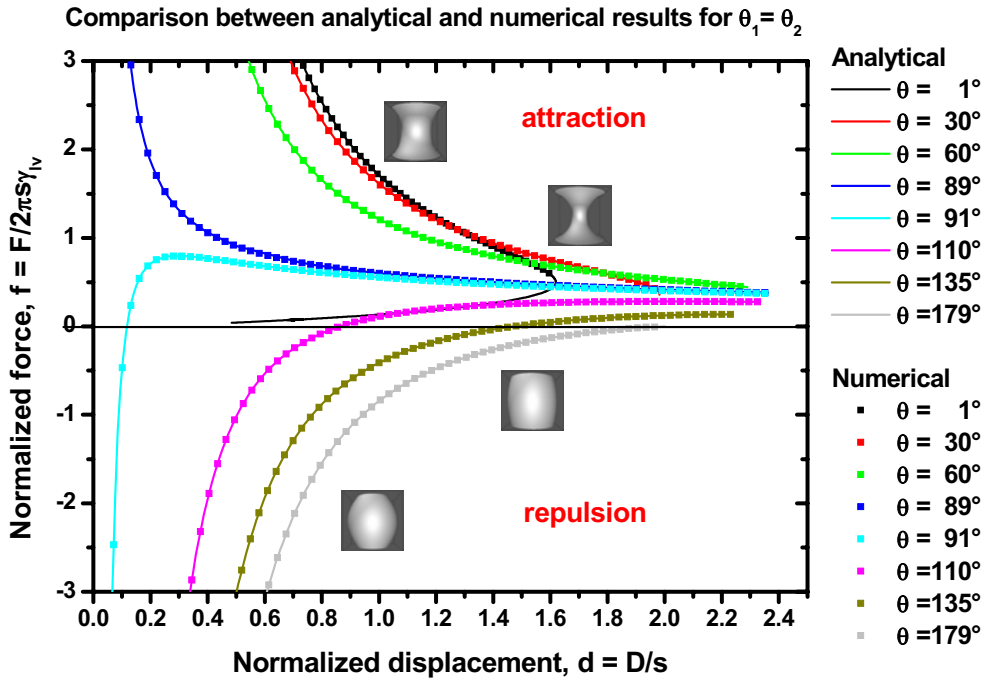


**Figure 2.2**: Force versus displacement for hydrophilic θ≤90° and hydrophobic θ>90° surfaces. In the hydrophilic range the forces are always attractive, they converge to positive infinity if the distances approach zero and rupture occurs at large separations. The forces in the hydrophobic domain are predominantly repulsive but exhibit small attractive contributions for increasing distances. The schematic drawings represent the shapes of liquid bridges for hydrophilic and hydrophobic conditions. Comparison between analytical (solid curves) and numerical (squares) results demonstrate the excellent accuracy of the numerical model.

### 2.4.2 Capillary force as a function of number of bridges *n* and contact angle *θ*

We now consider the effect of splitting one large liquid bridge into *n* smaller bridges, each of volume *V/n* as schematically shown in Figure 2.3.

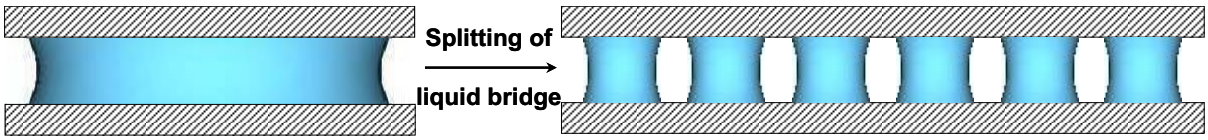


**Figure 2.3**: Schematic of splitting one liquid bridge into n smaller liquid bridges of equal size. The total volume of the liquid and the separation of the substrates are equal in both cases.

In the subsequent calculation it is assumed that the individual bridges do not interact or coalesce. This situation could be realized experimentally by topographical or chemical patterning of the substrates.

To calculate the total force of $n$ liquid non-interacting bridges, we start from the absolute force for one liquid bridge (eqn. 2.5d). If $V$ decreases to $V/n$, the scaling factor $s$ and the normalized distance $d$ change in the following way: $s$ becomes $s_n=s\ n^{-1/3}$ and $d$ becomes $d_n=d\ n^{1/3}$. For $n$ liquid bridges the total absolute force at distance d is therefore given by:

$$F_n(d) = 2\pi \cdot n\gamma_{lv} s_n \cdot f(d_n) = 2\pi \cdot n^{2/3}\gamma_{lv} s \cdot f(d_n) \tag{2.6}$$

Note that the absolute separation $D$ of the substrates has not changed and is the same in $F(d)$ and $F_n(d)$. The dependence of this total force on $n$ and $\theta$ is displayed in Figure 2.4, using $\gamma_{lv}=72.8\ mN/m$ for the water-air interface, $V=1\ \mu l$ and $D=15\ \mu m$.

The results show that the total capillary force increases due to splitting of a bridge for all values of $\theta$. For angles $\theta \leq 50°$, $F_n$ possesses a maximum at some intermediate value of $n$, while for $\theta > 50°$ a monotonic increase with $n$ is observed.

The maximum attainable force, under the conditions assumed, is achieved for $\theta \approx 70°$, $n \approx 9.5x10^5$ and $d=dmax(70°)$. Interestingly, this is not in the very hydrophilic regime but rather in the weakly hydrophilic range. For a fixed separation of the substrates, the point of rupture for a given contact angle determines the maximum number, $n_{max}$, of stable bridges. Its value thus depends on the angle $\theta$.

The information contained in Figure 2.4 can be conveniently displayed in a color map as shown in Figure. 2.5. As axes, we choose the contact angle $\theta$ and the number $n$ of bridges that vary in steps of $\Delta\theta=5°$ and $\Delta n=1$, respectively, in all color maps presented in this work. The parameters $V$, $D$, and $\gamma_{lv}$ are fixed as in Figure 2.4.

The color coding corresponds to different total force values. The continuous lines represent contours of equal force (labeled in Newtons); the heavy black contour marks the transition from attractive to repulsive forces.

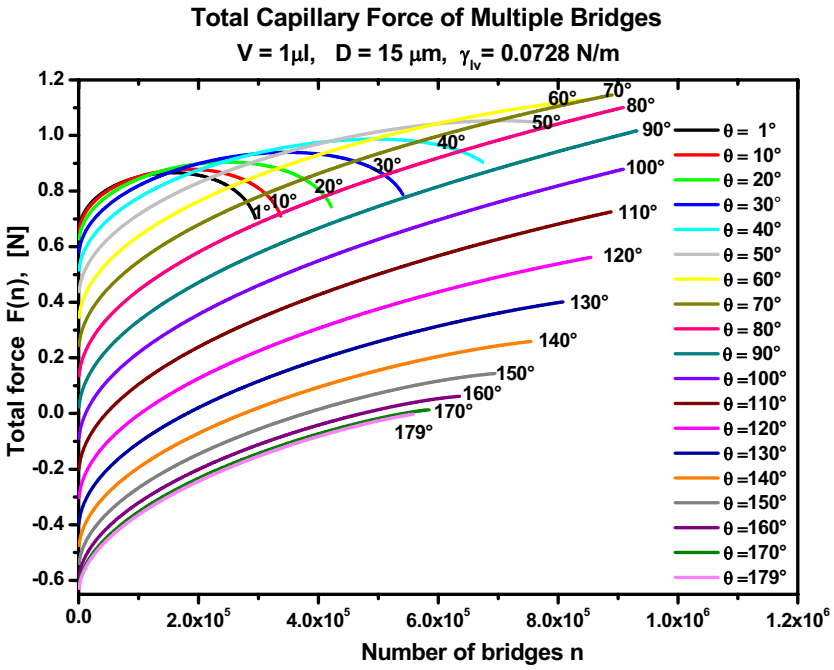


**Figure 2.4**: Total force versus the number of liquid bridges for different contact angles.

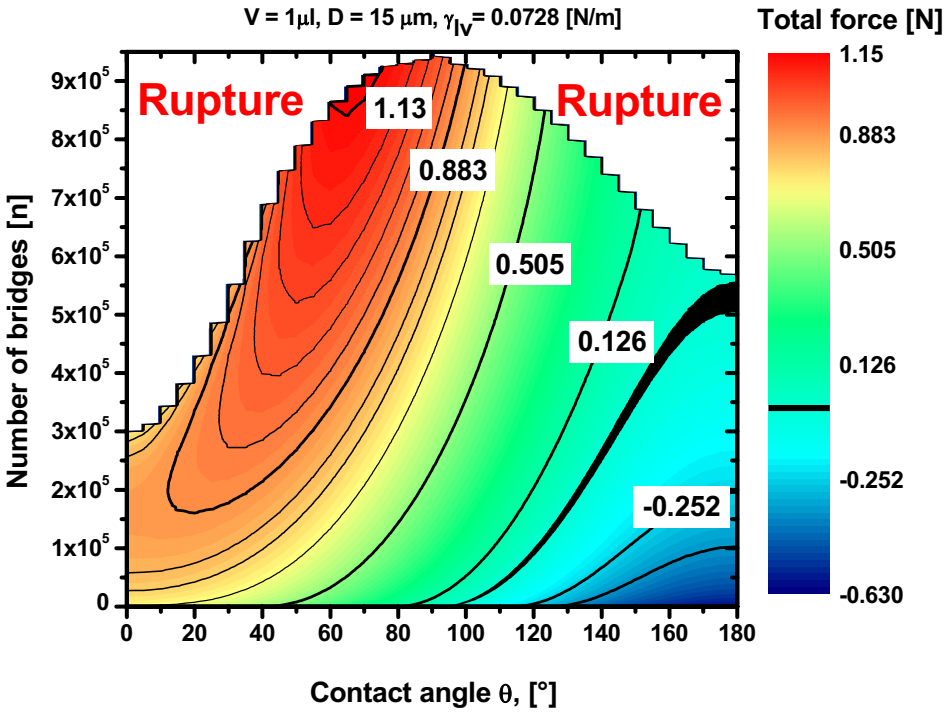


**Figure 2.5**: Map of the total force versus the contact angle $\theta$ and the number of liquid bridges. The black contours are lines of equal force, some of which are labeled in [N] for a better visualization.

The maximum force (red area) reflects the maximum discussed in Figure 2.4. The "landscape" in Figure 2.5 has an interesting topography which will be discussed later.

Variation of the total volume for a constant initial distance shows that the force of multiple liquid bridges is directly proportional to that volume without changing the qualitative behavior of previous results. For a given initial separation, a larger total volume results in a larger number of possible bridges and vice versa. Likewise, the choice of different initial separations does not change the qualitative behavior of the total force, which scales with the initial separation as $F_n \sim D^{-2}$. Equivalent to a decrease in volume, a larger separation leads to fewer possible bridges. We can therefore normalize the total force by $F_n D^2/2\pi\gamma_{lv}V$ and summarize the results in Figure 2.6.

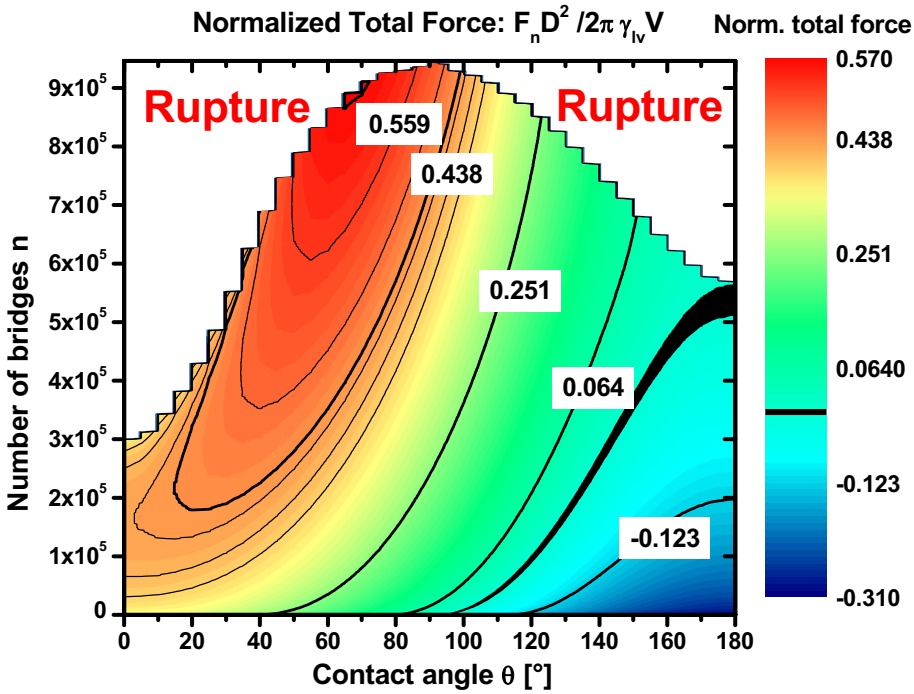


**Figure 2.6**: Total normalized force versus number of bridges and contact angles. $F_n$ is normalized by the initial separation D, total volume V and the surface tension $\gamma_{lv}$ of the liquid-vapor interface. Labels of isolines are dimensionless.

Comparison with Figure 2.5 shows that there is indeed no qualitative change in the results.

### 2.4.3 Required substrate area and stress

- **Map of substrate area**

After subdividing into *n* bridges, it is of interest to know the total area of the bridges projected onto the substrate, which defines the minimum required substrate area. From the numerical minimization of the total energy we directly obtain the radius of the liquid-solid interface $R_{sub}(d)$ and the neck radius $R_1(d)$ as presented in Figure 2.1.

The total area necessary to accommodate *n* liquid bridges is equal to the sum of all small projected areas of each bridge

$$A_n(d) = n\pi \cdot R_n^2(d_n)\,, \tag{2.7a}$$

where
$$R_n(d_n) = R^*(d_n)s_n \tag{2.7b}$$

and
$$R^*(d_n) = R_{sub}(d_n) \text{ for } \theta \leq 90°$$

or
$$R^*(d_n) = R_1(d_n) \quad \text{for } \theta > 90° \tag{2.7c}$$

Eqn. 2.7c reflects the fact that the neck radius of a bridge is larger than its contact radius if $\theta > 90°$: $R_1(d) > R_{sub}(d)$.

Figure 2.7 shows that for a given contact angle $\theta < 90°$, the total area increases as a function of *n* and is maximal at $n_{max}$. For $\theta = 90°$ it is constant and for $\theta > 90°$ it increases slightly (see labeled contour lines in Figure 2.7) due to the convex shapes of the liquid bridges between hydrophobic surfaces.

If the number of bridges is kept constant, the total area decreases as a function of $\theta$ for $\theta < 90°$, is minimal at $\theta = 90°$ and increases with $\theta$ for $\theta > 90°$.

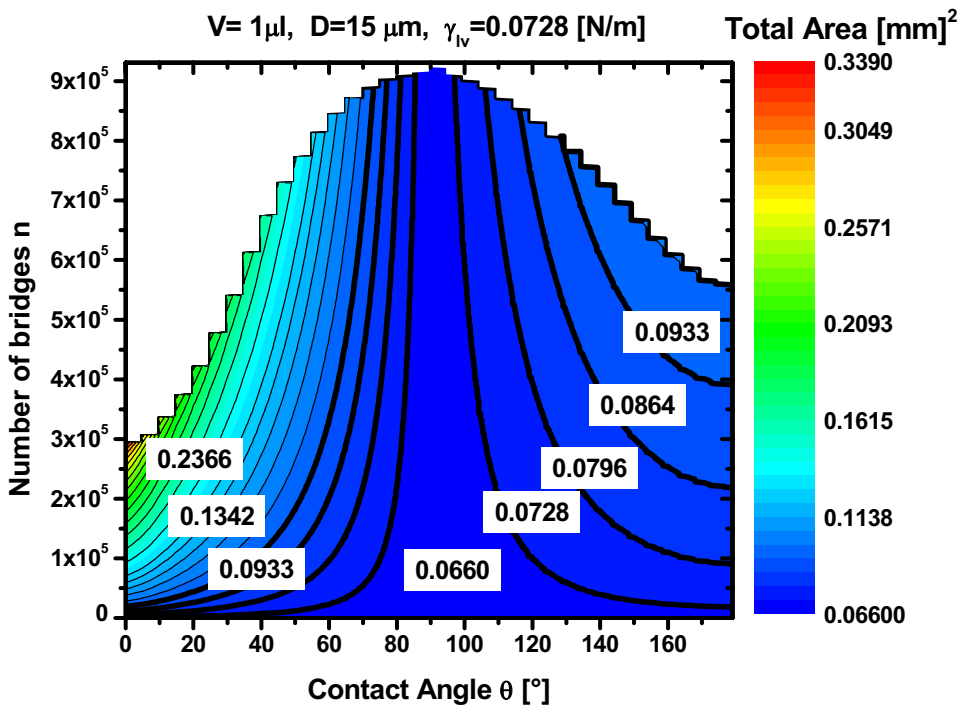


**Figure 2.7**: Map of the minimal projected area of the bridges onto the plates necessary to accommodate the liquid-solid contact areas of n liquid bridges versus the contact angle θ and the number of bridges n. Isolines are labeled in [mm$^2$].

- **Map of stress**

The results presented in Figure 2.5 (map of force) and in Figure 2.7 (map of area) show that both force and area increase as a function of *n*. Therefore, it is interesting to calculate the mean contact stress given by the total force per total contact area (Figure 2.8).

Comparing Figure 2.8 with Figure 2.5, it can be seen that the maximal stress is now obtained for $\theta=90°$ instead of $\theta=70°$ as before; the reason lies in the fact that bridges with straighter contours take up less projected area. For $\theta<35°$ the stress decreases and for $\theta>90°$ it increases as a function of *n*.

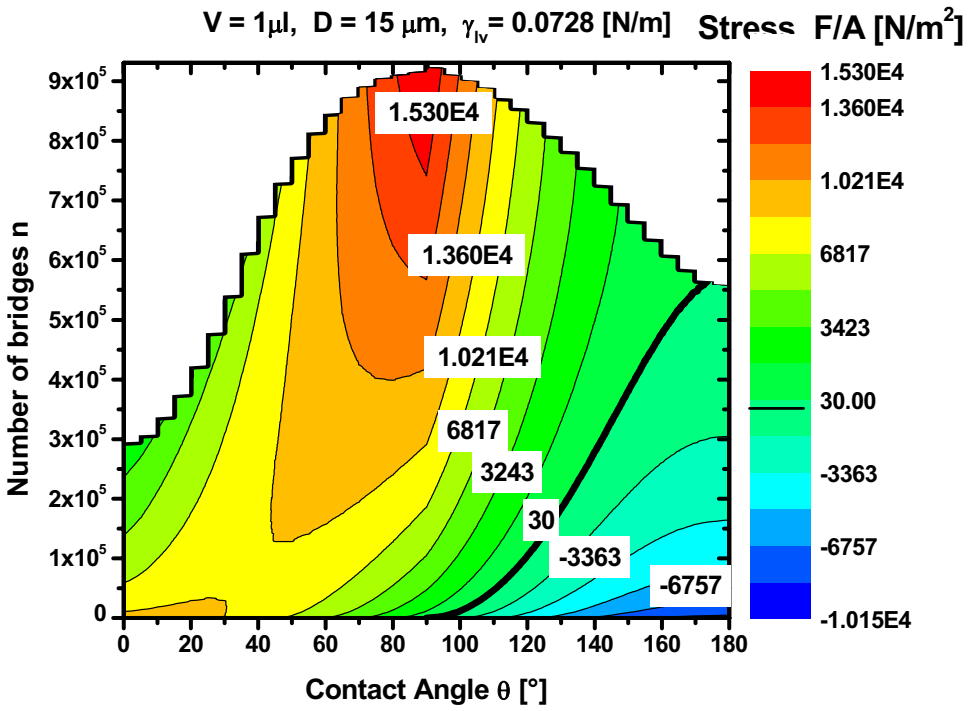


**Figure 2.8**: Map of the stress versus the contact angle and the number of bridges. Isolines are labeled in [N/m$^2$].

- **Enhancement effect of multiple bridges**

It is instructive to evaluate the enhancement of the adhesion force and of the stress exerted by multiple bridges. We define an enhancement α for force and β for stress as follows:

$$\alpha(\theta) = F_{\max} - F(1), \tag{2.8a}$$

$$\beta(\theta) = S_{\max} - S(1), \tag{2.8b}$$

where Fmax is the maximum value of the total force Fn for a given angle θ.

Note that Fmax does not necessarily occur at n=nmax (see Figure 2.4). F(1) is the total force for the same angle due to one single bridge. Analogously, Smax and S(1) denote the maximal stress and the stress exerted by a single bridge for a given angle.

$\alpha$ and $\beta$ thus measure the maximal increase of the force or the stress for a given angle. The results are plotted in Figure 2.9, where we rescaled $\beta$ by a factor $10^{-5}$ in order to be able to

show both curves in one graph.

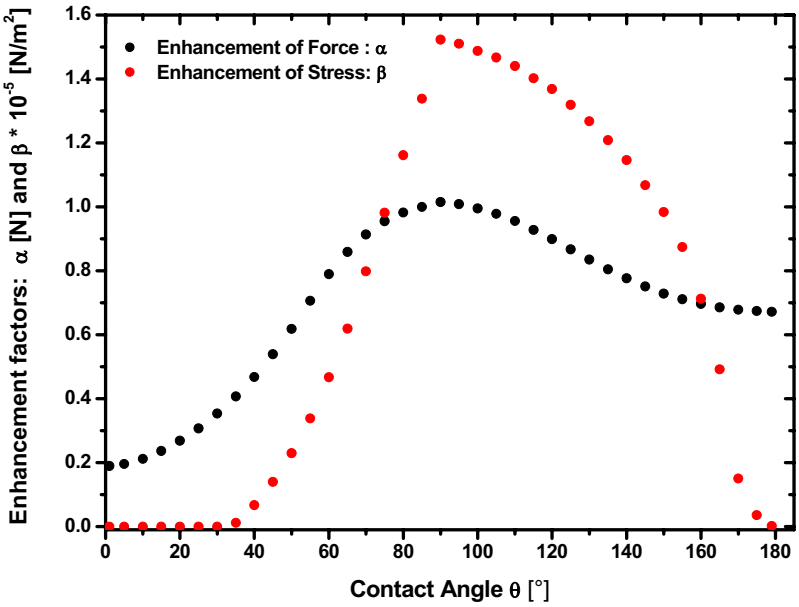


**Figure 2.9:** Enhancement $\alpha=F_{max}$ - $F_1$ and $\beta=S_{max}$ - $S_1$ versus contact angle.

It can be seen that $\alpha$ has a maximum at $90°$ and is not symmetric with respect to this maximum. The same also holds for $\beta$ but the asymmetry between the hydrophilic and hydrophobic regimes is even more pronounced. For $\theta < 35°$ there is no enhancement of the stress by increasing $n$ and hence $\beta=0$.

### 2.4.4 Work of separation

The work of separation is the energy necessary to pull the substrates apart starting from an initial separation that corresponds to a stable arrangement of liquid bridges. It is calculated as the difference between the energy of liquid bridges between two substrates at their maximal separation and the energy at an initial separation $d_{initial} < d_{max}$. It follows for the work of separation $W_n$ for $n$ bridges:

$$W_n = E_n(d_{\max}) - E_n(d_{initial}) = n s_n^{\,2} \gamma_{lv} \left[ e(d_{\max}) - e(d_{initial}) \right]. \qquad (2.9)$$

Here, $E_n(d)$ is the total energy of $n$ non-interacting bridges that is obtained from eqn. 2.5c and $d_{max}$ is the maximal normalized separation which is independent of $n$ (see section 2.3.1).

Consequently, the maximal absolute separation $D_{max}=d_{max}(3V/4\pi n)^{1/3}$ decreases as a function of $n$ as is expected for a decreasing volume of the individual liquid bridges.

To compare the work of separation for different numbers of multiple bridges, we choose the absolute initial separation $D_{initial}$ to be constant (15 µm) for all $n$, while $V$ and $\gamma_{lv}$ remain as before. Furthermore, to compare this energy with values reported in the literature [62], we divide the work of separation $W_n$ by the area $A_n$ calculated with (eqn. 7). In Figure 2.10 the top view of a three dimensional graph shows how $W_n$ depends on $\theta$ and $n$.

The work of separation possesses a maximum for a single bridge under hydrophilic conditions. Its dependence on $n$ is such that it decreases monotonically with $n$ for $\theta<35°$ but has a maximum at $n>1$ for larger angles. For a constant number of bridges, the work of separation always exhibits a maximum at some angle $\theta$. At $n_{max}$ it is zero for all values of $\theta$ because under the conditions chosen the liquid bridges are at the verge of instability already at the initial separation.

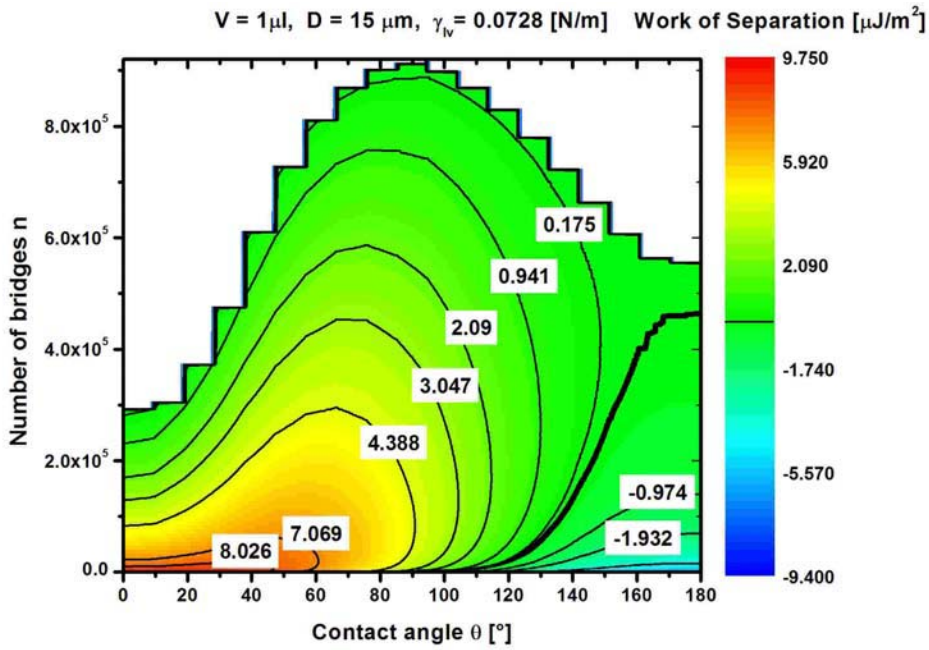


**Figure 2.10:** Map of work of separation as function of the contact angle and the number of bridges. Isolines are labeled in [µJ/m$^2$].

## 2.5 Discussion

### 2.5.1 Capillary force as a function of distance and contact angle

The excellent match of our force-distance curves for one liquid bridge with the analytically calculated curves in [40] demonstrates that the energy minimization with Surface Evolver is precise over the whole range of contact angles and distances. This finding justifies the application of numerical minimization methods to new problems for which there are no analytical solutions yet.

Two main results can be seen from the force-distance curves in Figure 2.2:

a) For contact angles $\theta \leq 90°$ the force is positive over the entire range of distances. In this case, the liquid bridge always exerts an attractive force between the substrates. The attraction decreases monotonically with the distance between the substrates because both the Laplace pressure and the surface tension decrease.

b) For angles $\theta > 90°$ the sign of the force changes. This results in a repulsion of the substrates that decreases with increasing spacing and finally turns into a weak attraction. It is interesting to note that even in the case of hydrophobic substrates the capillary force can be weakly attractive.

### 2.5.2 Capillary force as a function of the number of bridges and the contact angle

The results in Figures 2.4 to 2.6 reveal that for all contact angles the splitting of one liquid bridge into n smaller ones leads to an increase in the capillary force. The maximum of $F_n$ for small angles and its monotonic increase for large angles result from the interplay of two terms. Equation 2.6 shows that $F_n$ grows with $n$ as $n^{2/3}$ for constant $\theta$ and $D$.

On the other hand, the normalized force, $f(d_n)=f(d\cdot n^{1/3})$, decays in magnitude as its argument increases with $n$. This decay occurs rapidly for small arguments and then levels off and approaches the saturation value for the largest possible argument $d_{max}(\theta)$ (see Figure 2.2).

In the hydrophilic regime, these two terms compete and lead to a weak but monotonic increase of the force for angles $\theta>50°$. For angles $\theta \leq 50°$, however, the decay of $f(d_n)$ remains steep because $d_{max}$ is small, i.e. rupture occurs at small distances, which leads to the observed maximum of $F_n$ for these angles.

In the hydrophobic regime, the two terms act in the same direction and thus create a monotonic increase of $F_n$ leading to attractive capillary forces for large values of $n$ even if the substrates are hydrophobic. This effect was also observed for only one bridge (see section 2.4.1) but it is amplified for multiple bridges in the sense that higher attractive forces are attained at the point of rupture for the same total volume $V$.

A striking example of the adhesive effect of multiple bridges is visualized by the iso-contours in Figure 2.5. They show that multiple bridges can generate the same attractive force between hydrophobic substrates at, for instance, $\theta = 120°$ as one large bridge does for hydrophilic surfaces with $\theta = 40°$.

This finding raises a question of practical importance, namely whether it is possible to render repulsive forces attractive in a reversible manner by small changes in the contact angle (for instance with the help of the electrowetting effects [131]). Figure 2.6 shows that this is theoretically possible independent of $V$ and $D$ and that it is easier for larger $n$.

Another interesting result of the balance of the two terms in $F_n$ is the fact that the maximum

force (as a function of $n$ and $\theta$) does not occur at very small angles, i.e. for very hydrophilic situations, as one might have expected. Neither does it occur at the angle $\theta=90°$, for which $n_{max}$ is largest. Instead it occurs for moderately hydrophilic situations, i.e. at $\theta\approx70°$ and $n=n_{max}(70°)$. In this case, the number of bridges is large enough for the $n^{2/3}$-term in $F_n$ to create a significant increase in the force, but at the same time it is still small enough for the individual bridges to have a sufficiently large liquid volume.

### 2.5.3 Minimum contact area and stress

The map of minimal contact area (Figure 2.7) illustrates that if the total available liquid-solid contact area is limited but a large number of bridges is still favorable, then the best choice of the contact angle is close to $90°$. No matter if $\theta$ approaches $90°$ from above or below, as long as it is close to $90°$, the total area is small even if $n$ is large. At the same time, the force $F_n$ is large (Figures 2.4 and 2.5), leading to a high stress for angles close to $90°$ (Figure 2.8).

For angles larger than $90°$ the stress decreases rapidly because $n_{max}$ and hence $F_n$ decreases rapidly while the area increases weakly. The region of relatively high stress in Figure 2.8 for angles $\theta<35°$ and small $n$ reflects the fact that the force is almost constant and high and the area is almost constant and small over this regime.

The enhancement of the adhesion force *and* of the stress due to multiple bridges is largest for $\theta=90°$ (Figure 2.9). Again, it is interesting to observe that this maximum is not in the hydrophilic regime, the reason being that $n_{max}$, and thus $F_{max}$ and $S_{max}$ are largest at $\theta=90°$. This result and the pronounced asymmetry of $\alpha$ and $\beta$ would favor the use of less hydrophilic or even weakly hydrophobic substrates for technical applications of adhesive systems with multiple bridges.

For $\theta<35°$ there is no gain in stress as $n$ increases. By contrast, the data in Figure 2.8 show that the stress decreases as $n$ increases because the area increases faster than the force in this regime.

### 2.5.4 Work of separation

Contact splitting has a very different effect if the work of separation is the decisive parameter (Figure 2.10). A single bridge with hydrophilic substrates ($\theta<35°$) produces the highest value because the final separation between the substrates is greater than for multiple bridges at a given $\theta$. With increasing $n$, the maximum separation drops and the attraction is of shorter range.

The map in Figure 2.10 shows that for constant intermediate $n$, the work of separation first increases and then decreases for increasing values of $\theta$. It can become negative for very large angles because of the repulsive interaction force. If a contact system based on wet adhesion is required to combine several properties such as maximal stress and minimal work of separation, our results predict that angles in the range of $70°<\theta<100°$ may constitute a good choice.

### 2.5.5 Stability of multiple bridges

All liquid bridges presented in this work are described as individual systems with constant volume. This description is based on the assumption that transport of liquid molecules through the ambient vapor phase or through a wetting film between the bridges proceeds on time scales that are much shorter than experimentally relevant times.

For a fixed total volume, the global minimum of the energy corresponds either to a single large bridge or to one droplet wetting one of the plates. Hence, a configuration of multiple bridges is unstable with respect to coalescence of neighboring bridges for all contact angles and distances.

However, thermodynamic stability of multiple bridges can be enforced by introducing appropriate constraints that hinder the coalescence of bridges. This can be achieved by the formation of wetting barriers [30] due to topographic or chemical structuring of the surfaces. They can suppress the coalescence of bridges and thus stabilize the formation of separate small bridges. In an experimental or biological situation, individual micro- or nano-scale adhesive structures, such as often observed in attachment organs of animals, can take on the role of wetting barriers. Stable arrangements of multiple liquid bridges are therefore feasible.

Slender and long bridges are subject to mechanical instabilities, as for example the Plateau-Rayleigh instability [20, 132]. All liquid bridges presented in this work have been obtained by numerical minimization of the interfacial energy and are therefore mechanically stable.
The onset of mechanical instability corresponds to the point of rupture in our force-distance curves. Beyond this point (i.e. for distances larger than $d_{max}$) there are no solutions of the numerical energy minimization procedure.

The Rayleigh-Plateau stability criterion for a cylindrical bridge with radius $R$ between parallel plates, for example, requires that its length $L$ satisfies the condition $L < \pi R$ [25, 30]. This is true even for the smallest cylindrical bridges considered in this work. As stated in section 3.2, it is this maximal length (or correspondingly, the minimal volume for fixed $L$) of the bridges that defines $n_{max}$ for a given contact angle and that ensures that all bridges presented in this work are mechanically stable.

### 2.5.6 Comparison with biological systems and with van der Waals forces

Splitting of one large contact element into many smaller, hairlike elements is observed in many biological attachment systems [9, 133]. The advantages of the principle of contact splitting in predominantly dry adhesive systems such as in spiders [134] and geckos [9, 10] include an increase of the adhesion force with the number of contacts due to minimization of elastic strain energy [102], and good adjustment to rough surfaces by increasing the contact area and thus the number of molecular interactions between the substrate and the contact elements [135, 136].

The gecko, for example, possesses several million micrometer-sized contact elements (setae) that can create a contact area large enough to generate an adhesion force that is greatly in excess of the force needed to carry the gecko's body weight [137, 138]. This adhesion capability provides the gecko with a large safety margin and is still no hindrance to its mobility. A recent paper [138] suggests that the reason being that the gecko's setae are ultra-hydrophobic and thus non-adhesive in the unloaded default state. The gecko therefore combines the conflicting properties of strong adhesion on the one hand and avoidance of inappropriate adhesion on the other hand.

Our study of model adhesive systems based on capillary forces show that the advantages of contact splitting also apply to wet adhesion. The total capillary force and the contact area increase upon splitting of one liquid bridge into several smaller ones for all possible contact angles. In analogy to the contact elements in dry systems, the number of liquid bridges could serve as a control parameter to regulate the contact area and thus the total capillary force. In addition, it could also act as a switch between repulsive and attractive behaviour. This can be seen in Figures 5 and 6 where for contact angles between $90° < \theta < 180°$ the force becomes less repulsive with increasing $n$ and even attractive as $n$ approaches $n_{max}$ (see also section 2.4.2).

Liquid bridges with large contact angles can thus mediate an attractive force between two surfaces that can be reversed by decreasing *n*. A biological wet adhesive system employing such bridges would be well adapted to situations in which reliable attachment and fast detachment are equally important and could therefore be the "wet counterpart" of the gecko's dry adhesive system.

The coupling of attachment and detachment performances may also be the reason why some biological systems [5] employ much less capillary force than they theoretically could. Capillary forces can indeed become very large if the distance between the surfaces becomes small (Figure 2.2). Exactly this fact can turn into a survival disadvantage if the animal has to avoid undesired attachment and/or has to detach fast.

It therefore seems more beneficial for a biological system to operate in the regime of large distances, i.e. close to the point of rupture, where a small increase in *D* leads to easy detachment from a substrate. Although the contribution of a single liquid bridge to the capillary force is small in this regime, the contributions from many bridges can again lead to a large attractive force ensuring good adhesion performance.

There may be biological situations that require a large adhesion force for a small contact area, for example due to a small size of the animal's attachment organ or due to a rough substrate surface. Our results of the capillary force per area (see map of stress, Figure 2.8) indicate that many liquid bridges with a cylindrical shape would be the best choice in this case. These bridges generate the highest forces per unit area because one cylindrical bridge can be split into very many smaller ones ($n_{max}$ (90°) is large) without increasing the total contact area (see Figure 2.7).

If animals make use of the principle of multiple liquid bridges, a fundamental question is how they manage to control the number of bridges formed. One way of doing so could be to control the amount of liquid that is secreted from the contact elements. [139] showed that a large amount of secretion decreases the adhesion performance of insects on smooth surfaces but increases it on rough surfaces. This increase is attributed to the formation of many small liquid menisci in the cavities between the substrate and the animal's adhesion pad that eventually merge to create a large contact area.

This study demonstrates that animals can actively influence the number of menisci that are formed. On very rough substrates this can in principle lead to systems that are very similar to our model systems when each surface asperity accommodates one liquid bridge and the asperities are separated by deep troughs that avoid coalescence of the bridges.

Some biological adhesive systems seemingly employ dry and wet adhesion principles. It is therefore instructive to compare our data quantitatively to dry adhesion based on van der Waals forces. To this end, we envision two systems made of two identical flat substrates, one separated by air (dry system) and the other one by a liquid bridge (wet system). We choose a distance of *5 nm* between the substrates, because in this regime the van der Waals force is non-retarded and has significant strength [140]. If the substrates are made of polysterene, the Hamaker constant is equal to $6.37 \cdot 10^{-20}\ J$ [141].

Applying the well known equation for the van der Waals force between two plates [142] to this geometry, we obtain $\boldsymbol{2.80 \cdot 10^{4}\ N/m^{2}}$. Now let the volume of a liquid bridge be equal to $10^{-18}\ l$. Note that for this volume the number of water molecules is still very large ($3 \cdot 10^{7}$ molecules). We can therefore assume that water still behaves like a fluid and we can calculate the capillary force using the continuum mechanical treatment realized in this work. The

calculation of capillary forces for this volume, a contact angle $\theta = 91°$ for polysterene [143], and separation $D=5\ nm$ leads to a force per unit area of one bridge equal to $\boldsymbol{2.88 \cdot 10^5\ N/m^2}$. This value is 10 times larger than that obtained for the dry system. We now split the bridge into $n=10000$ smaller bridges; this number leads to a volume of an individual small bridge that is equal to $10^{-22}\ l$ (0.1 zeptoliter), which is still above the minimum value necessary to apply continuum mechanics [144]. The splitting further increases the capillary force by a factor of 100, to $\boldsymbol{2.88 \cdot 10^7\ N/m^2}$.

This comparison seems to suggest that in adhesive systems of nanometer size, which applies to many biology attachment organs, the concept of liquid bridge splitting can principally generate adhesion forces that exceed van der Waals forces in dry systems by several orders of magnitude.

## 2.6 Conclusions

We performed numerical calculations of the capillary force between two planar substrates with identical contact angles. The results, displayed as a function of the separation of the plates, agree well with analytical results for the entire range of contact angles. In addition, we presented novel calculations of the capillary force as a function of the number of liquid bridges for constant total volume. The results predict an increasingly attractive force for multiple bridges even for contact angles larger then $90°$. This finding demonstrates that the adhesion force of a wet contact system is not only a function of the contact angle but is also a non-linear function of the number and size of liquid bridges. Two-dimensional maps conveniently summarize these results; they can be helpful tools in the design of artificial wet-adhesive systems.

Depending on the adhesion requirements, different “optimum” regions were found:

- To optimize the *total capillary force,* a large number of individual bridges and a contact angle of about $70°$ is advantageous (red region in Figure 2.5).
- To achieve a high *capillary force per contact area* (contact stress), the optimum occurs for a large number of cylindrical bridges with $\theta=90°$ (red region in Figure 2.8).
- A high *work of separation* is achieved for single bridges and hydrophilic surfaces, $\theta<35°$ (orange region in Figure 2.10).
- Under the assumptions of our calculations, also hydrophobic contacts profit from contact splitting : for large $n$, repulsive interactions may even turn into attractive interactions.
- Our discussion of "wet" biological contact systems suggests that animals may modulate attachment forces by controlling the number of liquid bridges or the volume of secreted fluid.

# 3 Capillary forces between chemically different substrates

## 3.1 Abstract

Motivated by experimental results, we present novel numerical calculations of the force versus distance exerted by a liquid bridge between two substrates with different contact angles, i.e. different chemical properties. Compared to identical contact angles, the results for chemically asymmetric substrates are qualitatively different: one strongly hydrophilic substrate, for instance, exerts mostly attractive forces over the whole range of displacements, independent of the contact angle of the second substrate.

The results are displayed in a map of force versus both contact angles for a given separation. These results allow the derivation of an approximated capillary force, which can be conveniently used to analyze experimental results. We calculate also the rupture displacements, i.e. the maximal extensions of liquid bridges, as a function of the contact angles. Our results show good agreement with previous theoretical models and experiments.

## 3.2 Introduction

As outlined in chapter 1.2, the force exerted by a liquid bridge between two substrates was investigated extensively for a variety of conditions. But most of these investigations are based on idealized assumptions and are therefore not sufficient to explain situations as they occur for example in technical or biological attachment situations. For example, the experimental force-displacement curves presented in chapter 4 differ strongly for chemically different substrates from those for identical contact angles. Consequently, there is a need for further investigations of the effect of different contact angles on the capillary force. In this work, I conduct numerical calculations and experimental measurements of the capillary force for

liquid bridges between parallel rigid plates with different surface properties and hence also different contact angles.

## 3.3 Methods

We used the same experimental set up as described in chapter 4 to measure the force-displacement curves of liquid bridges between different substrates. To summarize briefly, we placed a drop of water on a glass plate and moved it towards a second plate that was attached to a cantilever. A deflection of the cantilever was measured when the drop connected both plates thereby forming a liquid bridge. The force-displacement curve was obtained from the cantilever deflection when moving the top plate towards the bottom plate or away from it.

For the calculations, we assume two planar substrates with different wetting angles $\theta_1$ and $\theta_2$, a distance $D$ between them and a constant liquid volume $V$ as depicted in Figure 3.1.

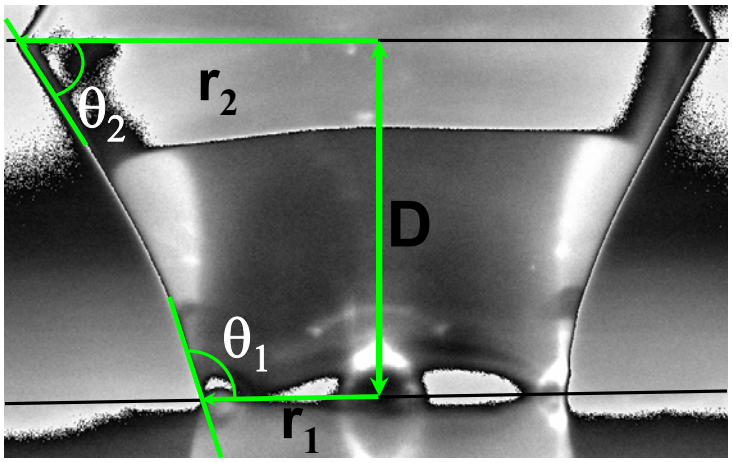


**Figure 3.1** Image of a liquid bridge of volume $V \approx 0.5\ \mu l$ between different substrates with $\theta_1 = 108°$ and $\theta_2 = 60°$, recorded during the measurement of a force-displacement curve. This picture illustrates that the surface profile of the bridge cannot easily be approximated by a sphere or some other simple geometric function.

Under these conditions, the total energy of the liquid bridge is numerically minimized using

the software package Surface Evolver [108]. This software has been successfully used for the analysis of cylindrical bridges between equal disks [122], liquid systems between three [123] and more particles [145], configurations of the liquid contact line on patterned super hydrophobic substrates [124] and to calculate the force of multiple liquid bridges (chapter 2 in this thesis). In the following sections, we will use the same notations as in chapter 2.

## 3.4 Results

In the following subsections we will show how specific asymmetric combinations of contact angles at the bottom and top plates influence the behavior of the force (section 3.4.2) and compare the results to symmetric systems (chapter 2 and review below). These investigations are extended to include large contact angle asymmetries which are shown to evoke large asymmetries in the force-displacement curves as well. The behavior for arbitrary contact angle asymmetry is shown for a given separation in section 3.4.3. To asses the behavior at the point of rupture qualitatively, we display in section 3.4.4 the maximal separation of the plates as a function of the contact angles for symmetric and asymmetric configurations. Finally, in section 3.4.5 we compare the calculated results to experimental measurements of the capillary force between chemically different substrates.

### 3.4.1 Review of the symmetric case: $\theta_1 = \theta_2$

For later reference, Figure (3.2) presents curves of the normalized force versus the normalized displacement for identical contact angles (for details see chapter 2).

In this case, forces are attractive (positive) for contact angles $\theta \leq 90°$ (hydrophilic surfaces) and increase for decreasing values of $\theta$. The opposite behavior is seen for $\theta > 90°$ (hydrophobic surfaces). Attractive forces can be observed for all contact angles at large

separations. The maximal displacement for stable liquid bridges (point of rupture) is largest for $\theta = 90°$ and decreases monotonically for smaller and larger values of the contact angles.

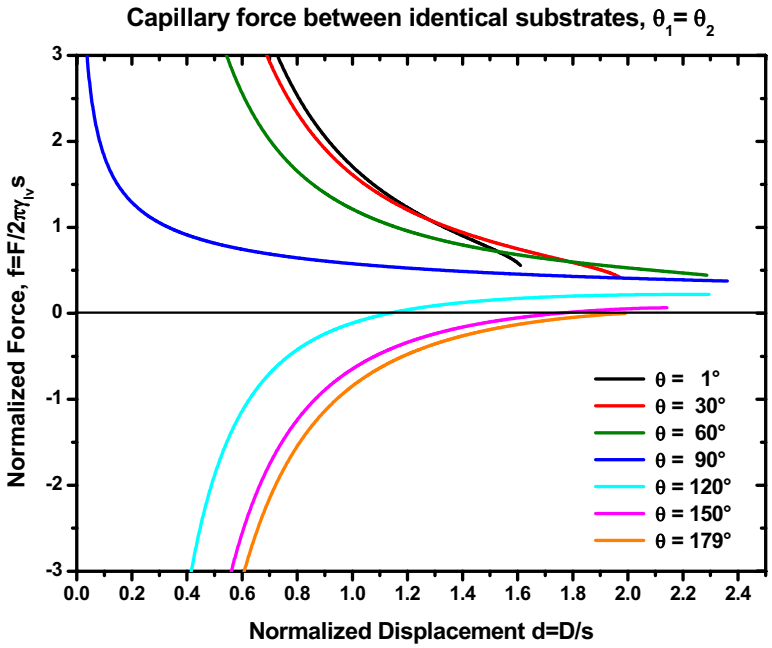


**Figure 3.2** Capillary force versus displacement displayed for different but identical contacts angles $\theta = \theta_1 = \theta_2$. Hydrophilic surfaces (contact angles $\theta \leq 90°$) lead to attractive forces (positive) while hydrophobic ones (contact angles $\theta > 90°$) to predominantly repulsive forces (negative).

### 3.4.2 Effect of contact angle asymmetry: $\theta_1 \neq \theta_2$

Figure 3.3 shows normalized force-distance curves for fixed contact angles, as for example, $\theta_1=60°$ (a) and $\theta_2=120°$ (b). It is evident that the force is not simply the average of the corresponding symmetric cases. The same applies to the distances of rupture, which are always largest for the symmetric case and decrease with increasing degree of asymmetry.

Inspection of Figure (3.3a) also shows that if $\theta_1$ is chosen such that $\theta_1 < \theta_2$ then the corresponding normalized force $f(\theta_1,\theta_2,d)$ tends to be more attractive as compared to the symmetric case with $\theta_1 = \theta_2$. Even the sign of the force can change in this way: the force for $\theta_1 = 60°$ and $\theta_2 = 120°$, for example, is attractive over the whole range of distances while for $\theta_1 = \theta_2 = 120°$, it is repulsive except for very large distances.

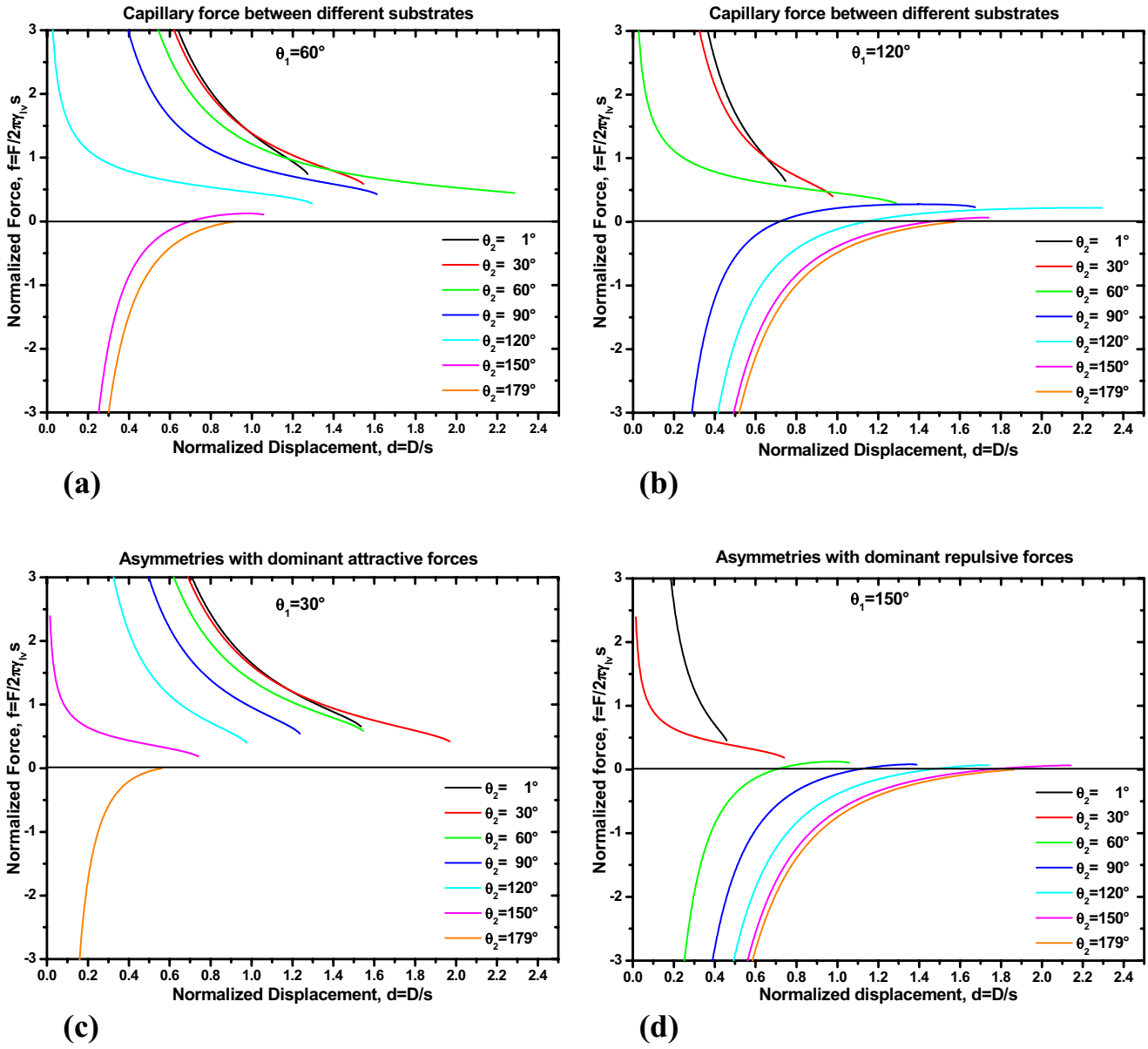


**Figure 3.3** Four examples of asymmetric configurations where $\theta_1$ is fixed while $\theta_2$ is varied. A hydrophilic substrate with $\theta_1 = 60°$ (a) can lead to entirely attractive forces even if the second substrate is hydrophobic ($\theta_2 = 120°$). Conversely, a hydrophobic substrate with $\theta_1 = 120°$ (b) can lead to predominantly repulsive forces even if the second substrate is hydrophilic ($\theta_2 = 90°$). These effects are more pronounced if the first substrate is super hydrophilic (c) or super hydrophobic (d). In these cases, the force remains attractive or repulsive even for large contact angle asymmetries.

The contact angle asymmetry thus results in an extension of the attractive region in the force-distance diagram that extends up to a contact angles $\theta_2 \leq 120°$ as opposed to $\theta_2 \leq 90°$ for identical contact angles.

Analogously, for $\theta_1 > \theta_2$ the force tends to be more repulsive than for the symmetric configuration (Figure 3b). For $\theta_1 = 120°$, for example, the repulsive region of the force-distance diagram extends up to contact angles $\theta_2 \geq 90°$ (except for very large distances).

This asymmetry in the size of the attractive and repulsive regions is even more pronounced if $\theta_1$ is either super hydrophilic or super hydrophobic. These situations are depicted in Figures 3c and 3d, respectively. Here the attractive region for $\theta_1 = 30°$ extends up to angles $\theta_2 \leq 150°$, while the repulsive region for $\theta_1 = 150°$ extends up to angles $\theta_2 \geq 60°$ (except for very large distances).

While Figure 3.3 focuses on the behavior of the force for finite distances up to the point of rupture, the asymptotic behavior for $d \rightarrow 0$ is shown in Figure 3.4. Here, we calculate the force for the same contact angles $\theta_1$ as in Figures 3.3a and 3.3b and vary $\theta_2$ in steps of $\Delta\theta_2 = 10°$ for better resolution. The results are displayed as a color map whose independent axes are the normalized displacement $d$ and the second contact angle $\theta_2$ while the colors correspond to different force values. Both graphs, 3.4a and 3.4b, display the normalized force for normalized displacements ranging from $d = 0.01$ to $0.05$.

The value of the force approaches infinity if $d$ approaches zero. The black lines represent isolines of equal force where the isoline for $f = 0$ separates the regions of attractive and repulsive forces. Figure 3.4a clearly visualizes that for $\theta_1 = 60°$ the region of attractive forces dominates over the region of repulsive forces, while the opposite holds for $\theta_1 = 120°$.

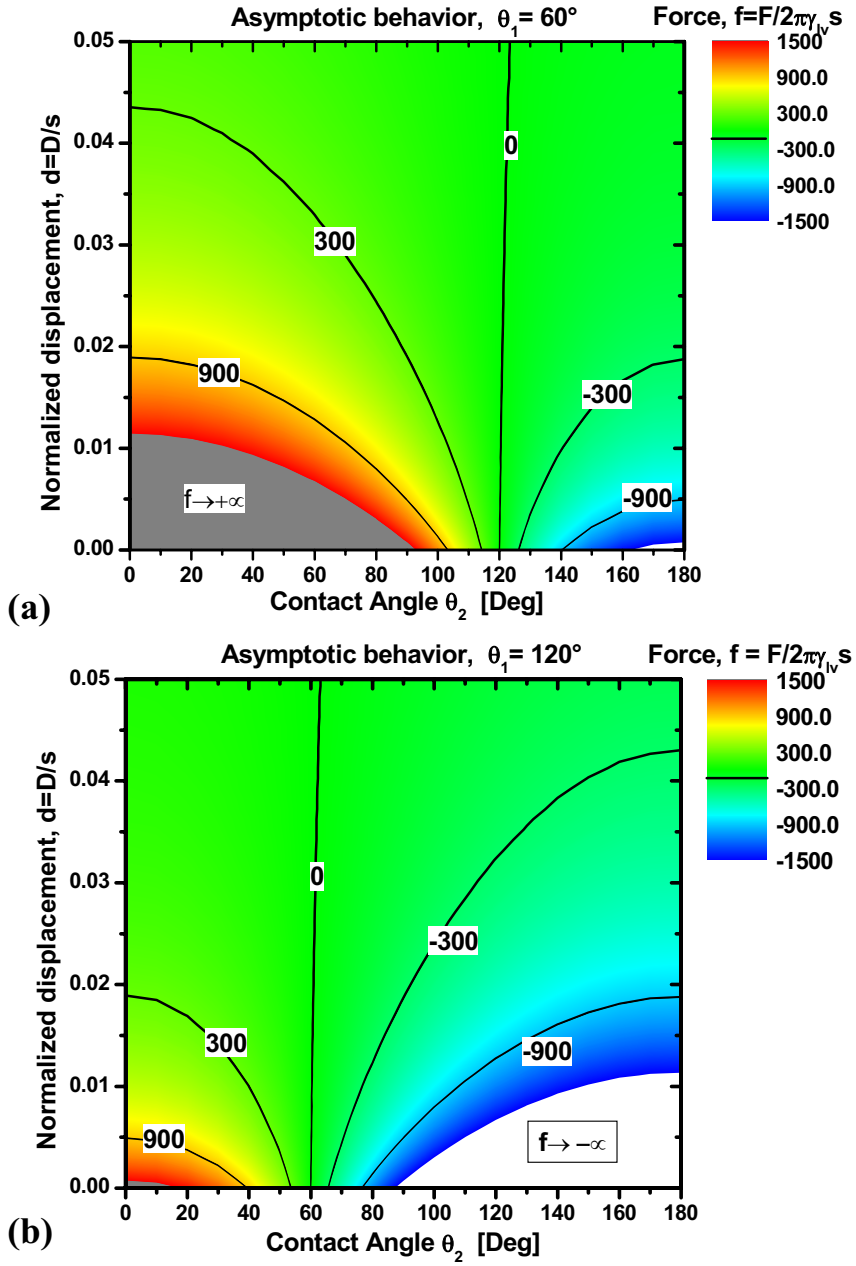


**Figure 3.4**. Normalized capillary force for $d \to 0$. Black lines depict lines of equal force and are labeled by their respective values. The grey region marks the asymptotic behavior of the force: $f \to \infty$ for a hydrophilic substrate (a), and the white region marks the asymptotic behavior $f \to -\infty$ for a hydrophobic substrate (b). In (a) the attractive region of the force dominates the force map while in (b) it is the repulsive region that dominates.

Figure 3.5a displays the normalized force as a function of $\theta_1$ and $\theta_2$ for a fixed normalized displacement $d = 0.05$. For good interpolation, we vary $\theta_1$ in steps of $\Delta\theta_1 = 30°$ while $\theta_2$ varies in steps of $\Delta\theta_2 = 10°$. It is seen that the function $\boldsymbol{f(\theta_1, \theta_2) = \cos(\theta_1)+\cos(\theta_2)}$ (solid lines in Figure 3.5a) matches the numerical results quantitatively very well.

This relationship was first postulated by O'Brien et al.[75] for the case of a liquid bridge between a sphere and plate. We will discuss this result in more detail in section 3.4.4

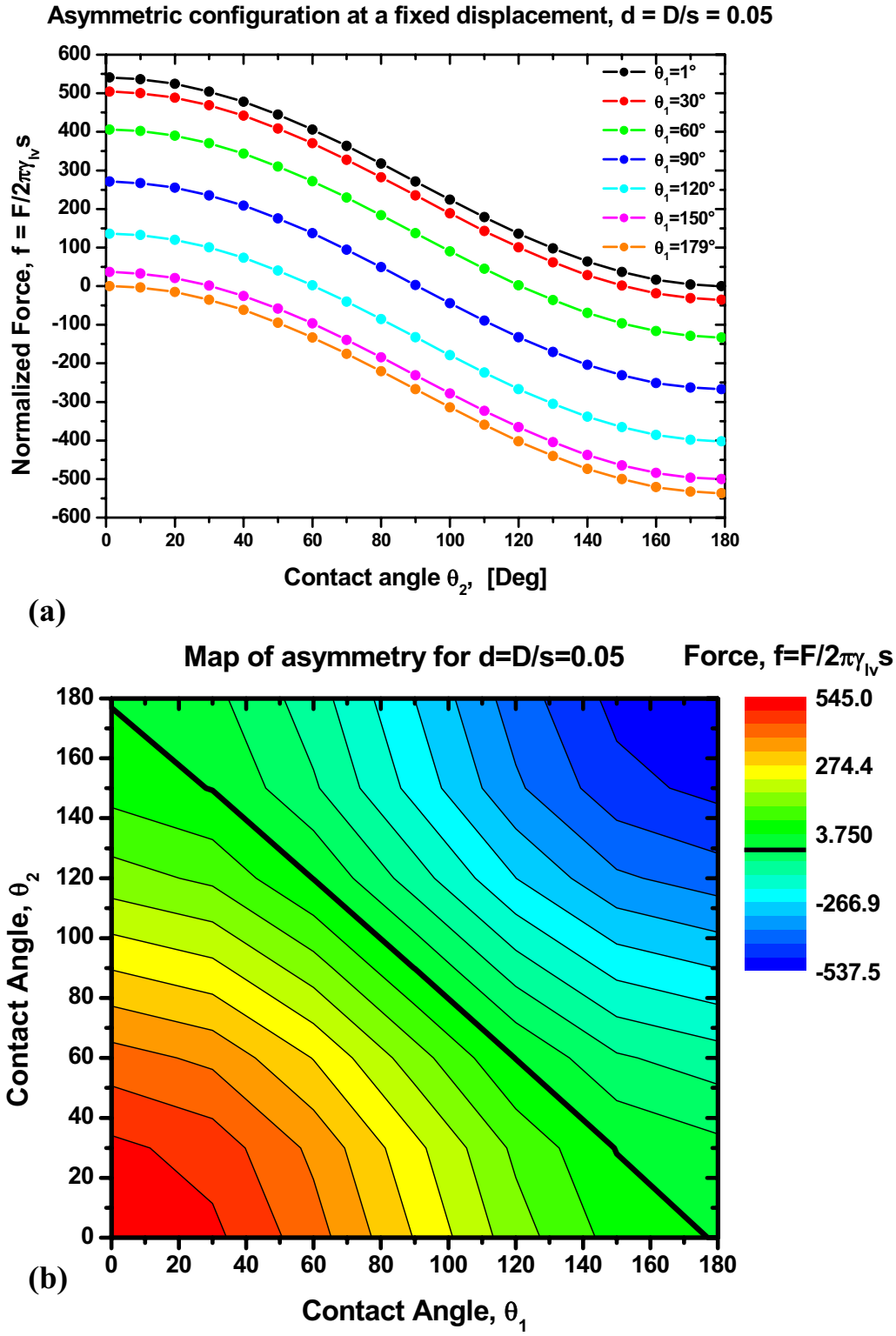


**Figure 3.5**. Behavior of force for a fixed displacement *d=0.05* and arbitrary contact angles $\theta_1$ and $\theta_2$. In (a) $\theta_1$ and $\theta_2$ vary in steps of 30° and 10°, respectively, while in (b) they both vary in steps of 10°. In (a) symbols corresponds to numerically calculated forces while solid lines correspond to fit functions.

The curves in Figure 3.5a can be better visualized as a color map as presented in Figure 3.5b, where we show the normalized force (colors) for all permutations of the contact angles. Here, we vary $\theta_1$ and $\theta_2$ in steps of $\Delta\theta=10°$ for better visualization. In this map, the effect of a super hydrophilic or a super hydrophobic surface leading to large attractive and repulsive interactions, respectively, is clearly visible.

### 3.4.3 Stability and rupture of liquid bridges

In this section we extend our studies to include an investigation of the dependence of the rupture distance on the contact angles.

- **The symmetric case $\theta_1 = \theta_2$**

The maximal extension of a stable liquid bridge, or point of rupture, corresponds to the last point in the force-displacement curve in Figure 3.2. Rupture distances have been calculated analytically by Carter[40]. These results were discussed in detail in chapter 2. Langbein[29] obtained results for rupture distances in terms of the normalized volume and the normalized pressure. To be able to compare his results with ours we express the displacement in terms of the volume:

$$d = \frac{1}{\left(\frac{3\tilde{V}}{4\pi}\right)^{\frac{1}{3}}} \tag{3.2}$$

where $d$ is the normalized displacement, as defined in this work, and $\tilde{V}$ is the normalized volume used by Langbein. According to the criterion calculated by Langbein, a liquid bridge is stable if the surface profile of the bridge has no inflection point between the plates (inflection point criterion) or if the liquid volume does not correspond to an extremum as a function of the Laplace pressure (extremum volume criterion).

In Figure 3.6 we compare our numerically calculated values of the rupture distances with those obtained by Carter and Langbein.

In this graph, all continuous curves were acquired from interpolation of discrete data points for contact angles varying in steps of $\Delta\theta=5°$. As can be seen, all results agree very well over the entire range of contact angles except for the results by Langbein that are based on the criterion of minimum volume. The implications of these results will be discussed in section 3.5

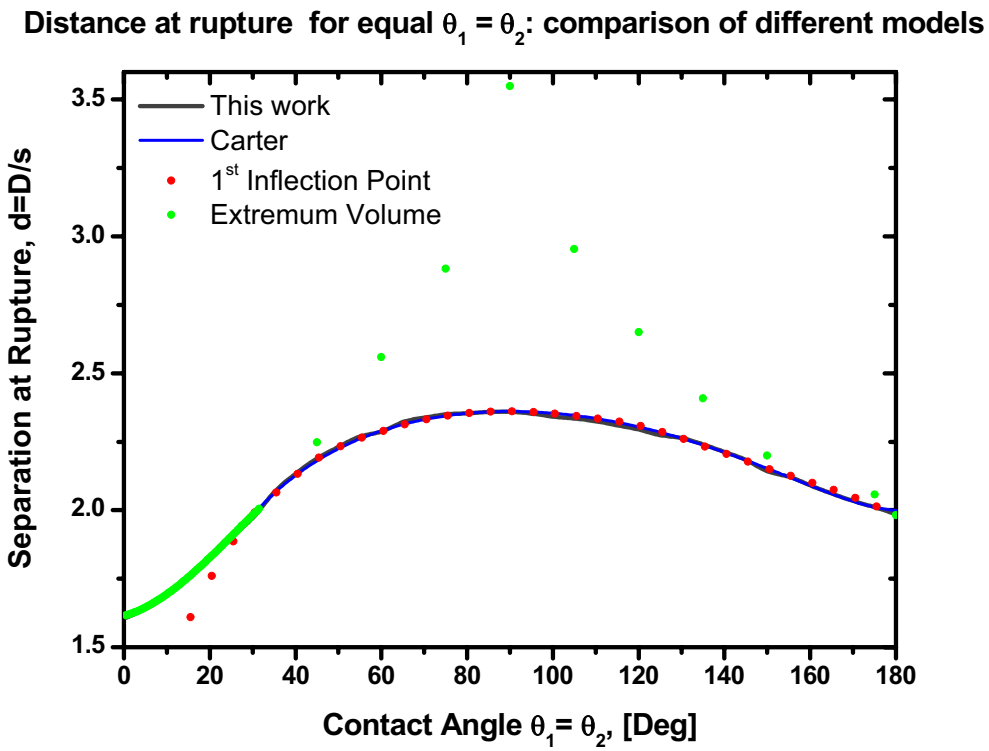


**Figure 3.6**. Comparison of rupture distances of a liquid bridge between substrates with equal contact angles obtained by four different methods.

- **The asymmetric case $\theta_1 \neq \theta_2$**

Since reliable analytical results do not exist for the asymmetric situation, we cannot compare our data to results obtained by other authors in this case. Figure 3.7 shows the rupture distances for many combinations of contact angles as obtained from our numerical calculations.

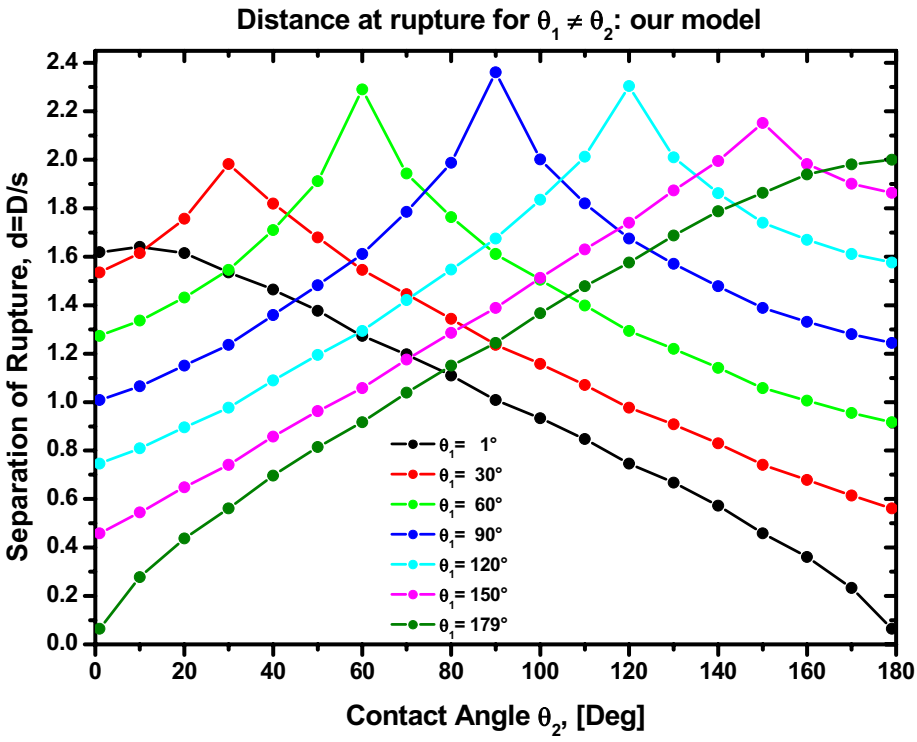


**Figure 3.7**. Rupture distances of a liquid bridges between two plates with different contact angles obtained numerically with Surface Evolver.

For a given contact angle of one substrate, the normalized rupture distance is a maximum only if $\theta_1$ equals $\theta_2$. With increasing contact angle asymmetry, it decreases monotonically in a manner that cannot be fitted to a linear or to a power law function.

### 3.4.4 Application of the model to experiments

In this section we investigate the effect of contact angle asymmetry on the measurement of the capillary force and on the hysteresis of the force-displacement curves in dynamic experiments. In these experiments, the contact angle asymmetry was generated by using different substrates at the bottom and the top of a liquid bridge.

During the dynamic force measurements a liquid bridge between two rigid plates was either continuously stretched or compressed by moving the plates relative to one another with a constant velocity.

The contact angles were measured via the evaporation method as described in [146] and were then used as input for the numerical model to compare the experimental with the numerical data. Liquid volumes were determined from the images of the droplets prior to the formation of a liquid bridge.

The velocity used to move the bottom plate relative to the top plate was set to $v = 10\ \mu m/s$, which ensured that evaporation of an aqueous volume of about 0.5 $\mu l$ was negligible when submitted to a low relative humidity of 18 %. Experiments of this kind are described in more detail in the next chapter. Here we present two relevant examples including the hysteresis for two different substrates.

Figures 3.8a and 3.8b present measured force-distance curves (red lines) for two different sets of plates. In each of these experiments, the branch of the curve marked “advancing curve” corresponds to a compression of the liquid bridge, i.e. the plates are moved towards one another. In this situation, the measured equilibrium contact angles at the two plates are called the advancing angles.

The branch marked “receding curve” represents a liquid bridge that is stretched by pulling the two plates apart from each other and the corresponding contact angles are called receding angles. There are thus four different angles that characterize one dynamic experiment: two advancing and two receding angles for each of the two plates.

The black and blue curves in each figure represent numerically calculated force-distance curves that have been fitted to the advancing and receding branches of the measured curve, respectively, by adjusting the values of the contact angles $\theta_1$ and $\theta_2$ in each fit.

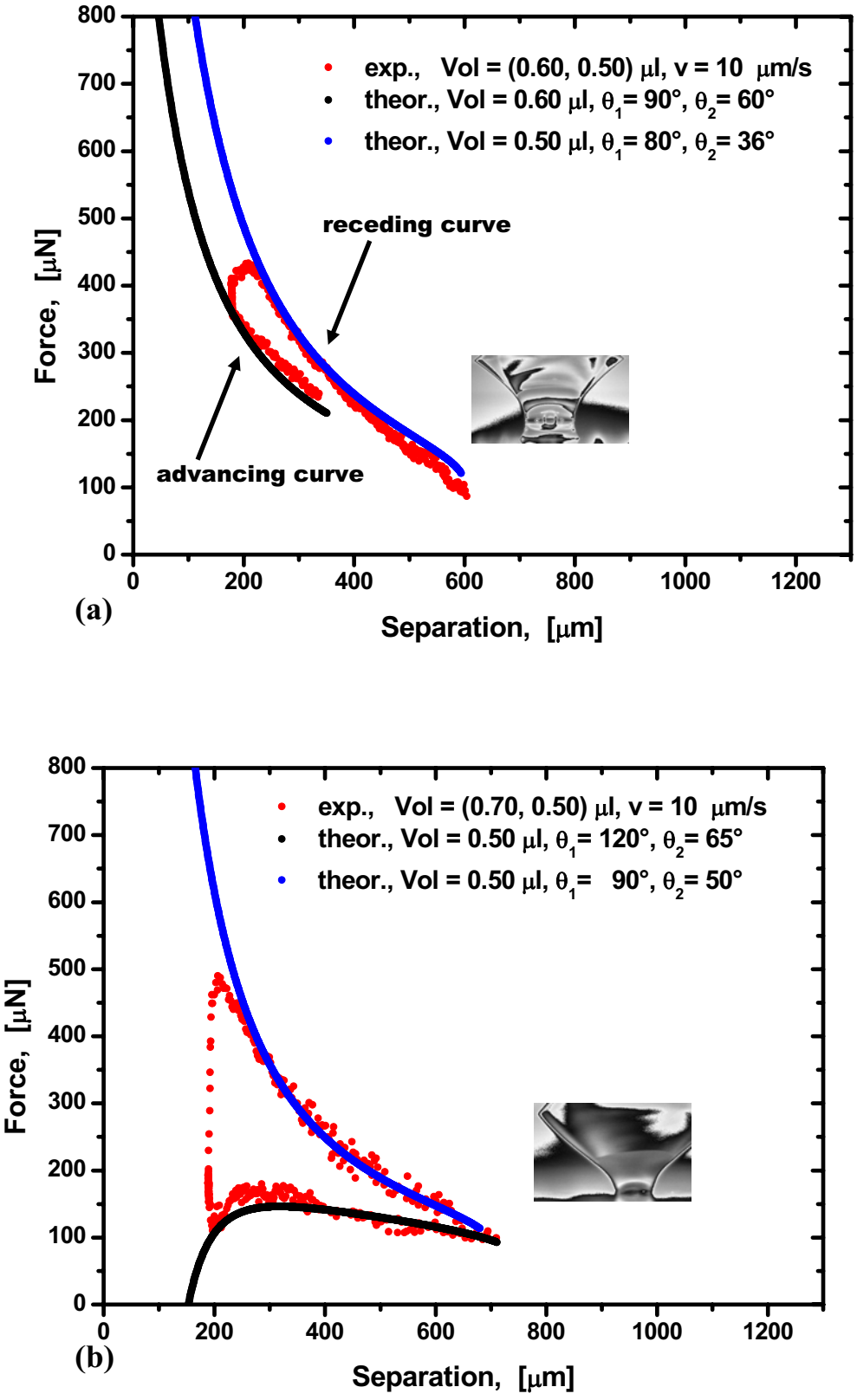


**Figure 3.8.** Measured hysteresis of the capillary force (red curves) and numerically calculated force-distance curves (black and blue curves). By fitting the calculated curves to the advancing and receding branches of the measured curve, the advancing and receding angles of the substrates can be determined. This is demonstrated for two substrates with a small (a) and a large (b) contact angle hysteresis.

The fit curves in Figure 3.8a show that both substrates are hydrophilic and their advancing contact angles correspond to 90° and 60 °, while their receding contact angles correspond to 80° and 36°, which results in a moderate hysteresis of the measured force-distance curve. A more pronounced hysteresis results when one substrate is hydrophobic while the other one is hydrophilic. This is depicted in Figure 3.8b, where the advancing contact angles are approximated by 120° and 65° and the receding contact angles by 90° and 50°.

## 3.5 Discussion

### 3.5.1 Review of the symmetric case: $\theta_1 = \theta_2$

The excellent match of our force-distance curves for one liquid bridge with the analytically calculated curves in [40] was already discussed in chapter 2. Here, we emphasize it again to demonstrate that the energy minimization with Surface Evolver is precise over the whole range of contact angles and distances. This finding justifies the application of Surface Evolver to new problems like asymmetric contact angles for which there are no analytical solutions.

In the symmetric case, contact angles $\theta \leq 90°$ lead to positive forces over the entire range of distances. In this case, the liquid bridge always exerts an attractive force between the substrates. The attraction decreases monotonically with the distance between the substrates because the absolute value of both the Laplace pressure and the surface tension decrease. For angles $\theta > 90°$, the capillary force is predominantly repulsive. This repulsion decreases with increasing spacing and finally turns into a weak attraction showing that the capillary force can be weakly attractive even between hydrophobic and super hydrophobic substrates.

### 3.5.2 Effect of contact angle asymmetry: $\theta_1 \neq \theta_2$

Our results in Figures 3.3a, b show that if one substrate is weakly hydrophilic, the capillary force between this substrate and a second one can be attractive over the whole range of distances even if the second substrate is hydrophobic. Analogously, one weakly hydrophobic substrate can produce repulsive interactions at small separations even if the second substrate is hydrophilic. These observations become even more pronounced if the first substrate is either super hydrophilic or super hydrophobic. In these cases, the capillary force is attractive or repulsive even for large contact angle asymmetries (Figure 3.3c, d). These results illustrate that not only the magnitude but also the type of the capillary interaction, i.e. whether attractive or repulsive, is a function of the properties of both substrates. Therefore, the force-distance curve cannot be easily anticipated if one of the substrates is hydrophilic and the other hydrophobic and if the asymmetry between their contact angles is either small or large. However, if the force-distance curves for asymmetric configurations are known, then for a given substrate, the degree of the contact angle asymmetry can be used as a tuning parameter to adjust the capillary force to a desired value. This determines the wettability of the second substrate and thus facilitates the choice of the substrate material.

The results in Figures 3.3 and 3.4 are also useful in obtaining measurements of contact angle hystereses. Direct measurement of contact angles can be difficult, especially for surfaces with large contact angles. A drop of water on such a surface does not adhere but tends to stick to the needle of dispense or to run downwards on an inclined surface that is used to measure the advancing and receding angle. I have therefore proposed an alternative method to measure the contact angle hysteresis by measuring the hysteresis of the capillary force and fitting numerically calculated force-distance curves to it [see sections 3.4, 4.4]. This fitting procedure allows to determine the contact angle hystereses for two arbitrary substrates.

The results in Figure 3.4 show that the capillary force rapidly diverges if the normalized distance decreases to values below 0.05. The large magnitude of the capillary force for small distances might be the reason why for some animals [5] that apply wet adhesion the measured adhesion force is usually much smaller than predicted by theoretical models. These animals seem to favor relatively large distances between their attachment organs and the substrate, which keeps the adhesion force moderately large and thus ensures efficient detachment from the substrate. In these cases, the optimum distance is therefore the result of the conflicting interests of tight attachment to and fast detachment from the substrate. The asymptotic behavior of a liquid bridge between plates is in contrast with the behavior of a bridge between a plate and a sphere that will be discussed in chapter 5.

The fit of the function $f(\theta_1,\theta_2) = cos(\theta_1)+cos(\theta_2)$ to the numerically calculated forces in Figure 3.5a has been extended to larger values of $d$ (data not shown) and shows the same very good agreement except for distances close to the point of rupture. This fit function was originally postulated by O' Brien [75] for the normalized capillary force between a sphere and a plate and later other authors [74, 87, 89, 94, 95] applied it to similar geometric configurations without verifying it's applicability. Our results show that it also holds for the force between two rigid, infinite plates. This suggests that the applicability of this fit function is limited to configurations in which the linear dimensions of the substrates (e.g. the radii of spheres) are large with respect to the dimensions of the liquid bridge ($D$). In these cases, the fit function provides a quick estimate of $f(\theta_1, \theta_2)$ for constant $d$ which is otherwise a complicated elliptical integral that cannot be given in a closed form

### 3.5.3 Stability and rupture of liquid bridges

The results of different rupture distances of a liquid bridge presented in Figure 3.6 show that the method based on the criterion of an extremal volume is not suitable to approximate the rupture distance between substrates with equal contact angles because it generally leads to an overestimation of the distance by as much as a factor of 1.5. The method based on the criterion of the inflection point seems to evoke more realistic results but it cannot be extended to situations with different contact angles. This is the reason why we display only our own, numerically calculated, results for rupture distances between chemically different substrates in Figure 3.7. These curves demonstrate the superior mechanical stability of symmetric liquid bridges as compared to asymmetric ones for all possible values of the contact angles. These results can help to design appropriate force sensors in measurements of the capillary force between two plates.

### 3.5.4 Application of the model to experiments

Our results in Figures 3.8a and b show that we can reproduce the experimental force-distance curve numerically with high precision using the liquid volume and both advancing angles and both receding angles of the substrates as input for the numerical model. This demonstrates that the model can accurately assess situations in which the contact angles are i) different and ii) at the same time display a hysteresis. Although this is the case in most experimental situations, there are not many studies that address both issues simultaneously. Lambert [147], for example, compares the results of his simulation with experimental data for the very specific case of polydimethylsiloxane-oil between a sphere and a plate with contact angles $\theta_1 = 16°$ and $\theta_2 = 12°$ but he does not discuss the contact angle hysteresis nor the stability of the

bridge.

Having confirmed the accuracy of the numerical model, we can use the calculated force-distance curves for asymmetric configurations to fit them to experimentally measured force-distance curves. This procedure allows to determine advancing and receding contact angles, and thus the contact angle hysteresis of arbitrary planar substrates.

## 3.6 Conclusions

Our results presented for the special case of a liquid bridge between two parallel plates show a variety of new effects that are also expected to apply to substrates with other geometries.
In summary we showed that:

- force-displacement curves can be calculated numerically for arbitrary contact angles,
- a simple fit function exists that matches all calculated force-displacement curves very well,
- symmetric configurations are mechanically more stable than asymmetric configurations,
- a very hydrophilic/ hydrophobic substrate biases the capillary force towards attractive/ repulsive values even for a large contact angle asymmetry.

# 4 Effect of contact angle hysteresis on the measurement of capillary forces

## 4.1 Abstract

We conduct experimental investigations of macroscopic capillary force between two flat rigid substrates characterized by their advancing and receding contact angles with water. Our results exhibit excellent agreement with theoretical predictions obtained by the numerical solution of the capillary equation. Based on this comparison, we use the measurements of capillary force to investigate the phenomenon of contact angle hysteresis. We present examples of force measurements for surfaces that display low, middle and high contact angle hysteresis and compare results for a larger variety of substrates. Finally, we show that for the case of water, the role of viscosity is insignificant within the range of force and velocity measured in the present work.

## 4.2 Introduction

The phenomenon of capillary force is classical, yet still elusive in the context of many real world materials that drive today's applications. The pioneering investigations of capillary force extend back to Young [16] und Laplace [15], who first introduced the concept of surface tension and formalized the capillary equation, where the difference $\Delta P$ between the vapor and liquid pressure, i.e. the pressure across the interface of a liquid bridge, equals the surface tension times the mean curvature ($1/R_1+1/R_2$). Based on this foundation, numerous research groups have increased the general understanding of capillary force in the context of different geometries [43-46, 68, 70-74], environmental conditions [47-59, 67, 101], and materials [60-64, 66, 69]. In most of these studies, the concept of a liquid bridge was regularly used to describe microscopic

events, although they were rarely imaged. The theoretical calculations used to support experimental observations were largely based on two model geometries: i) liquid bridge between two spheres [43-46, 68, 70, 71] or ii) liquid bridge between sphere and plane [47-64, 66-70, 72-74]. The solutions to these model problems were obtained by different approximations and only a few exact solutions of the capillary equation, numerical or analytical, can be found in the literature [70-74]. In general, these results are expressed in terms of elliptical integrals or dimensionless parameters, which are not convenient for the analysis of experimental data. Consequently, most experimental researchers have proposed their own calculations. The insight provided by these previous investigations was fundamental to the general understanding of capillary forces, and its importance was supported by the many applications in the different branches of science and technology. However, this rich literature has largely focused on the modeling of the capillary condensation phenomenon and does not specifically address the effects of surface properties of real world materials. For example, most solid surfaces display hysteresis in the liquid contact angle as it advances with increasing volume and recedes with decreasing volume. How does this hysteresis affect the measurement of the capillary force?

Here, we conduct experimental studies of *macroscopic* liquid bridges of approximately *0.1 - 0.5* µl drops of water between two rigid flat substrates, which are characterized by their advancing and receding contact angles $\theta_a$ and $\theta_r$. Through comparison of experimental data and theoretical predictions, we address: i) the accuracy of a numerical solution to the capillary equation achieved from the minimization of the total energy and ii) the effect of contact angle hysteresis on the measurement of capillary forces for liquid bridges. This new understanding and demonstration is desirable for a variety of applications and is specifically aimed at impacting the interpretation of capillary forces in biology [3, 5, 7], the adhesion measurements of multiple contacts [148-150] and the overall characterization of ultra-hydrophilic and ultra-hydrophobic surfaces properties [146, 151-156].

## 4.3 Methods

Since the main goal of this work is to explore experimentally the impact of contact angle hysteresis on capillary forces, we only summarize the theoretical model to describe general capillary bridge forces.

### 4.3.1 Theoretical model

We assume a liquid bridge with a constant liquid volume $V$ between two perfectly homogeneous flat substrates with equal contact angles $\theta = \theta_1 = \theta_2$ as shown in Figure 4.1.

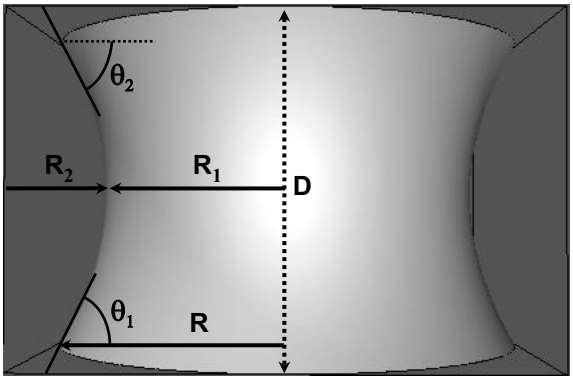


**Figure 4.1.** Illustration of a liquid bridge with volume $V$ between two identical substrates obtained through numerical minimization of the total energy with Surface Evolver [108].

The capillary force depends on the separation $D$ of the substrates, the surface tension $\gamma_{lv}$ of the liquid-vapor interface, $V$ and $\theta$. If the length scale $s = (3V/4\pi)^{1/3}$, set by the radius of a liquid sphere of volume $V$, is small compared to the capillary length $l_{cap}=(\gamma_{lv}/g\Delta\rho)^{1/2}$ (where $g$ is the acceleration of gravity and $\Delta\rho$ the difference between the liquid and vapor densities), then the influence of gravity is negligible and the liquid bridge has a constant mean curvature. In the case of water, $l_{cap}$ =2.7mm, which indicates that for $V$ << 80 µl gravitational contributions can be neglected.

The capillary force can be expressed as the sum of forces arising from surface tension ($F_{tension}$) and Laplace pressure ($F_{Laplace}$) [74] as:

$$F_{total}(D) = F_{tension} + F_{Laplace} = 2\pi R(D)\gamma_{lv}\sin\theta + \pi R^2(D)\gamma_{lv}\left(\frac{1}{R_1}+\frac{1}{R_2}\right) \qquad (4.1)$$

where $F_{total}(D)$ is the total capillary force as a function of the distance $D$ between the substrates; $R(D)$ is the radius of the interface between liquid and solid; and $R_1$ and $R_2$ are the principal radii of curvature. The tension term describes the surface tension of the liquid acting on the substrates while the Laplace term describes the mechanical equilibrium between the bulk phases and the liquid-vapor interface

To compare the predictions of equation (4.1) with experimental data, we need to determine the values of $R$ and $\Delta P = (1/R_1+1/R_2)$ for a given value of contact angle and $D$. To avoid elliptical integrals, we use an equivalent approach as used by Carter [40], which consists of the minimization of the total energy in the capillary bridge system at a given $D$ and $\theta$. The total energy of a liquid bridge is the sum of three contributions: the liquid-solid $(\gamma_{ls}A_{ls})$, the liquid-vapor $(\gamma_{lv}A_{lv})$ and the solid vapor $(\gamma_{sv}A_{sv})$ interface energies, where $\gamma$ and $A$ denote the respective surface energies and surface areas. Since the substrate is considered rigid, we assume the total substrate area to be constant throughout the wetting process. Therefore the interfacial energy $E$ of the system is constant and written as:

$$E = \gamma_{lv}A_{lv} + (\gamma_{ls} - \gamma_{vs})A_{ls}. \qquad (4.2)$$

This expression for the total energy of a liquid bridge is minimized using the software package Surface Evolver [108]. In this method, the liquid vapor interface is substituted by a mesh of triangles whose total area approximates the value of $A_{lv}$. The area of the wetted substrate is obtained by line integrals along the contact line. The constraint of constant volume is expressed by means of a surface integral over a suitably chosen vector field. With the help of this numerical minimization, it is possible to calculate the capillary force as a

function of the separation of the substrates from the first derivative of the total energy with respect to distance. In Figure 2.2, we review the results obtained in [150] to give an overview of how capillary forces behaves for different contact angles over the whole range of displacements.

### 4.3.2 Experimental method

We measure water capillary forces between two substrates with arbitrary surface properties and compare them with force-separation-curves obtained from the numerically-solved model described above. In addition to the measurement of force, we image the liquid bridge before, during, and after the process of contact and separation of the liquid with the two substrates.

These measurements are performed on a custom-built instrument as shown in Figure (4.2).

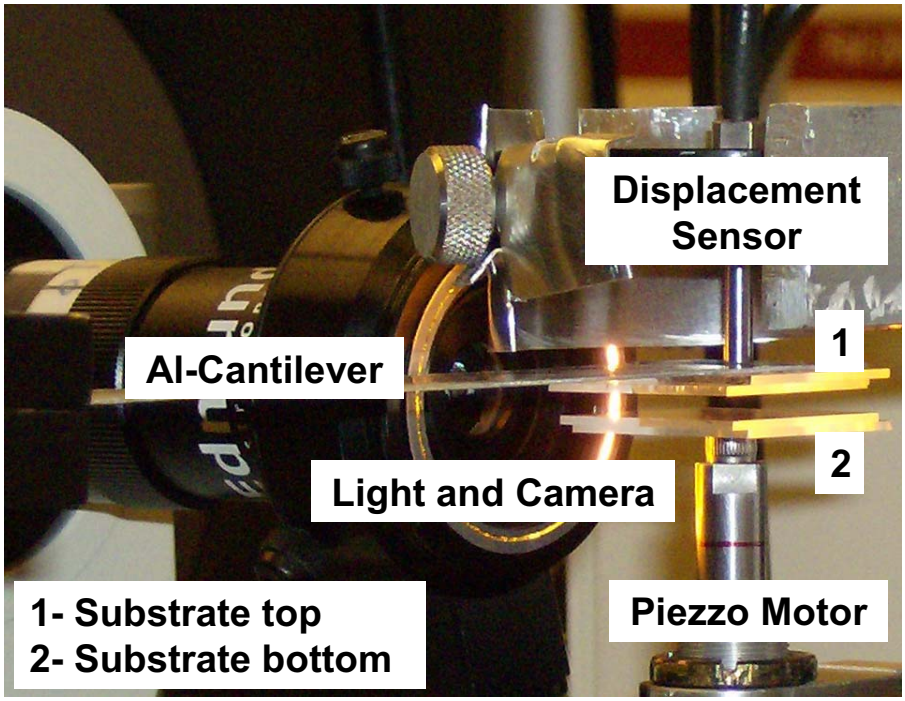


**Figure 4.2.** Picture of the experimental construction, for details see text.

A detailed description of the measurement procedure follows.

- **The measurement:**

First, a droplet of water of V ~ *0.5* µl is placed on the bottom substrate, which is rigidly fixed to piezoelectrically-driven nanopositioner (EXFO Burleigh Inchworm). This droplet then moves by the use of the nanopositioner in the direction of the top substrate, which is fixed to an aluminum cantiliver (Al-Cantilever). The length of the Al-Cantilever can be varied to modify its stiffness for measuring a wide range of forces. When the droplet contacts the top substrate, the Al-Cantilever deflects in response to the capillary force. The deflection is measured by a fiber optic displacement sensor (Philtec), and the position of the nanopositioner is obtained from an integrated optical encoder. Both quantities are recorded continuously through a computer with a National Instruments Labview interface. Since the initial position of the nanopositioner and Al-Cantiliver are recorded, the force and separation can be obtained from the deflection measurements:

$$F = k \cdot d_s \tag{4.3a}$$

$$D = -(d_s + M), \tag{4.3b}$$

where $d_s$ is the deflection of the fiber sensor, $k$ is the stiffness of the Al-Cantilever, and $M$ is the displacement of the nanopositioner.

- **Calibration of stiffness and fiber sensor**

The stiffness of the Al-Cantilever is calibrated using standard weights (0.1 to 6 mN ). The average stiffness value is $k$ =(18.92 ± 0.2) µN/m for the cantilever lengths used in the experiments discussed here. We calibrated the stiffness before each measurement for verification, and each result is calculated with its own stiffness. The noise level of the force measurements is approximately $F \approx 9$ µN. This value is approximately 10 times smaller than the forces measured in this work.

- **Imaging, calculation of volumes and contact angles**.

To facilitate comparisons among different capillary bridges, we image the droplets and the liquid bridges before, during and after each experiment. These images show an exact contour and reflection of the liquid on the substrates as shown in Figure (4.3a). From these images,

we can accurately measure the radius, contact angle and height of the liquid droplets and bridges. From these values, we calculate the volume via the radius and contact angle or via the radius and height through well-known equations for the geometry of a droplet. Volumes calculated from both conditions are compared in Figure (4.3b), and the slope of unity reveals an accurate measurement of both contact angle and volume. In addition to facilitating fair comparisons of different capillary bridges, these values of volume are also used in the theoretical model for direct comparison of measured forces with theoretical calculated forces.

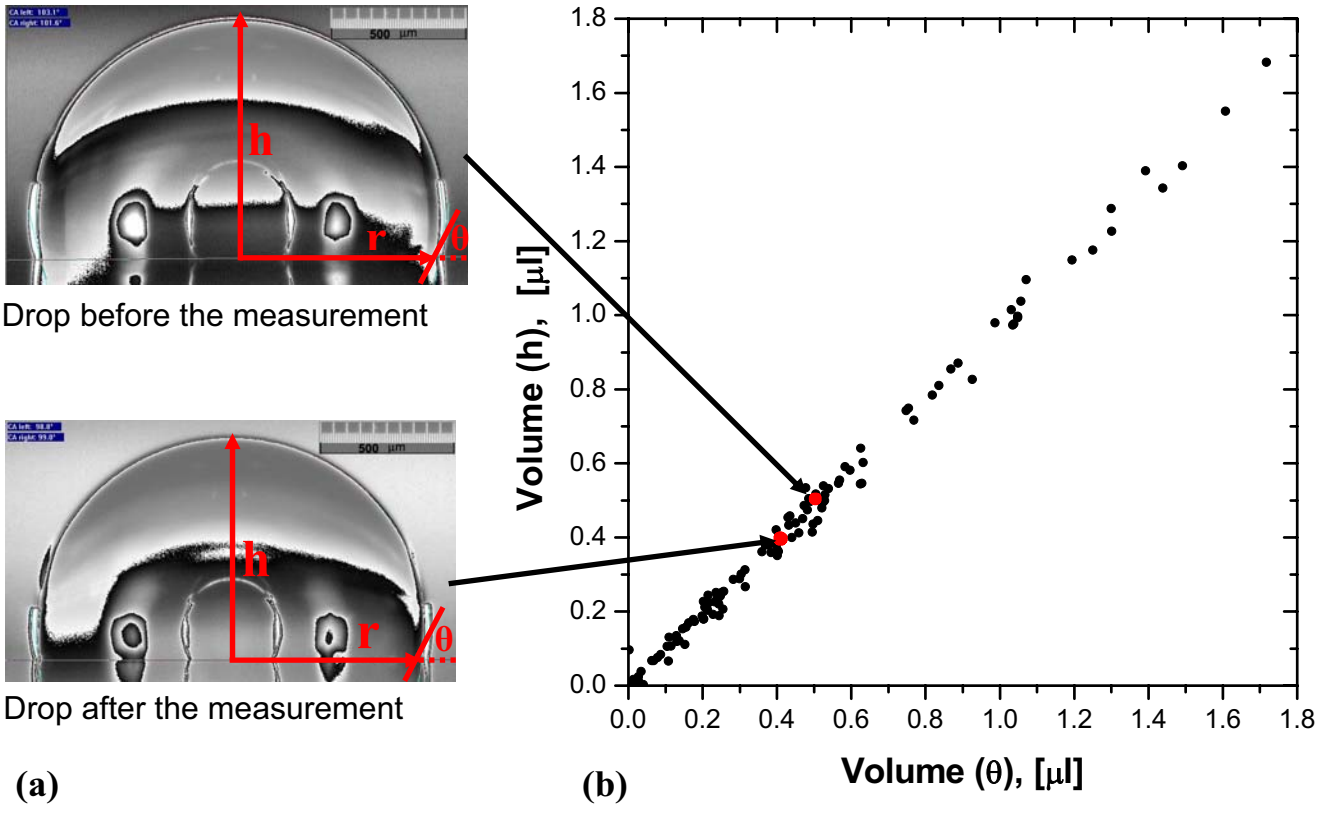


**Figure 4.3.** **(a)** Droplets of water with $V \approx 0.5$ [µl] recorded previous and immediately after each measurement. Height $h$, radius $r$ and contact angle $\theta$ are obtained through the imaged reflection of the surface contour on the substrates. **(b)** Calculated volumes obtained through the measured contact angle and height.

- **Measurement of contact angle hysteresis via evaporation dynamics**

The contact angle of the droplet before bridge formation roughly corresponds to the advancing angle, while the contact angle after bridge rupture is close to the receding angle. Independent measurements of the advancing and receding contact angles were made by a

method described in detail by Gao [146]. This method consists of recording the advancing contact angle as the maximum contact angle during droplet deposition on a substrate and the receding contact angle as the angle at which the contact line moves during droplet evaporation. We measured the contact angle hysteresis of all substrates used in our experiments by recording movies as described above using the instruments of Dataphysics model OCA 30. These values are compared with the contact angles hysteresis obtained from the capillary bridge measurements.

## 4.4 Results

In this section, we present the forces measured experimentally and compare them with the theoretical ones.

### 4.4.1 Measurement of capillary forces between two parallel plates

Figure 4.4a shows a representative force-separation curve for a capillary bridge experiment between two toluene-cleaned glass substrates with advancing contact angle of 70° and receding contact angle of 50°. The red points represent the experimental data while the black and blue lines are theoretical fittings obtained from our numerical model for the advancing and receding contact angles, respectively.

In this representative example, the capillary bridge forms upon approach when the glass substrates are approximately separated by 400 μm. After forming the bridge, the capillary force increases as the bridge length, or separation, decreases upon approach. During approach, the advancing contact angle controls the droplet expansion on the substrates as demonstrated by the black fitting curve. The images of the water droplet/bridge illustrate how the shape of the bridge changes during the approach.

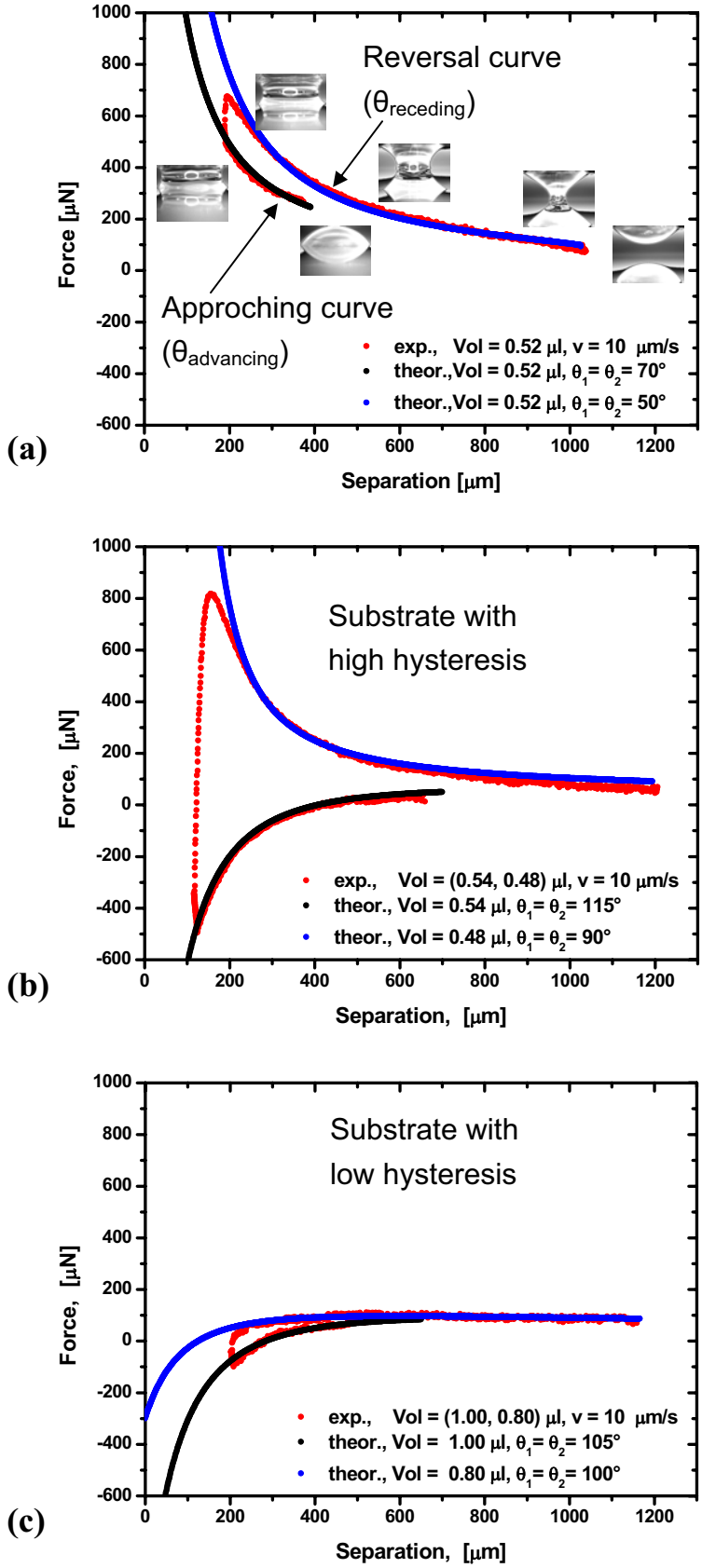


**Figure 4.4** Examples of substrates with different contact angle hysteresis determined by the fitting of the experimental curve with the numerical model of capillary force. **(a)** Glass with intermediate values, **(b)** PDMS with high and **(c)** tris(trimethylsiloxy)silylethyldimethylchlorosilane[151] with low hysteresis demonstrate the good agreement between experimental and theoretical data for a variety of conditions.

At an arbitrarily defined minimum separation, the nanopositioner stops for 10 seconds and subsequently reverses at the same velocity as the approach. Upon reversal, the contact angle decreases until it reaches the receding contact angle and remains constant for the rest of the separation process. Images illustrate the transitions of the bridge at different separations until it ruptures. Since the relative humidity during our experiments was $RH \approx 18$ %, low velocities of approach and separation provide time for evaporation of the water. In fact, a change of volume of 0.1 μl is enough to dramatically change the comparison between experimental and theoretical curves, Therefore, for the volume $V \approx 0.5$ μl, we used a consistent velocity $v = 10$ μm/s for all experiments reported here to avoid significant volume loss due to evaporation. The droplet images before and immediately after the measurements allowed us to calculate the volumes precisely and confirm the insignificant volume loss under these experimental conditions. Larger velocities were not used due to the limited data collection rates of our instrument.

The results in Figure (4.4a) show quantitative agreement for the global behavior of both the model and experimental curves. The small deviation at close separations occurs due to the transition behavior of the contact angle as it changes from advancing to receding when the movement of the nanopositioner reverses direction. This transition does not occur instantaneously and our numerical model does not include a time-dependent change of contact angle. We also found precise agreement, in terms of both force and separation, for the point of rupture of the liquid bridge.

### 4.4.2 The effect of contact angle hysteresis

Figure 4.4 shows three force-separation curves for materials that exhibit different degrees of contact angle hysteresis. Figure 4.4(a) demonstrates the effect of relatively low hysteresis, where both the advancing and receding contact angles are less than 90°. In this capillary

bridge, the forces for both approach and recession are attractive at small separations. This behavior is consistent with our understanding of capillary bridges with static contact angles, as shown in our theoretical curves in Figure 2.

Figure 4.4(b) shows the force-separation paths for substrate materials with high hysteresis. In this example, upon approach the force is repulsive at small separations, but the force changes to attractive at small separations upon reversal of the nanopositioner direction. For these measurements, we used a 1:30 cross-linked poly(dimethylsiloxane) (PDMS) (Dow Corning, Sylgard 184) film supported by a glass slide. The change from repulsive to attractive forces at small separations is an indication of the critical range of advancing and receding contact angles of this material. The advancing contact angle is approximately 115°, while the receding contact angle is approximately 90°.

In Figure 4.4(c), the substrate materials show low hysteresis and both the approach and recession data indicate repulsive forces at small separations. For this experiment, the substrate material was a tris(trimethylsiloxy)silylethyldimethylchlorosilane-silicon supported monolayer[151]. The small hysteresis of the force-separation curves in this figure is consistent with the low hysteresis of the advancing and receding contact angles of the substrate materials.

### 4.4.3 Comparison between capillary force and contact angle methods

In addition to the three representative force-separation curves shown in Figure 4.4, we measured the force-separation curves for an extensive series of different substrates. From these capillary force curves, we used our theoretical curves to determine the advancing and receding contact angles that provide the best-fit curve. For these materials, we also quantified the advancing and receding contact angles with the evaporation method described above [146].

The values for the advancing and receding contact angles from both methods are compared in Figure 4.5.

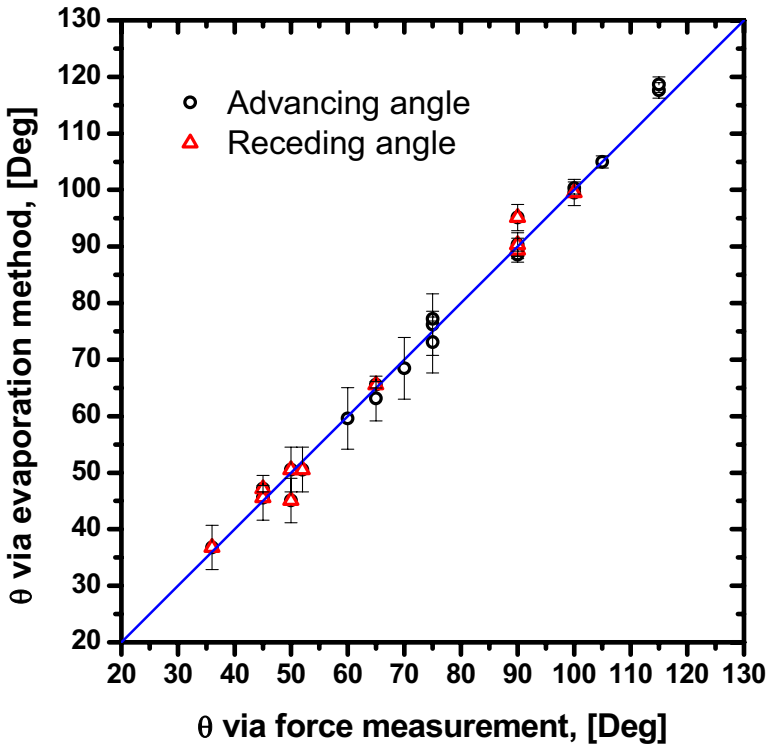


**Figure 4.5** Comparison of contact angle hysteresis obtained by the capillary force measurement and conventional contact angle methods[146].

The error bars for the evaporation method results are calculated from the standard deviations of 6 measurements per substrate. The slope of unity demonstrated in Figure 4.5 confirms the accuracy of using a capillary force measurement for determining both advancing and receding contact angles.

## 4.5 Discussion

### 4.5.1 Measurement of capillary forces between two parallel plates

The force-separation curve of a capillary bridge depends strongly on the contact angles of both bounding substrates, the volume of the drop during the complete measurement, the velocity of the measurement or viscosity of the liquid, the alignment or geometry of the substrates, as well as numerous other parameters. In this paper, we have focused primarily on

the effect of contact angle hysteresis for the substrate materials. The contact angle hysteresis can be simply accounted for in our theoretical model by using the advancing contact angle for force-separation curves during approach and receding contact angles for force-separation curves upon recession. The deviations between our theoretical curves and experimental data at small bridge separations is attributed to the transitional behavior of the contact angle as the substrates change direction. This behavior is not accounted for in our simple theoretical model and further modifications would be required to quantitatively account for these changes.

In addition to relating the force-separation hysteresis to the contact angle hysteresis, our data shows quantitative agreement between experiment and theory for the point of rupture. We observe that larger contact angles lead to rupture at larger separation values. This fact plays a fundamental role in understanding the behavior of multiple liquid bridges [150], which is relevant for understanding the adhesion mechanisms in biology [3, 5, 7] and of patterned surfaces [148, 149].

We note that we have assumed both substrates to have identical advancing and receding contact angles. This assumption is supported by the good quantitative agreement between model and experiments curves. When the bounding substrates are dissimilar, the prediction of force-separation curves becomes more complex. In this case, each substrate has its individual hysteresis and 4 contact angles are required to describe the force-separation curve, i.e. 2 advancing (bottom and top) and two receding angles, to completely fit the experimental curves. The role of different contact angles between the two substrates will be addressed in a subsequent paper.

### 4.5.2 The effect caused by the contact angle hysteresis

Contact angle hysteresis has been studied and reported extensively, but its relation to capillary force hysteresis has not been quantitatively addressed.[146, 152, 154-156]. Our measurements confirm that the hysteresis of a capillary bridge force-displacement curve is directly associated with the contact angle hysteresis of the bridge/substrate interface. This hysteresis causes the specific force-separtion relationship to be history dependent. In other words, the examples in Figure 4.4 clearly indicate that the force associated with a given separation is dictated by the previous movement history for the two bounding substrates. This difference in force for a given separation can be especially significant when the advancing and receding contact angles are greater and less than 90°, respectively (as shown in Figure 4.4b). This path dependence of capillary forces could have important implications in the fabricatiton of micron and nano- scale devices, such as MEMS, where capillary effects often cause defects or failure.

Comparisons between capillary force hyteresis and contact angle hysteresis with our current approach can be obtained only if the advancing and receding contact angles are constant over the whole range of separation. However, it is not difficult to imagine a material with patterns or impurities that cause the contact angle to change with lateral position or time. For these materials, the kinetics of hysteresis become essential for a complete description of the capillary bridge force-separation curve.

### 4.5.3 Comparison between force and standard methods

As Figure 4.5 indicates, capillary force measurements provide a straightforward, alternative technique for quantifying the effect of contact angle hysteresis for a variety of materials. In particular, this approach is robust and sensitive for the characterization of materials that have extreme surface properties, such as ultra-hydrophobic and ultra-hydrophilic surfaces. For these surfaces, the stability of a sessile drop due to gravitational effects or the camera

resolution often limit the precise measurement of contact angles over a range of liquids. These difficulties often limit the fundamental insight that is needed in these technologically-important surfaces. These effects do not present difficulties in the measurement of capillary forces. Once a drop of known volume is on the surface of a substrate, the forces can be measured as a function of separation and the hysteresis can be recorded and analyzed in the context of the numerical model presented here. In these measurements it is clear if the surface is truly non-hysteretic and if the surface is truly superhydrophobic, i.e. $\theta_{adv} = \theta_{rec} = 180°$ . For this surface condition, the entire force-separation curve will exhibit repulsive forces – the only case that exhibits this behavior.

### 4.5.4 Volume evaporation and viscosity

Although previous studies of capillary forces with water bridges often neglect viscosity effects[147, 157], many reports of non-aqueous liquid bridge capillary forces often emphasize the impact of viscosity effects.[158-162]. Therefore, for completeness, it is necessary for us to use Stefan's equation [163] : $F_{visc} = 3\pi r^4 \eta v / 4d^3$ to calculate the viscosity force of a liquid between two discs of radii $r$, viscosity $\eta$, velocity $v$ and separation $d$. With this force calculation, we can determine the validity of neglecting viscosity effects in our measurements. Assuming a value of $r \approx 1000$ μm which is the maximal radius at the minimal separation $d = 200$ μm, the viscosity $\eta = 0.001$ Pas for water and the maximal velocity $v = 10$ μm/s, we obtain $F_{visc\text{-}stefan} = 2.94$ nN. For conditions at the point of rupture, we calculate $F_{visc\text{-}stefan} = 2.64$ pN. These values are significantly smaller than force values measured in our experiments; therefore, our neglect of viscosity contributions is valid for these studies. Future investigations will use different liquids and velocity ranges to investigate viscosity effects in the context of capillary bridges between materials with contact angle hysteresis.

## 4.6 Conclusions

We have shown the importance of hysteresis in the measurement of the force-separation curves for capillary bridges, and the utility of this technique for characterizing general surfaces. The hysteresis of the force-separation curve is related directly to the measured hysteresis of contact angles as shown by the quanitative agreement between our experimental data and theoretical curves from the numerical solution of the total energy of a capillary bridge. This agreement was demonstrated for a wide-range of substrate materials. The characterization of surfaces properties with capillary bridges also emphasizes the importance of the kinetics of transition from advancing to receding contact angles in determining the specific force at a given bridge separation. Finally, we emphasize the ease and quantitativeness of this procedure for the inspection of hysteresis in super hydrophobic surfaces, which is not easily detected in contact angle measurements on these surfaces but is essential for a variety of technical applications.

# 5 Capillary force between sphere and plate

## 5.1 Abstract

We study numerically the effect of the radius of a sphere on its adhesion to a planar substrate due to capillarity. The adhesion force is found to scale linearly with the radius in near contact; for large separations, the behavior is found to be more complicated and exponential fit-functions with coefficients depending on the contact angle and displacement are proposed. The results for a large radius converge as expected to the results obtained for the plate-plate geometry, however, results for small spheres reveal that a repulsive force can be obtained even for contact angles smaller than 90° at small separations. We also calculate the Laplace pressure, surface tension and total force for the whole range of displacements and contact angles for the plate-plate and sphere-plate configurations. These results are fundamental to an understanding of the enhancement of the force due to multiple small bridges between many small spheres and a plate. Color maps display the comparison of the total force due to multiple bridges for both situations.

## 5.2 Introduction

Capillary forces exerted by a liquid bridge between two surfaces have been extensively investigated experimentally and theoretically. The most common geometries were i) sphere-sphere[35, 43, 46, 71, 126-128, 162, 164], ii) sphere-plate [12, 47-50, 54, 60-65, 72-97, 125] and iii) plate-plate [24, 25, 27, 29, 39, 40] configurations. Studies based on different assumptions resulted in many approximations and rarely in a general model. In an earlier numerical study of the capillary force due to multiple liquid bridges [150], we have shown, for example, that the total capillary force of *n* bridges is maximized at moderately hydrophilic contact angles, i.e. *70*°, and not for

very hydrophilic substrates, as would be intuitively expected. We found good quantitative agreement between the results of the model and new experimental data for liquid bridges between two parallel plates [165]. Also the effect of different contact angles on the force-displacement curves was studied numerically [166]. These investigations were restricted to a plate-plate geometry.

The adhesion of a sphere in contact with a plate was studied by McFarlane and Tabor [47]. Their result for the adhesion force is

$$F = 4\pi\gamma_{lv}R\cos\theta\,, \tag{5.1}$$

where $\gamma_{lv}$ is the surface tension of the liquid, $R$ the radius of the sphere and $\theta$ the contact angle of the liquid on the plate. O' Brien and Hermann [75] extended this equation to

$$F = 2\pi\gamma_{lv}R(\cos\theta_1 + \cos\theta_2)\,, \tag{5.2}$$

where $\theta_1$ and $\theta_2$ are the contact angles of the liquid on the plate and on the sphere, respectively, to include dissimilar material properties. These equations became the reference for numerous research groups in the context of a humidity-dependent capillary force [48-50, 54, 76] and measurements of capillary adhesion and friction by atomic force microscopy [64, 77-83]. Further expressions were proposed based on the circular approximation of the curvature of the liquid-vapor interface [60-62, 84-88] and on numerical computations of the curvature [72-74, 89]. The circular approximation was shown to be valid for small liquid bridges [72-74, 89]. Furthermore, the sphere-plane geometry was also frequently used to model capillary forces on rough surfaces [63, 90-97]

However, this large body of literature has mainly focused on very specific problems that are often described by idealized conditions such as a sphere that is in immediate contact with a plate, numerical calculations for some selected contact angles but not for the whole range of

possible angles, the focus on only one liquid bridge instead of several adjacent ones as might occur on rough substrates or the fact that most often the size of a spherical substrate relative to the volume of the liquid bridge is neglected in quantitative descriptions.

In this work, we investigate theoretically how the radius of the sphere influences the force-displacement curve for a large range of radii and all contact angles. We calculate the force versus the sphere radius for different displacements and propose different fit-functions depending on the range of the displacements. Furthermore, we show how the Laplace pressure and surface tension terms behave for different contact angles and displacements for plate-plate and sphere-plate geometries. Based on these results, we extend the multiple bridge model proposed in [150] to a sphere-plate geometry.

## 5.3 Methods

We assume a liquid bridge, with a constant liquid volume *V,* between a rigid sphere of radius *R* and a flat substrate as shown in Figure 5.1.

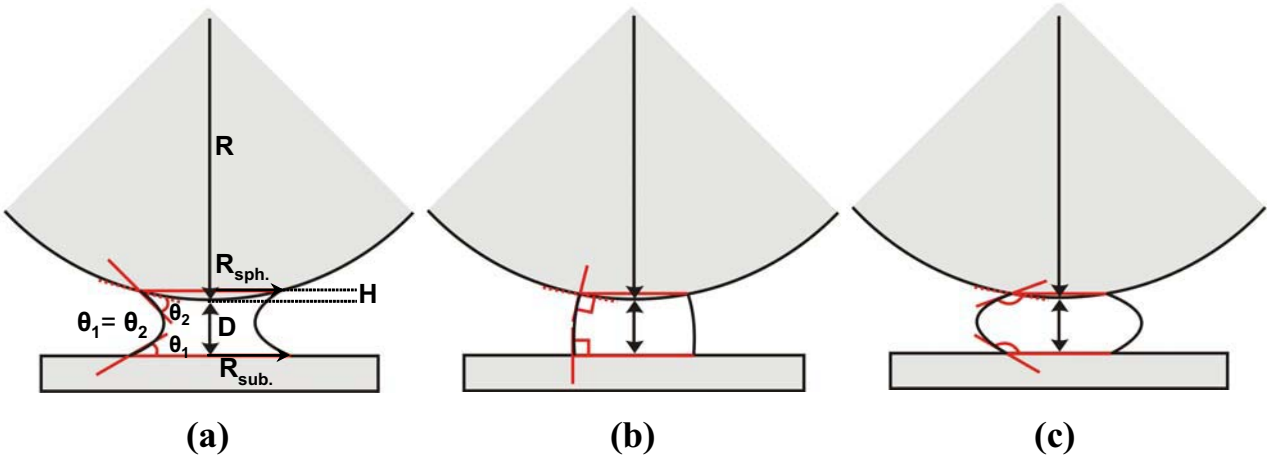


**Figure 5.1.** Schematic illustration of a liquid bridge wets between a spherical and a planar substrate with fixed contact angles $\theta_1$ and $\theta_2$. (a) illustrates the shape of the liquid-vapor interface for $\theta=30°$, (b) for $\theta=90°$ and (c) for $\theta=150°$. The radius of the sphere ($R$) is five times larger than the radius obtained from the volume $V$ of the liquid bridge. The radius on the substrate ($R_{sub}$), the radius on the sphere ($R_{sph}$) and the wetting height ($H$) for the separation $D$ between sphere and plate are obtained from numerical calculations of the total energy with Surface Evolver [108].

The surfaces are characterized by their contact angles $\theta_1$ and $\theta_2$, which are assumed to be identical: $\theta = \theta_1 = \theta_2$. The capillary force depends on the separation $D$, the surface tension $\gamma_{lv}$ of the liquid-vapor interface, $V$ and $\theta$. $R_{sub}$ in Figure 5.1 is the liquid-solid contact radius on the substrate while $R_{sph}$ is the same radius on the sphere. $H$ is the wetting height.

We calculate numerically the minimization of the total energy of the liquid bridge given by $E = \gamma_{lv}A_{lv}+(\gamma_{ls}-\gamma_{vs})A_{ls}$ using the software package Surface Evolver [108]. This software has been successfully used for earlier studies of plate-plate geometries [150, 165, 166] (chapters 2, 3 and 4 in this thesis). We will use in the following sections the same notations as in chapters 2 and 3.

The normalized total force is also obtained from the sum of forces arising from the surface tension ($f_{tension}$) and the Laplace pressure ($f_{Laplace}$) as given in [74, 125]. The surface tension contribution is calculated by $f_{tension}(d) = r(d)^2 sin(\theta)$, where the normalized radius of contact between liquid and solid $r(d)$ is a direct output from the numerical calculation. The normalized Laplace pressure can be calculated by subtracting the normalized surface tension contribution from the normalized total force. Following Carter [40] and our earlier study [150], we relate an attractive force to a positive Laplace pressure.

## 5.4 Results

### 5.4.1 Force versus displacement for fixed sphere radii

Figure 5.2a displays the normalized force as a function of the normalized distance for a plate-plate (solid lines) and sphere-plate (circles) geometry. The radius $R$ of the sphere is 1000 times larger than the radius $s$, set by the volume of the liquid bridge ($R = 1000 \cdot s$). This comparison shows excellent agreement for all contact angles, except for $\theta = 90°$ and very small displacements.

In Figure 5.2b the size of the sphere is reduced to $5 \cdot s$. Comparison between Figures 5.2a and 5.2b shows that this decrease of the radius of the sphere does not significantly affect the forces at large distances except for the case $\theta = 90°$.

Figure 5.3 shows the effect of the radius $R$ on the force-distance curves at small distances. For $\theta = 60°$, Figure 5.3a illustrates that for $R < 500 \cdot s$ the sphere-plate geometry (solid lines) strongly deviates from the plate-plate curves (circles). We note that the force approaches infinity for the plate-plate configurations while it converges to a finite value in the case of sphere-plate configurations. For $\theta = 120°$, Figure 5.3c shows a similar behavior, but with opposite sign. Further calculations for different $\theta$ values gave qualitatively the same results.

Interestingly, for $\theta = 90°$ an anomaly occurs (Figure 5.3b). This irregularity occurred also in Figure 5.2 a, b. Figure 5.3b shows in detail how the size of the sphere affects the behavior as $d$ approaches zero, the force becomes repulsive (negative) for all sphere radii; it is completely attractive (positive) for the plate-plate geometry. Stronger repulsive forces are observed for larger radii. The range of displacements for repulsive forces is smaller for larger $R$.

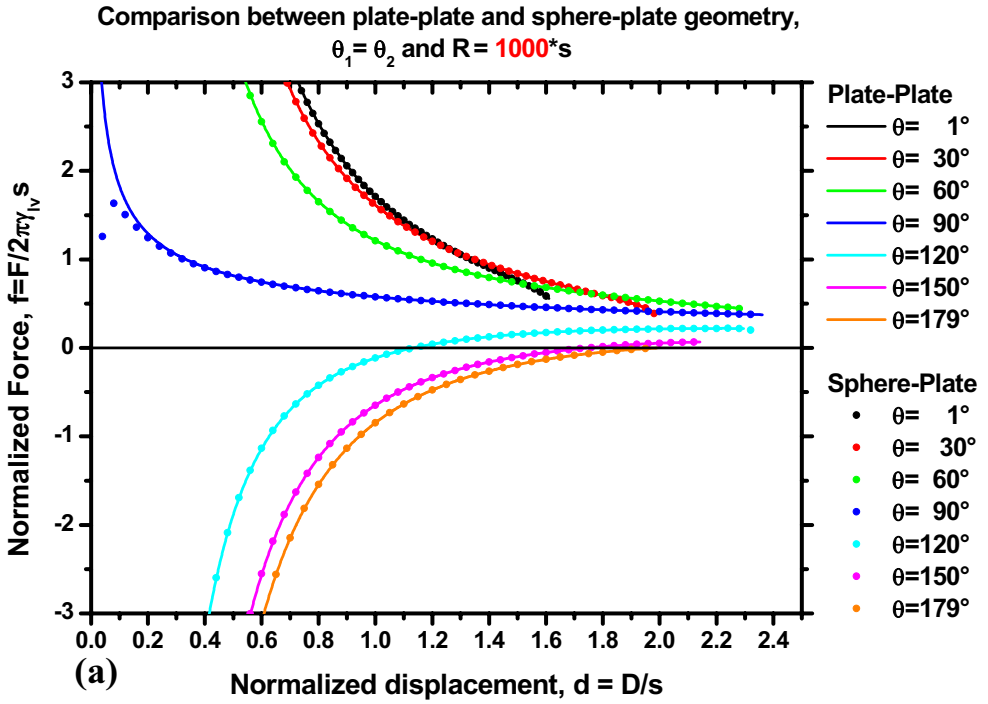


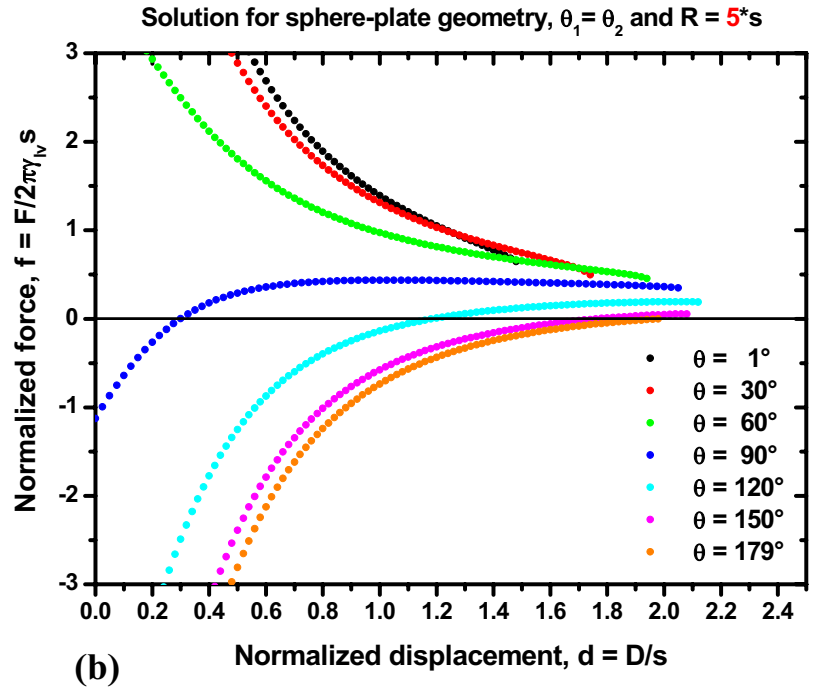


**Figure 5.2.** Numerical force versus displacement for hydrophilic $\theta \leq 90°$ and hydrophobic $\theta > 90°$ surfaces for two fixed sphere radii: (a) Comparison between results for plate-plate (solid curves) and a large sphere radius, $R = 1000 \cdot s$, (circles) demonstrates excellent agreement. (b) Results for a sphere-plate geometry with a sphere radius five times larger than the radius for the volume of the liquid bridge.

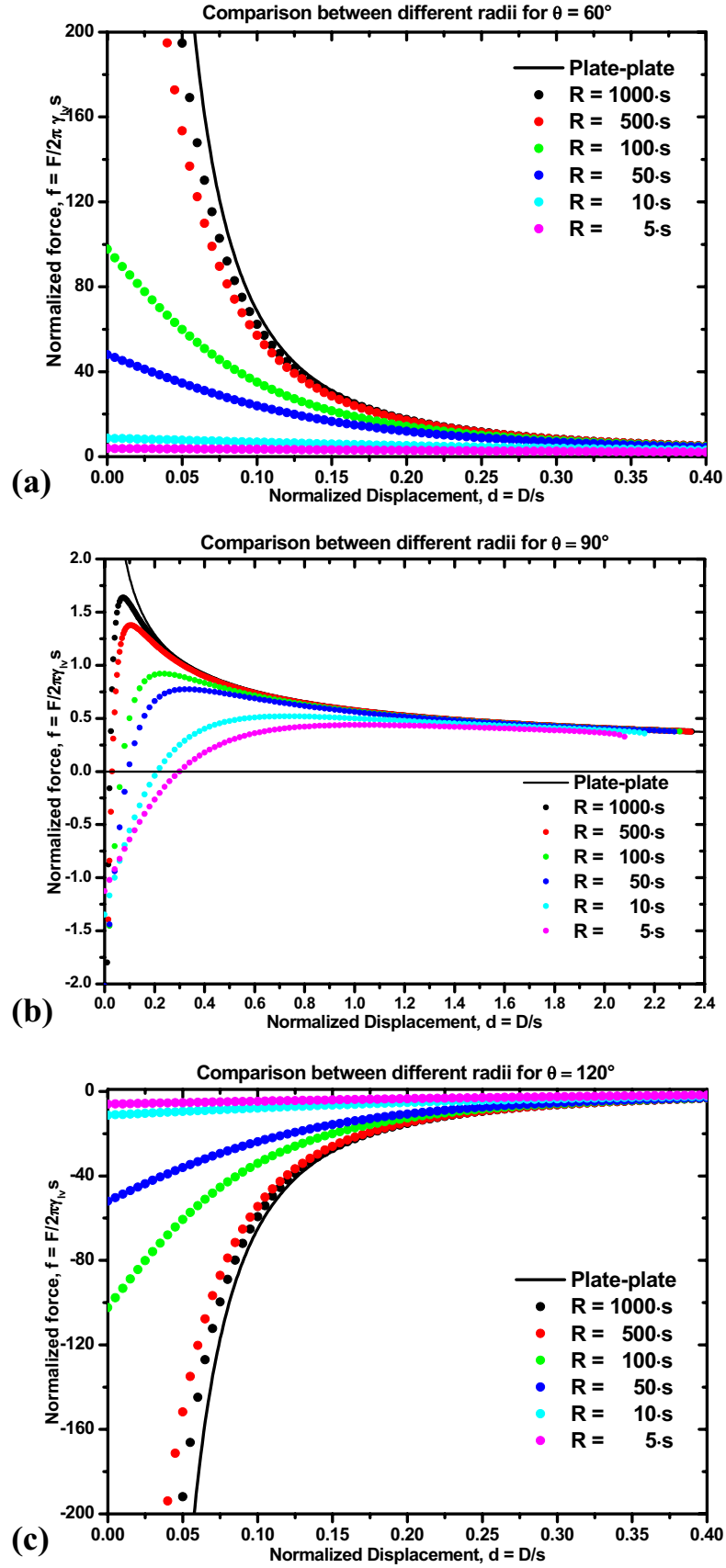


**Figure 5.3.** Examples of force-displacement curves for fixed contact angles and different sphere radii (circles). The range of force is appropriately chosen to highlight the comparison at small separations. (a) displays the results for $\theta$=60° (b) for $\theta$ = 90° and (c) for $\theta$ = 120°.

### 5.4.2 Force versus radius for fixed separations

It is instructive to display the forces as a function of the radius of the sphere at fixed normalized displacements (Figure 5.4). The numerical data (circles) are fitted with different functions (solid lines). For very small separations, the forces can be fitted by linear functions of the form:

$$f(R,d,\theta) = \beta \cdot R + f_0, \tag{5.3}$$

where $\beta$ is a contact-angle dependent slope given by $\beta(\theta)=2\cos(\theta)$, $R$ is the radius of the sphere and $f_0 = 0$. We also calculated the normalized force $f$ for larger distances and verified that the linear fit in Eqn. (5.3) holds up to separations of $d$=0.01.

Figure (5.4b) shows numerical results for an even larger separation of $d$=0.05. In this case, the normalized force can be fitted to the following exponential function:

$$f(R,d,\theta) = h(d,\theta) \cdot \exp(-R \cdot \delta(d)) + f_0 \tag{5.4}$$

where, $h(d,\theta) = \alpha(d) \cdot \beta(\theta)$ and $\delta(d)$ are displacement and contact-angle dependent functions, respectively. At this value of $d$, the fit function matches the numerical data very well for $\beta(\theta)=\cos(\theta)$ (Figure 5.4b) but there are no analytical expressions for $\alpha(d)$ and $\delta(d)$.

If the distance is increased to $d$ = 1, the numerical results can still be fitted by a fit function as given in Eqn. (5.4) (Figure 5.4c) but now the analytical expression for $\beta(\theta)$ is also unknown. Taken together, the comparison between numerical data and the exponential fit functions shows good agreement up to distances close to the maximal extension, i.e. point of rupture (results not shown).

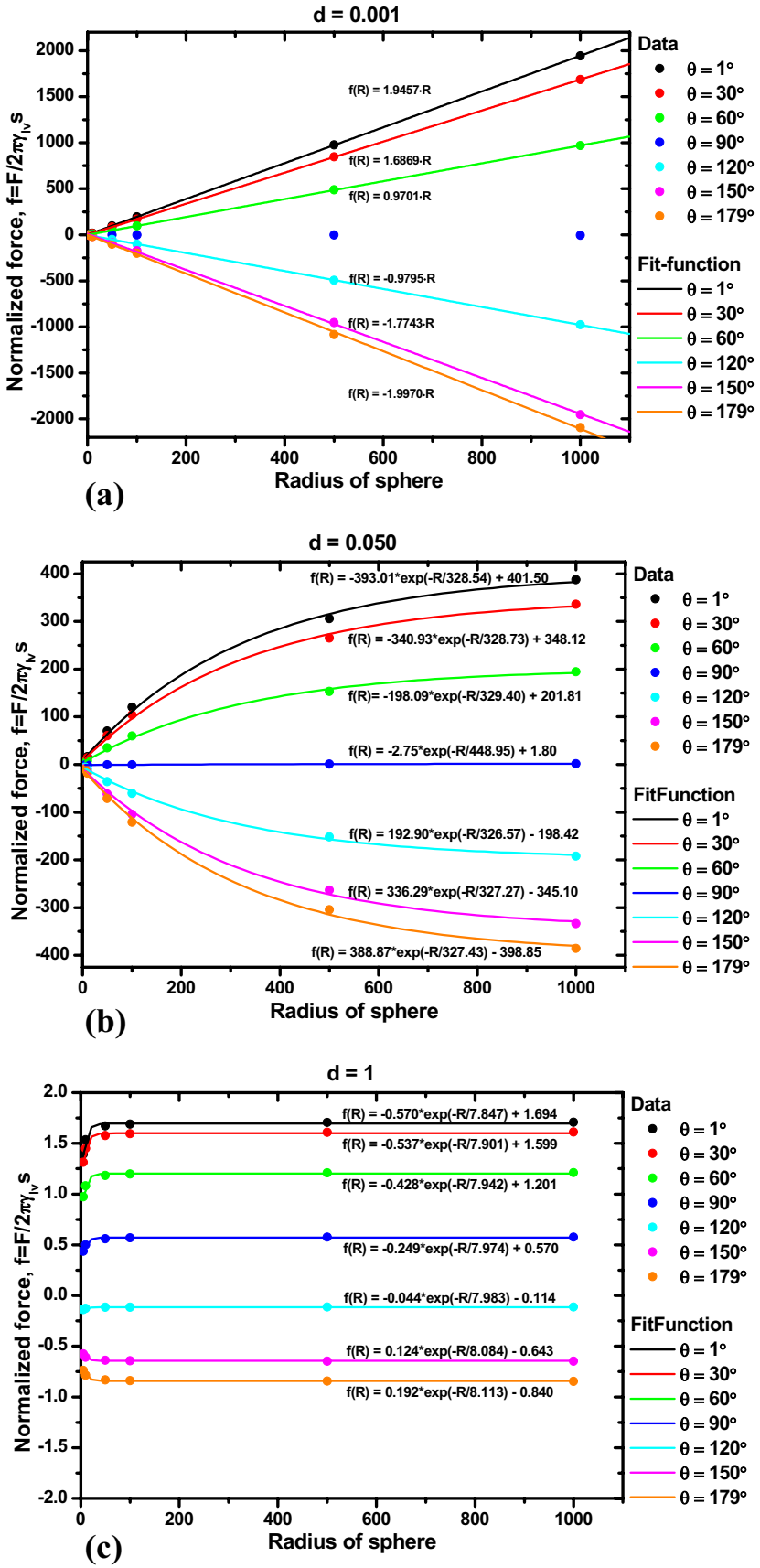


**Figure 5.4.** Force versus radius for fixed contact angles and fixed displacements. (a) displays the results for very small *d,* (b) for small and (c) for intermediate displacements *d*, respectively. Comparison between fit-functions (solid curves) and numerical data (circles) demonstrate a good agreement for these particular displacements.

### 5.4.3 Laplace pressure and surface tension for flat and spherical geometries

Figure (5.5) presents color maps of the behavior of the Laplace pressure (5.5a, d), the surface tension along the contact line (5.5b, e) and the total force (5.5c, f). As axes, we choose the contact angle $\theta$ and the normalized displacement $d$ (in steps of $\Delta\theta=5°$ and $\Delta d=0.001$). The color coding corresponds to different normalized force values. The continuous lines represent contours of equal force and the contour maked "0" describes the transition from attractive to repulsive forces.

First, we compare the Laplace pressure, surface tension and total force for the plate-plate geometry shown in Figure (5.5a, c). The Laplace pressure and the total force increase dramatically for separations $d < 0.5$, they approach positive infinity for $\theta < 90°$ and negative infinity for $\theta > 90°$. The Laplace pressure is positive over the whole range of displacements for $\theta < 20°$. Beyond this contact angle, it crosses the line of zero force and becomes negative for shorter displacements with increasing contact angle. For $\theta > 90°$, it is entirely negative. The total force, however, is positive for the whole range of displacements if $\theta < 90°$ and crosses the zero line from negative to positive values for $\theta > 90°$.

Comparing the isolines of the Laplace pressure with the isolines of the surface tension (Figure (5.5b)) for large separations, shows that the surface tension dominates the total force for this displacement regime. Therefore, since the surface tension is always attractive (positive), it results in an attractive total force at large separations, even for super-hydrophobic surfaces. Note that the Laplace pressure decreases much faster to small values than the surface tension. The white color at large separation represents the rupture of the liquid bridge.

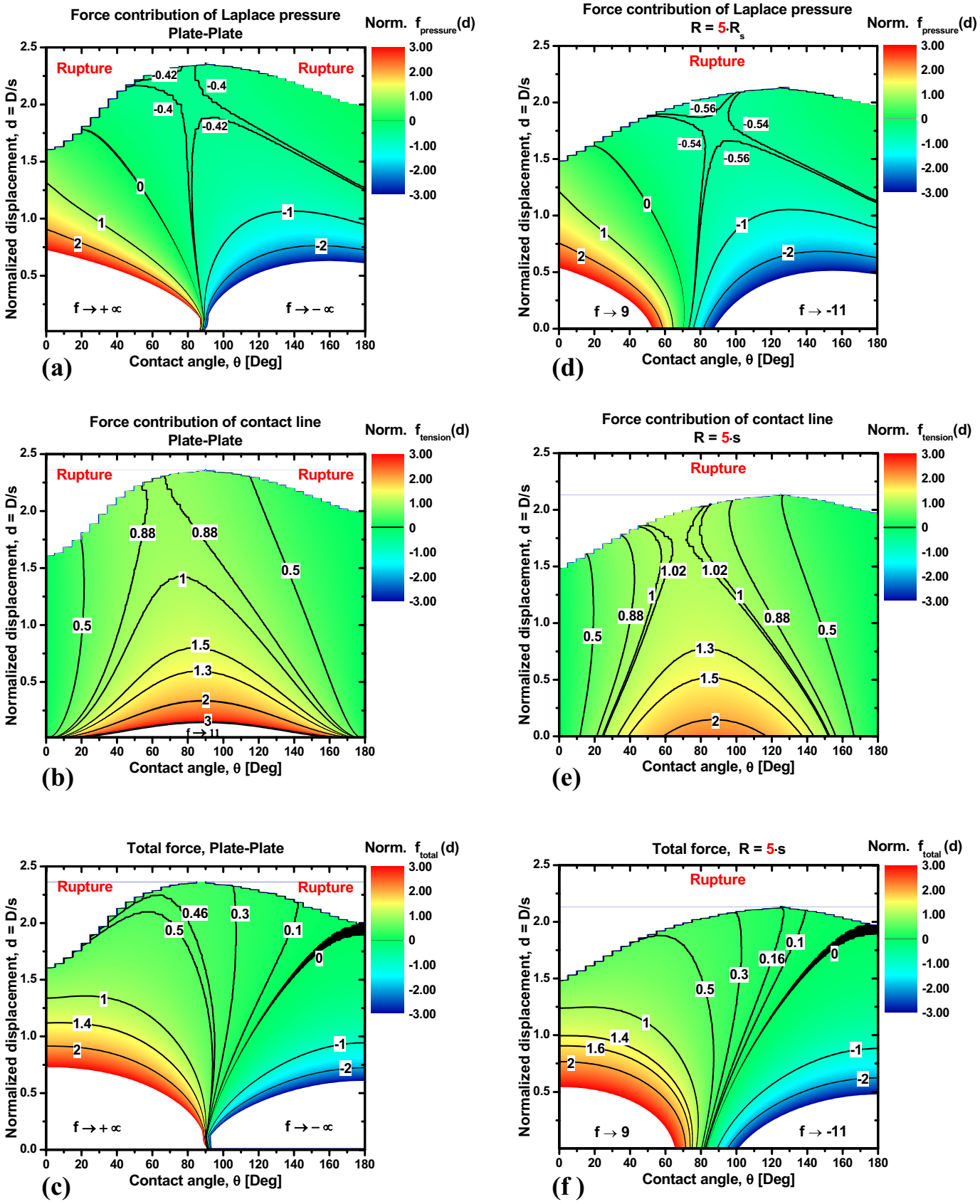


**Figure 5.5.** Map of force contributions to the total capillary force. (a), (b) and (c) are the Laplace pressure, surface tension and total force, respectively, for the plate-plate geometry. (d), (e) and (f) are the force contributions in the same order for the sphere-plate geometry.

In the case of a sphere-plate geometry, the Laplace pressure (Figure (5.5d)) and consequently the total force (Figure (5.5f)) assume finite values at close separations. Besides, the Laplace pressure decreases to more negative forces at large separations than the forces obtained for the plate-plate geometry at the same regime of distances. The opposite occurs for the surface tension.

Comparing Figure (5.5b) with (5.5e) at large separations, shows that the surface tension contribution for the sphere-plate geometry is more positive than that for the plate-plate. Comparison of the maximal extension of the liquid bridge between plate-plate and sphere-plate geometries, for example, (Figure (5.5 c) and (5.5f)), shows that the rupture occurs at larger distances for plate-plate than for sphere-plate arrangements and that the maximum separation occurrs for $\theta=90°$ for two plates and for $\theta=125°$ for a sphere and a plate.

The Laplace pressure and the total force shown in Figure (5.5 d) and (f) at small separations differs strongly from the Laplace pressure shown in Figures (5.5 a) and (c) for a contact angle approaching 90°.

To visualize this difference, we display in Figures (5.6 a) and (b) two dimensional force-displacement curves of solutions for plate-plate and sphere plate geometry for contact angles approaching 90° from the right and left side. Comparison of these pictures shows that the mentioned anomaly of the previous section (Figure (5.3c)) does not occur exclusively for $\theta=90°$ but for all contact angles around $\theta=90°$. It shows that repulsive forces occur even for $\theta < 90°$ if the separation and the sphere radius are both very small.

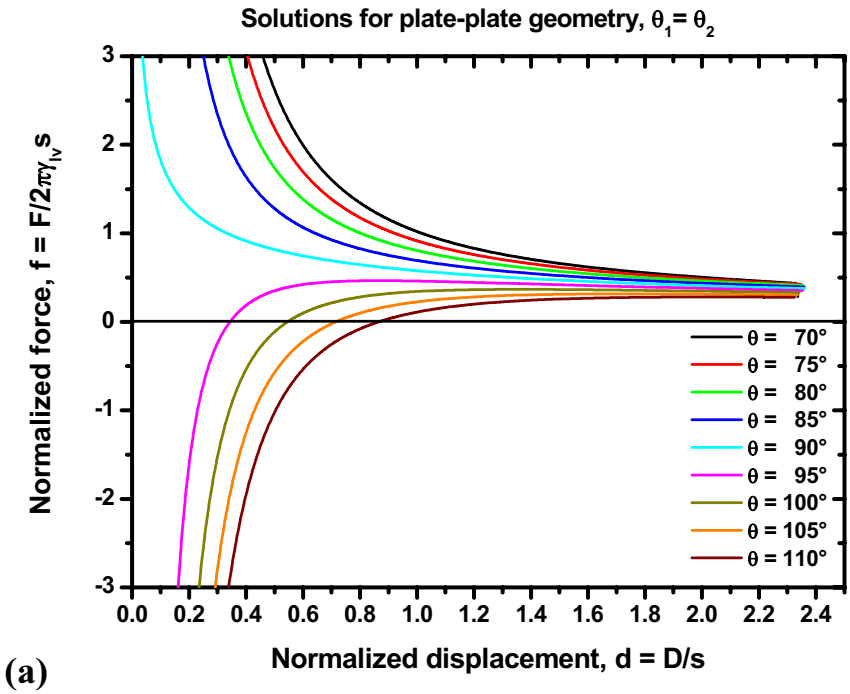


(a)

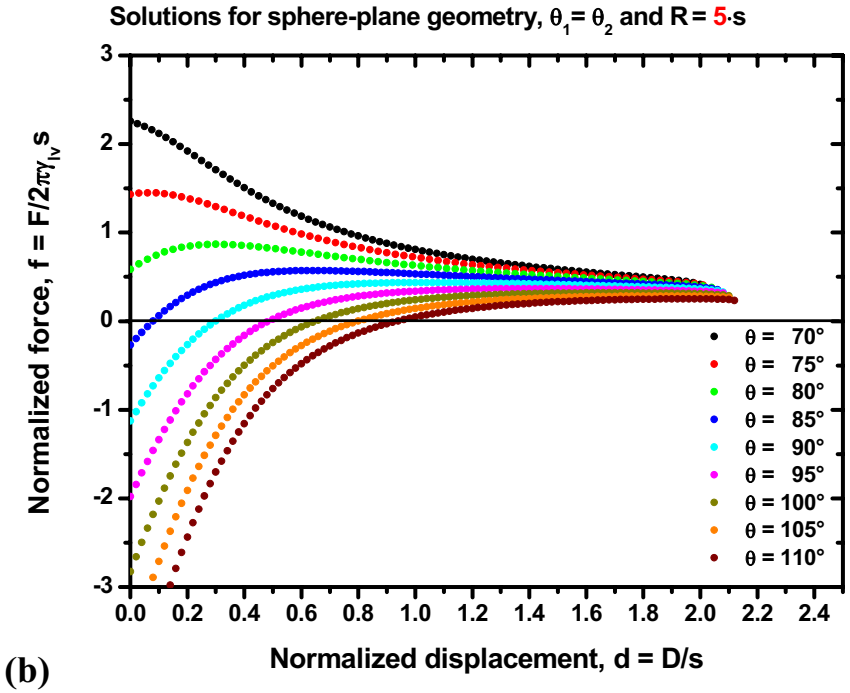


(b)

**Figure 5.6.** Comparison of force-displacement curves between a plate-plate and a sphere-plate geometry for a small sphere radius *R = 5 s* and restricted range (*70°-110°*) of contact angles. The figures are details of Figure s (5c) and (5f) represented as two-dimensional curves. (a) Results for the plate-plate and (b) the sphere-plate geometry, respectively.

### 5.4.4 Extended maps of multiple liquid bridges

We now consider the effect of splitting one large liquid bridge between a sphere and plate into *n* smaller bridges with the identical ratio *Q=R/s*, i.e. a self-similar splitting into *n* equal bridges of volume *V/n* as schematically shown in Figure 5.7.

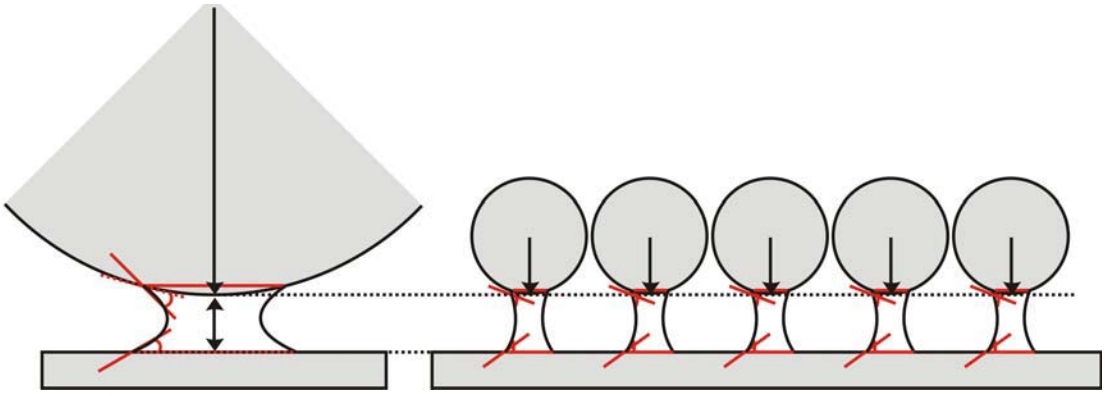

**Figure 5.7.** Schematic of splitting one liquid bridge into *n* smaller liquid bridges of equal size. The total volume of the liquid, the ratio *R/s* and the separation of the substrates are equal in both cases.

In the subsequent calculation it is assumed that the individual bridges do not interact or coalesce. This situation could be realized experimentally by chemical patterning of the substrate.

- **Map of force**

To calculate the total force of *n* non-interacting bridges, we proceed as described in [150]. We start from the absolute force for one liquid bridge (Eqn. 2.5d). If *V* decreases to *V/n*, the scaling factor *s* and the normalized distance *d* change in the following way: *s* becomes $s_n = s\, n^{-1/3}$ and *d* becomes $d_n = d\, n^{1/3}$. For *n* liquid bridges the total absolute force at distance *d* is therefore given by:

$$F_n(d) = 2\pi \cdot n\gamma_{lv} s_n \cdot f(d_n) = 2\pi \cdot n^{2/3}\gamma_{lv} s \cdot f(d_n) \qquad (5.5)$$

Note that the absolute separation $D$ of the substrates and the ratio $Q=R/s$ have not changed. To provide a direct comparison between sphere-plate and plate-plate geometry we replot in Figure (5.8a) the results for the plate-plate configuration published in [150] . The dependence of this total force on $n$, $\theta$ and $R$ is displayed in Figure (5.8b), using $\gamma_{lv}=72.8\ mN/m$ for the water-air interface, $V=1\ \mu l$, $D=15\ \mu m$ and $R=5\cdot s$.

As axes, we choose the contact angle $\theta$ and the number $n$ of bridges that vary in steps of $\Delta\theta=5°$ and $\Delta n=1$, respectively. The color coding corresponds to different total force values. The continuous lines represent contours of equal force (labeled in Newtons); the heavy black contour marks the transition from attractive to repulsive forces. The fields labeled "rupture" correspond to situations for which the liquid bridges are no longer stable.

First, an enhancement of the total force is seen as the number of bridges (spheres) increases. Comparison between Figures (5.8a) and (b) reveals that the total force for the sphere-plate configuration is decreased with respect to the plate-plate configuration. The maximal forces between two plates is about $1.15\ N$ for $\theta \sim 70°$ (Figure 5.8a), while the maximal force for the sphere-plate geometry is about $0.838\ N$ for $\theta \sim 50°$ (Figure 5.8b). Close inspection shows that the isolines for the total forces F < 0.505 N are quantitatively very similar for the same number of bridges and contact angles. The comparison also shows that the possible number of bridges is reduced for the sphere-plate geometry: the "rupture" field is larger.

- **Map of stress**

To calculate the stress we divide the total force $F_n$ for $n$ liquid bridges by the total area $A_n$ obtained from the sum of the projections of the equatorial areas of the $n$ spheres onto the bottom substrates, i.e. the area necessary to accommodate $n$ adjacent spheres. The stress shown in Figure 5.9 is maximal for strong hydrophilic surfaces and one liquid bridge (red area near $\theta=0°$).

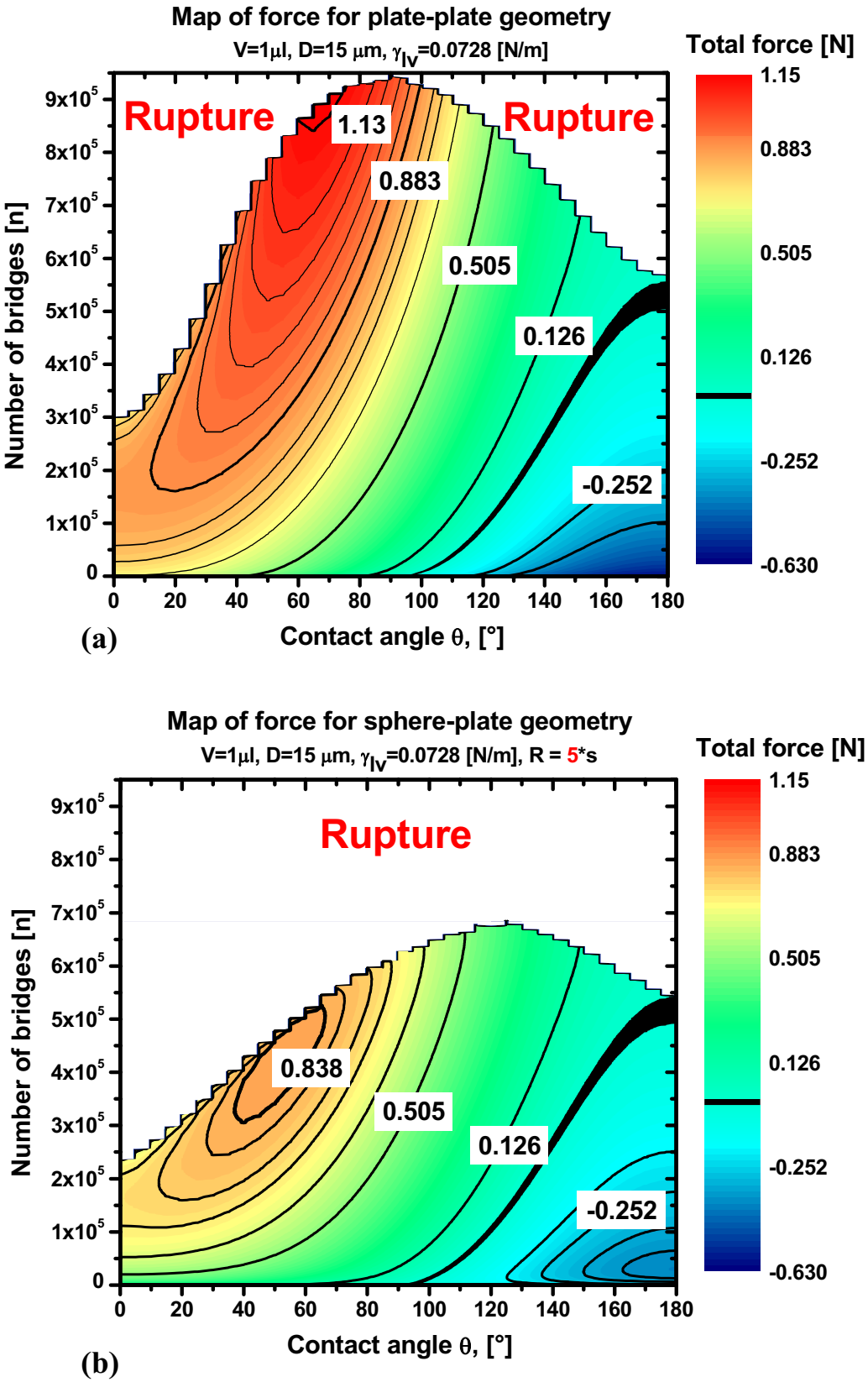


**Figure 5.8.** Map of the total force versus the contact angle $\theta$ and the number of liquid bridges. The black contours are lines of equal force, some of which are labeled in [N] for a better visualization. The graphs (a) and (b) display a comparison between a plate-plate and a sphere-plate geometry for a constant ratio ($Q = 5$) between sphere-radius and bridge-radius.

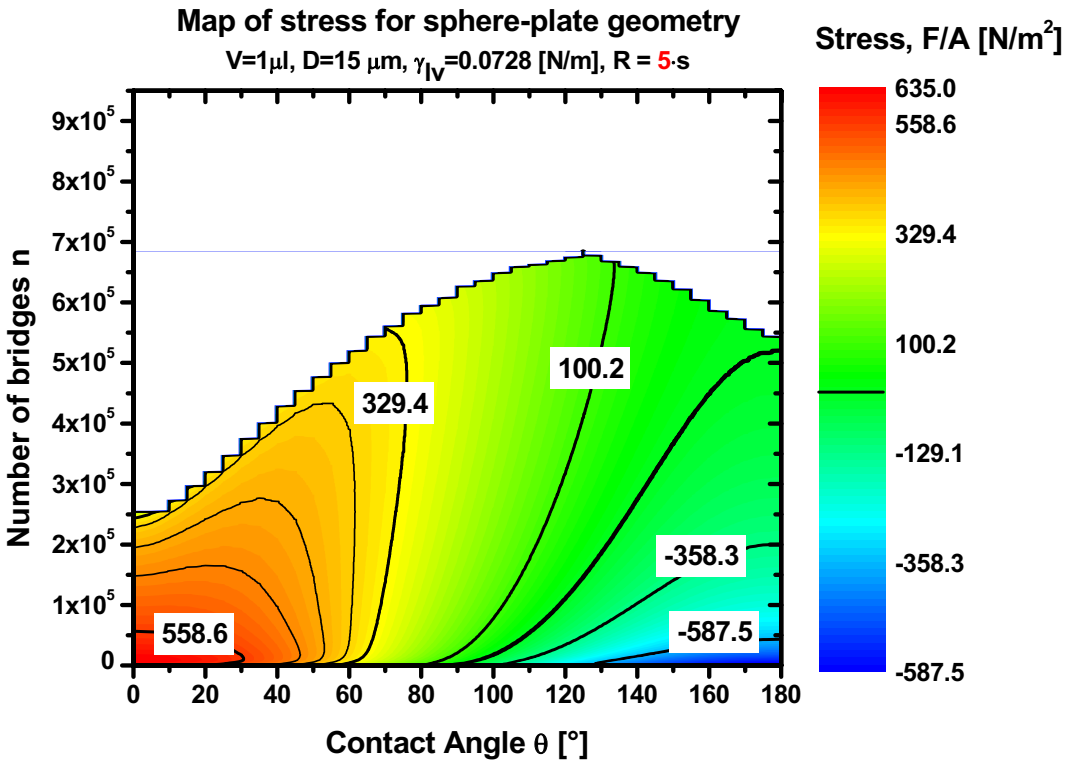


**Figure 5.9**: Map of the stress versus the contact angle and the number of bridges. Isolines are labeled in [N/m$^2$]. The stress is calculated as total force of *n* bridges divided by the total area necessary to accommodate the *n* adjacent spheres, i.e. the total area that results from projecting all spheres onto the lower substrate.

## 5.5 Discussion

### 5.5.1 Forces-displacement curves for large and small separations

- **Large separations**

Comparison between plate-plate (solid curves) and sphere-plate (circles) results in Figure 5.2a demonstrates excellent agreement. It is reasonable to assume that the energy minimization with Surface Evolver is reliable over the whole range of contact angles. This finding justifies the application of the numerical minimization method to systematically investigate the size effect of the sphere on the force-displacement curves, as demonstrated in Figure 5.2b. The qualitative similarity between Figures 5.2a and 5.2b at large distances (except for $\theta = 90°$) indicates that a liquid bridge is not sensitive to the size of the sphere in this regime. Since the surface tension dominates the total force at large separations, it follows

from our observations that the surface tension is also insensitive to the size of the sphere at large separations.

- **Small separations**

As mentioned in the introduction, the sphere-plate model has been frequently used to model capillary condensation and other adhesion experiments, however, the effect of the ratio *R/s* has been rarely taken into account. Our results in Figure 5.3 clearly show that this ratio has indeed a very large effect on the total force. In particular, Figure 5.3a shows that for $R/s \geq 500$ the sphere-plate geometry can be approximated by a plate-plate geometry, which is easier to handle numerically because less parameters are needed to describe this configuration. There are many experimental situations with $R/s \geq 500$, such as for example in [52], where such approximations would be meaningful. Our results in Figure 5.3a are therefore helpful in choosing an appropriate geometric model to quantitatively describe experimental results. If, for example, a liquid volume is of the order of $10^{-15}$ $m^3$, as occurs during capillary condensation, and a spherical substrate is of the order of few mm, then it follows that $R/s \approx 500$. Our results suggest that this situation can be approximated by a plate-plate geometry which is very convenient in experimental measurements of the total force.

- **Anomaly for $\theta = 90°$.**

The repulsive force shown in Figure 5.3b demonstrates the importance of knowing the exact contact angle to compute the total force. It is frequently assumed that the force for $\theta = 90°$ is completely attractive between a sphere and a plate, our results however shows that attractive forces can be obtained only if *R* approaches very large values. Furthermore, this effect may be difficult to observe experimentally because it occurs at very small separations and specific contact angles.

### 5.5.2 Fitting results

- **Linear fit**

By plotting the slope observed in Figure 5.4a versus the contact angles (results not shown), we obtained $\beta(\theta)=2\cos(\theta)$. Thus, insertion of equation (5.3) in equation (2.5d) yields:

$$F(R) = 4\pi R\cos(\theta)\gamma_{lv}(3V/4\pi)^{\frac{1}{3}}. \qquad (5.6)$$

Up to the volume term, this result is identical to the previous observations in [47] and demonstrates the accuracy of our numerical model at very small separations, which is not evident in earlier numerical solutions [72-74, 89].

- **Exponential fit**

The fact that $\beta(\theta) = \cos(\theta)$ for $d = 0.05$ in Eqn (5.4) does not hold for larger separations as shown in Figure 5.4c. This indicates that it is difficult to propose a global quantitative model that fits the results for a large range of different values of $d$. Even if such a model existed, the physical interpretation of its coefficients would most likely remain elusive. Numerous quantitative approximations presented in earlier studies did not consider the effect of the sphere radii and contact angles for all separations. Consequently, there are no comparable fit functions in the literature. We therefore suggest more experimental investigations to support our fits and to possibly give physical meanings to the fit coefficients.

### 5.5.3 Laplace pressure and surface tension for flat and spherical geometry

The "landscapes" shown in Figure 5.5 have interesting topographies, because they characterize the liquid bridge between two substrates when one pulls them together or pushes them apart. By reading off the Laplace pressure, one can deduce how the liquid-vapor

interface is being deformed, while the surface tension describes how the contact line moves. In general, the Laplace pressure governs the total force at small separations while the surface tension plays the dominant role at larger separations.

As opposed to the plate-plate configuration, where the contact line can expand indefinitely outwards, the contact lines are constrained by the spherical shape of one substrate. Thus, the liquid bridge starts to “feel” the size of the sphere as it approaches the plate. The response of this curvature results in a repulsive force even for contact angles smaller than 90°.

The Laplace pressure is more strongly repulsive (negative) at large separations for the sphere-plate geometry than for the plate-plate configuration. Interestingly, the surface tension is more strongly attractive (positive) for the sphere-plate geometry than for the plate-plate geometry at the same large separations. We suggest that the combination of these effects explains why the rupture occurs at smaller separations for the sphere-plate geometry than for plate-plate configurations.

Geometric and size effects in the context of different substrate shapes and relative humidities have been investigated in earlier studies [68, 167-170]. However, the size effect of the sphere relative to the size of the liquid bridge is not investigated in the present literature. To our knowledge, a complete overview of the influence of contact angles and substrate geometries on the force-displacement curves has not been published so far. The map of force contributions due to the Laplace pressure and the surface tension for plate-plate and sphere-plate geometries are also completely new results. Besides the completeness, the results shown in Figure 5.5 are the basics for understanding the effects described in [150].

### 5.5.4 Map of total force and stress

- **Map of total force**

In the context of improving adhesion, the map of the total force due to multiple bridges for the sphere-plate geometry reveals that the enhancement of force is moderately reduced if compared to the map of force for the plate-plate geometry. In the case of artificial attachment devices, this result suggests that capillary adhesion is stronger for a plate-plate arrangement. Such configurations would occur, for instance, for capillary bridges between pillars with flat tip geometry as described in [171]. Also some biological systems, as for example the attachment organ of flies [6-8], resemble a plate-plate geometry rather than a sphere-plate geometry.

On the other hand, reduction of adhesion is desired in many technical application as described in [63]. Previous investigations addressed the effect of roughness on the capillary force [92-94] and even the hypothesis of multiple bridges [90, 92, 96, 97]. However, it was not known how the number of bridges affects the total force for arbitrary contact angles. Therefore, the map of total force due to multiple liquid bridges for sphere-plate geometries presents a helpful new tool to minimize the adhesion and stiction by controlling the number of asperities and the contact angles of the substrates.

Our results are also qualitatively consistent with a previous experimental observation of a two dimensional curve of the total force versus the number of bridges as shown in [97]. This result was obtained by sliding an AFM tip with radius $R \sim 10\ nm$ on a hydrophilic rough surface of glass. Water bridges can form between the tip and the asperities of the surface resulting in a total force $F_n$ proportional to $n^{2/3}$. This observed power law represents a stripe in our color map for a very specific condition and therefore direct comparisons cannot be made.

- **Map of stress**

The maximal stress for strongly hydrophilic surfaces and one liquid bridge demonstrates that Contact splitting is not an efficient method to maximize the adhesion if the available area for adhesion is limited. This is in contrast to a plate-plate geometry. The reason is that here, for a given separation, i) the maximal force is obtained for the minimal contact angle (very hydrophilic substrates), and ii) the total projected area obtained by splitting a large spherical contact does not depend on the contact angle and increases with the number of bridges. The highest stresses are thus obtained for $\theta \approx 0°$, and $n \approx 1$, which corresponds to the red region in Figure 5.9.

This too indicates that hierarchical biological attachment devices rather resembles a plate-plate geometry than a sphere-plate geometry, because they make use of contact splitting and require a strong adhesion for a limited contact area.

## 5.6 Conclusions

The results presented in this work reveal the importance of the ratio of the sphere relative to the volume of the liquid bridge. This ratio changes the behavior of the force-distance curves in different ways depending on the separation. We have shown, for example, that repulsive forces can be obtained for $\theta < 90°$ and small sphere radii.

We reproduced previous results for a sphere in contact with a plate and extended the description of this configuration to all separations. The exponential fits proposed here are very accurate and convenient but require experimental verifications.

For the first time, contributions due to the Laplace pressure and the surface tension are displayed for all distances and contact angles. These maps do not only give an overview of

the contributions to the total force, but also help to understand the effects observed for multiple liquid bridges.

Finally, the calculation of a map of the total force due to multiple liquid bridges for sphere-plate geometries has shown that an enhancement of the force is also present for this case. This map can be very instructive in designing artificial adhesive systems where, for example, the capillary adhesion due to surface asperities is to be minimized.

# 6 Summary and outlook

Earlier studies of the effect of capillary forces on adhesion have revealed that it remains difficult to this date to derive a general model of capillarity that is based on realistic conditions such as i) different chemical properties and different geometries of the substrates, ii) more then one liquid bridge between the substrates and that applies to a large range of possible distances. The idealized conditions studied previously left many open questions that are important for the qualitative and quantitative understanding of how liquid bridges behave generally. The investigations in this work go beyond the limits presented in the literature and offer a more general view of capillarity.

We have shown that the force exerted by multiple liquid bridges does not scale linearly with the number $n$ of bridges, as might be intuitively assumed. Instead, two scaling regimes are found: for a contact angle $\theta \leq 52°$, the force exhibits a maximum at some intermediate value of $n$, while for $\theta > 52°$, it increases monotonically with $n$. In both cases, however, does contact splitting lead to an enhancement of the force as compared to only one bridge. The overall maximum of the force occurs for moderately hydrophilic surfaces with contact angles of $\theta \sim 70°$ *and not* for strongly hydrophilic surfaces as expected at first glance. Color maps calculated for the stress and the energy of separation of the substrates show that the maxima are shifted towards contact angles of 90° and many bridges and towards very small angles and only one bridge, respectively. These maps can be helpful tools to optimize engineered functional surfaces.

In view of biological attachment systems, the maps suggest that animals may indeed apply the mechanism of liquid bridge splitting, because many small bridges can lead to stronger adhesion than a single bridge, which is especially important for adhesive systems operating in

the regime of large distances, i.e. close to the point of rupture. Furthermore, animals most likely have the capability to adjust the amount of liquid that is secreted to their attachment organs and to control the number of bridges that are in contact. Both parameters may serve as control parameters that can modify the capillary force and even switch it from attractive to repulsive and vice versa.

The calculations of the capillary force for different contact angles show that the force between very hydrophilic and moderately hydrophobic surfaces is attractive over the whole range of distances. On the other hand, the point of rupture (maximal possible separation) is maximal for identical contact angles and decreases with increasing degree of contact angle asymmetry. These results may have important consequences for biological attachment devices, where the contact elements, of insects for example, are assumed to be strongly hydrophilic while the substrates to which they attach can range from hydrophilic to strongly hydrophobic. Our results suggest that this is not necessarily a problem, because very hydrophilic contact elements provide attractive interactions with a large class of substrates ranging from hydrophilic to hydrophobic. On top of that, a large contact angle asymmetry has the additional advantage of small rupture distances and thus of easy detachment from the substrate whenever necessary.

Comparison between our numerical calculations and measurements of the capillary force for one bridge between two parallel plates demonstrates the high accuracy of the numerical model. This allows to use fits of the numerically calculated force-distance curves to measured ones in order to determine the dynamic contact angles at both substrates, thereby providing a new and accurate method to evaluate the contact angle hysteresis. This method is very flexible and can also be applied to super hydrophobic surfaces which are otherwise very difficult to analyze with standard techniques.

Calculation of the capillary force between a sphere and a plate shows that in this case the additional parameter describing the size of the sphere relative to the volume of the liquid bridge is very important and affects the force-separation curves. As opposed to the plate-plate configuration, it is shown that the force converges to finite values for $d \rightarrow 0$, that it can become repulsive even for $\theta < 90°$ as the size of the sphere approaches that of the liquid bridge and that the maximal rupture distance decreases and shifts from $90°$ to larger contact angles with decreasing sphere size. If the sphere is more than 500 times larger than the bridge, our results suggest that a sphere-plate configuration can be approximated well by a plate-plate configuration. Color maps of the Laplace pressure and the surface tension for plate-plate and sphere-plate geometries are very helpful in understanding the role of the individual contributions to the total force for all separations and contact angles. The results of contact splitting show that an enhancement of the force is still present but it is reduced as compared to two planar substrates and it decreases with decreasing radius of the sphere. The maximal total force is shifted to $\theta \sim 50°$ for a sphere 5 times larger than the individual bridges and the stress is maximal for very hydrophilic substrates and one bridge.

In future work, it would be very interesting to measure experimentally the capillary force due to multiple liquid bridges for plate-plate and sphere-plate geometries. To this end, macroscopic liquid bridges could be considered with dimensions comparable to those used for the study of one bridge in chapter 4. This would allow to systematically investigate the combined effects of the contact angles and the number of liquid bridges and thus to verify the calculated maps of force and stress. On the level of microscopic dimensions, capillary condensation could be studied experimentally with a sphere-plate geometry. This would allow to verify the effect of the relative size of the sphere and whether the forces is repulsive for contact angles $\theta < 90°$, as theoretically predicted. The exponential fits of the forces as a function of the sphere radius at large separations, as proposed in chapter 5, could also be

inspected experimentally to understand the physical meaning of the coefficients better. Such investigations would surely provide new aspects of the capillary force and open new directions for its application not only in view of adhesion but also to design functionalized surfaces and to explain complex phenomena observed in micro fluidic devices.

# Deutsche Zusammenfassung

**Motivation**

Die Motivation für diese Arbeit beruht zum einen auf dem großen wissenschaftlichen und technischen Interesse an Bindungs- und Haftphänomenen, sowie zum anderen darauf, dass – obwohl bereits im 18 Jahrhundert begründet – die Theorie der Kapillarität bis heute fundamentale, ungeklärte Fragen enthält.

Die Haftung und Reibung zwischen zwei Substraten, bei denen Wasser oder eine wässrige Lösung eine Rolle spielt, wird als „nasse Haftung“ bezeichnet, im Gegensatz zur „trockenen Haftung“, bei der keine Haftkraft-vermittelnde Flüssigkeit existiert. Die quantitative Untersuchung der nassen Haftung sowie der Benetzbarkeit von Substraten wurde in den sechziger Jahren initiiert [115, 116] und hat sehr an Auftrieb gewonnen, nachdem die nasse Haftung als Hauptursache für das Versagen von Festplatten identifiziert wurde [65]. Zusätzlichen großen Impuls hat dieses Forschungsgebiet während der letzten 10 Jahre erfahren, als die Haftorgane und die Haft- oder auch Antihaftmechanismen einiger Tiere und Pflanzen systematisch untersucht worden sind, um z.B. zu beantworten, wie einige Insekten und Geckos auf vertikalen, glatten Oberflächen haften und laufen können. In vielen Fällen hat sich dabei herausgestellt, dass nasse Haftung, eine wesentliche Rolle bei der Adhäsion von tierischen Haftorganen auf Substraten spielt. Dies ist z.B. bei Baumfröschen der Fall [3-5], die ein flüssiges Sekret zwischen Fuß und Substrat bilden, oder auch bei einigen Fliegen [6-8]. Sogar beim Gecko, bei dem die molekulare Anziehung durch sehr viele nanometergroße, haarartige Haftorgane vermittelt wird [9, 10], weisen Experimente daraufhin [9], dass die Haftkraft mit wachsender relativer Luftfeuchtigkeit zunimmt.

Das Verstehen der Haftmechanismen in biologischen Systemen ist aber nicht nur von

wissenschaftlichem, sondern darüber hinaus auch von technischem Interesse. Es existieren bereits mehrere biomimetsiche Konzepte zur Übertragung der Struktur und der Funktionsweise biologischer Haftsysteme auf technische Systeme. Ein Beispiel hiefür sind mikro-strukturierte Polymeroberflächen [103].

Um biologische und technische Haftsysteme verstehen, bzw. entwickeln zu können, müssen einige fundamentale Fragen der nassen Haftung geklärt werden. Dazu gehört z.B., wie die Kapillarkraft zwischen zwei Substraten, die durch eine flüssige Brücke zwischen ihnen vermittelt wird, durch Randbedingungen und Substrateigenschaften beeinflusst wird. Die chemischen Eigenschaften eines Substrates werden dabei durch den Kontaktwinkel $\theta$, der sich zwischen der Flüssigkeit und dem Substrat ausbildet, charakterisiert. Streng genommen ist dieser Winkel nur in statischen Fällen eine Konstante. Wenn sich dagegen die Substrate relativ zueinander bewegen, d.h. die flüssige Brücke entweder gedehnt oder gestaucht wird, dann variieren die Kontaktwinkel an beiden Substratoberflächen in Abhängigkeit von der Richtung der Relativbewegung. In diesem Fall spricht man von dynamischen Kontaktwinkeln.

Es existieren viele Modele zur Berechnung der kapillaren Kraft, die den Einfluss der Substratgeometrie berücksichtigen. So gibt es Arbeiten zu Platte-Platte Konfigurationen [21-42], Kugel-Platte [12, 47-64, 66-69, 72-76] und Kugel-Kugel [43-46, 70, 71] Geometrien sowie weiteren, unterschiedlichen Geometrien [68]. Auch der Einfluss der relativen Luftfeuchtigkeit [47-59] und der Materialeigenschaften der Substrate [60-64, 66] sind untersucht worden. Dass trotz der umfangreichen Literatur wichtige Fragen noch ungeklärt sind, hängt zum Teil damit zusammen, dass analytische Berechnungen der Kapillarkraft wegen des großen Parameterraumes entweder nicht möglich oder kompliziert und unanschaulich sind. Außerdem werden in vielen quantitativen Beschreibungen idealisierte Bedingungen

angenommen. Z.B. werden statische Kontaktwinkel vorausgesetzt, obwohl dynamische realistischer wären, oder es werden idealisierte Geometrien angenommen oder Größeneffekte der Substrate vernachlässigt. Dies führt dazu, dass es bis heute keine einheitliche Theorie der Kapillarität gibt, die auf alle Flüssigkeiten, Substrate und Längen-und Zeitskalen anwendbar ist.

In der vorliegenden Arbeit sind numerische Berechnungen und experimentelle Messungen der Kapillarkraft angestellt worden, die auf allgemeineren Annahmen beruhen, als es bisher in der Literatur geschehen ist. So wird z.B. der Fall behandelt, dass sich an den Substraten unterschiedliche Kontaktwinkel ausbilden, d.h. dass die Substrate unterschiedliche Eigenschaften haben, wie man es in einem natürlichen Haftsystem erwarten würde. Desweiteren wird berücksichtigt, dass die Kontaktwinkel sich ändern können und dass die Substrate verschiedene Geometrien haben können. Im Hinblick auf biologische Haftsysteme wird erstmalig untersucht, wie sich eine Aufspaltung der Kontaktfläche in mehrere kleine Kontakte auf die Gesamtkraft auswirkt. Die erzielten Ergebnisse erweitern das Verständnis von der kapillaren Adhäsion und ermöglichen neue Interpretationen biologischer Haftsysteme sowie interessante Vorhersagen zur Anfertigung künstlicher Systeme. Im Folgenden werden die wichtigsten Ergebnisse und ihre Bedeutung für Haftsysteme erläutert.

**Erhöhung der Kapillarkraft durch mehrere flüssige Brücken**

In diesem Kapitel haben wir zunächst die Kraft, die eine einzelne kapillare Brücke zwischen zwei Substraten ausübt, als Funktion des Abstandes zwischen ihnen berechnet. Als Substrate haben wir parallele, steife Platten mit gleichen Materialeigenschaften, d.h. $\theta_1 = \theta_2 = \theta$, angenommen. Die Ergebnisse haben wir in Abb. 2.2 (Symbole) als Diagramm wiedergegeben, in dem die normierte Kapillarkraft $f$ als Funktion des normierten Abstandes $d$ für alle möglichen Kontaktwinkel aufgetragen ist. Das Diagramm zeigt, dass die Kraft

attraktiv (positiv) ist für $\theta \leq 90°$ und abstoßend (negativ) ist für $\theta > 90°$. Darüber hinaus sieht man deutlich, dass auch hydrophobe Oberflächen ($\theta > 90°$) attraktive Wechselwirkungen bei großen Abständen ausüben können. Die Berechnungen zeigen, dass der Betrag von $f$ für kleine $d$ proportional zu $1/d^2$ abnimmt, während er für große $d$ divergiert. Abb 2.2 enthält außerdem einen Vergleich der numerisch berechneten Kurven mit analytisch berechneten Kraft-Abstand Kurven [40] (Linien). Die exzellente Übereinstimmung bestätigt die Genauigkeit unserer numerischen Rechnungen und rechtfertigt die Anwendung dieser Methode auf komplexe Systeme, für die es keine analytische Lösung gibt.

Beim Übergang von einer Brücke zu $n$ Brücken (Abb. 2.3), nehmen wir an, dass das Gesamtvolumen der Flüssigkeit und der Abstand der Platten konstant bleiben. Außerdem soll es keine Wechselwirkung zwischen den Brücken geben, und alle Brücken werden als thermodynamisch stabil angenommen. Letzteres ist auch bei kleinen Volumina der einzelnen Brücken möglich, wenn Materialtransport zwischen ihnen ausgeschlossen werden kann, was z.B. durch eine geeignete Strukturierung der Substratoberflächen möglich ist.

Die Abb. 2.4 und Abb. 2.5 fassen die Ergebnisse für alle möglichen Werte von $\theta$ und $n$ zusammen, wobei als absoluter Abstand $D$ zwischen den Platten $D$=15 µm gewählt wurde, für das Gesamtvolumen $V$ der Flüssigkeit $V$=1 µl gewählt wurde und die Oberflächenspannung zwischen Flüssigkeit und Luft wie folgt angenommen wurde: $\gamma_{lv}$=0.0728 N/m. Wir sehen, dass die Anzahl der mechanisch stabilen Brücken durch $D$ und $V$ limitiert ist und von $\theta$ abhängt, es existiert also ein $n_{max} = n_{max}(D,V,\theta)$. Die Kurven zeigen außerdem, dass für $\theta \leq 52°$ $f(d)$ ein Maximum bei bestimmtem $n < n_{max}$ hat, während für $\theta > 52°$ die Kraft mit $n$ monoton wächst. Die maximale Kraft tritt nicht wie erwartet für sehr hydrophile Oberflächen auf, sondern für $\theta \sim 70°$. Dieses Phänomen lässt sich aus dem Zusammenspiel zwischen der Oberflächenspannung der Kontaktlinie und dem Laplace Druck

der flüssigen Brücke erklären. Die Ergebnisse zeigen außerdem, dass die schwach attraktive Kraft für große $d$ und $\theta > 90°$ durch Aufspaltung in viele kleine Brücken stärker wird. Oberflächen, die a priori hydrophob sind, können also bei genügend großer Anzahl von Brücken eine attraktive Kraft ausüben, die so groß sein kann wie im Fall einer einzigen Brücke zwischen hydrophilen Oberflächen.

Wird die Gesamtkraft durch die gesamte Fläche geteilt, die mindestens notwendig ist, um $n$ individuelle, nichtüberlappende Brücken nebeneinander auf einem Substrat zu platzieren, so erhält man die Spannung als Funktion von $\theta$ und $n$. Abb 2.8 stellt ein derartiges Spannungsdiagramm dar, in dem die Farbskala die Werte der Spannung angibt und $D$, $V$ und $\gamma_{lv}$ wie oben gewählt sind. Man sieht, dass das Maximum der Spannung bei $\theta = 90°$ liegt, da in diesem Fall, d.h. für zylindrische Brücken, die Kraft mit $n$ zunimmt, während die Fläche konstant bleibt. Abb. 2.10 stellt ein Farbdiagramm der Energie dar, die benötigt wird, um die Brücken beginnend bei dem Abstand $D$=15 µm bis zum Zerreißen zu strecken. Sie ist ein Maß für die Stärke der Anziehung der beiden Platten. In diesem Fall tritt das Maximum bei einer Brücke zwischen hydrophilen Platten auf.

Zusammenfassend zeigen die Ergebnisse, dass i) für alle Kontaktwinkel durch die Bildung mehrerer kleiner Brücken eine Erhöhung der Kapillarkraft auftritt im Vergleich zu einer einzigen großen Brücke, dass ii) das absolute Maximum der Kraft bei $\theta \approx 70°$ und $n \approx 9 \cdot 10^5$ (unabhängig von $D$ und $V$) liegt und dass iii) das Maximum der Spannung, also der Kraft bei vorgegebener Kontaktfläche, bei $\theta \approx 90°$ und $n \approx 9 \cdot 10^5$ liegt und dass iv) die Wechselwirkung zwischen hydrophoben Substraten als Funktion von $n$ attraktiv werden kann. Die Farbdiagramme von Kraft, Spannung und Energie der kapillaren Brücken können als übersichtliche Leitlinien dienen, um gewünschte Eigenschaften in künstlichen Haftsystemen einzustellen.

**Asymmetrische Kontaktwinkel**

Während im letzten Kapitel angenommen wurde, dass die Kontaktwinkel an beiden Platten identisch sind, wird in diesem Kapitel diese idealisierte Annahme aufgegeben, und es wird der Einfluss der Kontaktwinkelasymmetrie, d.h. $\theta_1 \neq \theta_2$, auf die Kapillarkraft untersucht. Abgesehen von Berechnungen einiger Spezialfälle [74, 75], gibt es keine systematische Studie zu dieser Frage, da die Oberflächenkontur einer flüssigen Brücke zwischen zwei verschiedenen Substraten nicht durch eine einfache Geometrie angenährt werden kann. Aus diesem Grund kann nur eine numerische Methode angewendet werden, um für beliebige Substratkonfigurationen die Kapillarkraft zu berechnen.

Die numerisch berechneten Kraft-Abstand Kurven für eine flüssige Brücke sind für verschiedene Kombinationen von Kontaktwinkeln in Abb 3.3 dargestellt. Die Ergebnisse zeigen, dass im Fall einer hydrophilen Platte ($\theta_1 = 60°$) die Kraft attraktiv ist bis zu einem Kontaktwinkel $\theta_2 \leq 120°$, d.h. der Bereich attraktiver Wechselwirkungen wächst auf Kosten des Bereiches repulsiver Wechselwirkungen. Das Umgekehrte geschieht wenn eine Platte hydrophob ist ($\theta_1 = 120°$), dann erstrecken sich die repulsiven Wechselwirkungen bis zu Kontaktwinkeln $\theta_2 \geq 90°$ (ausgenommen hiervon sind die Kräfte bei sehr großem $d$). Diese Effekte werden verstärkt, wenn eine Platte entweder super hydrophil (30°) bzw. super hydrophob (150°) ist.

Abb 3.7 zeigt die größtmöglichen Abstände zwischen den Platten als Funktion der Kontaktwinkel. Aus den Kurven folgt, dass für alle möglichen Kontaktwinkel dieser maximale Abstand bis zum Zerreißen der Brücke immer für den symmetrischen Fall $\theta_1 = \theta_2$ auftritt. In Abb 3.5 sind Kraft-Abstand Kurven für einen festen normierten Abstand $d = 0.05$ aufgetragen. Die Symbole geben die berechneten Kurven wieder, während die Linien Fitfunktionen der Gestalt $f(d,\theta_1,\theta_2)=g(d)\cdot(\cos\theta_1+\cos\theta_2)$ sind. Mit diesem Fit reproduzieren wir ein früheres Resultat [75], das für eine Kugel in Kontakt mit einer Platte entwickelte wurde.

Die gute Übereinstimmung in unserem Fall zeigt, dass diese Fitformel auch auf die Konfiguration Platte-Platte anwendbar ist, die sich aus obiger Konfiguration für einen sehr großen Kugelradius ergibt.

Zusammengefasst zeigen die Berechnungen dieses Kapitels, dass bei asymmetrischen Konfigurationen der Kontaktwinkel ein stark hydrophiles bzw. hydrophobes Substrat den attraktiven bzw. repulsiven Wechselwirkungsbereich vergrößert. Somit ist der Grad der Kontaktwinkelasymmetrie ein weiterer Parameter zur Steuerung der Kapillarkraft. Symmetrische Brücken sind mechanisch stabiler als alle asymmetrischen Brücken. Die Resultate dieses Kapitels sind besonderes wichtig bei der Interpretation experimenteller Beobachtungen, in denen praktisch immer unterschiedliche Kontaktwinkel auftreten. Aus diesem Grund beinhaltet diese Arbeit ein Kapitel über Messungen von Kontaktwinkeln und Kapillarkräften.

**Experimentelle Bestimmung der kapillaren Kraft**

Um die Berechnungen des letzten Kapitels experimentell zu überprüfen, wurden Kraft-Abstand Kurven für verschiedene plattenförmige Substrate gemessen. Diese Experimente wurden im Rahmen einer Kollaboration mit Prof. A. Crosby von der University of Massachusetts in Amherst, USA, durchgeführt. Der experimentelle Aufbau ist in Abb. 4.2 dargestellt. Mit Hilfe eines Piezo – Motors wird Substrat 2, auf dem ein Wasser Tropfen platziert ist, mit einer Geschwindigkeit von ca. 10 μm/s in die Richtung des Substrates 1 bewegt, das an einem Aluminium Kantilever befestigt ist. Eine flüssige Brücke bildet sich wenn das Wasser Substrat 1 berührt, wodurch der Kantilever bewegt wird. Aufgenommen wird der Abstandsunterschied, der bei dieser Bewegung entsteht und aus dem sowohl der Abstand als auch die Kraft zwischen den Substraten errechnet werden können. Als Substrate dienten wieder zwei parallel ausgerichtete Platten mit unterschiedlichen

Materialeigenschaften.

In Abb. 4.4 präsentieren wir sowohl die experimentell gemessenen Kurven [172] als auch die numerisch berechneten (schwarz und blau). Während der Motor das Substrat 2 in die Richtung des Substrates 1 führt, wird die Brücke zwischen den Platten gestaucht und der Gleichgewichtswert der dynamischen Kontaktwinkel ist der sog. fortschreitende (advancing) Kontaktwinkel. Die gemessene Kraft entspricht in diesem Fall dem Ast der roten Kurve, der mit „advancing branch“ bezeichnet ist. Bei Richtungswechsel ändert sich auch der Kontaktwinkel an den Platten und es stellt sich der sog. Rückzugswinkel (receding angle) ein, und die gemessene Kraft entspricht dem Ast, der mit „receding branch“ bezeichnet ist. Die Ergebnisse zeigen, dass die beiden Äste der gemessenen Kurve durch die numerisch berechneten Kurven sehr gut angenähert werden, wenn im numerischen Model die angegeben dynamischen Winkel an den beiden Platten vorausgesetzt werden. Man benötigt demnach 4 Winkel: 2 fortschreitende und 2 Rückzugswinkel an beiden Platten, um eine allgemeine Platte-Platte Konfiguration zu beschreiben.

Die gute Übereinstimmung zwischen gemessenen und berechneten Kurven zeigt, dass das numerische Model auch im Falle unterschiedlicher Kontaktwinkel realistische Resultate liefert und ist somit eine weitere Bestätigung für die Zuverlässigkeit dieser Methode. Darüber hinaus zeigt der Vergleich der Kurven, dass Messungen der Kapillarkraft verwendet werden können, um die Kontakwinkelhysteresis (Unterschied zwischen advancing und receding angle) zu bestimmen. Bis jetzt ist dies oft über direkte Messungen der Winkel versucht worden, was allerdings besonders bei sehr hydrophoben Substraten sehr schwierig sein kann. Unsere Methode ist dagegen einfach durchzuführen und zuverlässig.

**Geometrie der Substrate**

In diesem Kapitel wird ein Substrat als kugelförmig angenommen und diese Kugel-Platte Konfiguration mit der in den letzten Kapiteln untersuchten Platte-Platte Konfiguration verglichen. Der Übergang zu einem kugelförmigen Substrat führt zu einem zusätzlich Parameter bei der Berechnung der Kapillarkraft, nämlich der Größe der Kugel im Vergleich zur Größe der flüssigen Brücke. Dieses Verhältnis wird durch $R/s$ ausgedrückt, wobei $R$ der Radius der Kugel ist und $s$ der Radius einer fiktiven Kugel, deren Volumen dem flüssigen Gesamtvolumen $V$ entspricht.

Der Einfluss des Verhältnisses $R/s$ auf die Kraft-Abstand Kurve hängt von dem Abstand ab. Für $d \rightarrow 0$, zum Beispiel, konvergiert die Kraft für alle Winkel und auch für großen Kugelradius gegen einen endlichen Wert (Abb. 5.3), so wie es erwartet wird, da der Radius der Kugel die Benetzungsfläche begrenzt und folglich auch die Kraft. Somit spielt der Radius der Kugel eine wichtige Rolle bei kleinem Abstand. Eine interessanter Unterschied zur Situation einer Platte-Platte Geometrie, ist die abstoßende Kraft für $\theta \leq 90°$, die bei sehr kleinen Abständen auftritt und mit kleiner werdenden Radius deutlicher wird (Abb. 5.3b, 5.6b).

Darüber hinaus haben wir bei festem Abstand die Kraft als Funktion des Kugelradius für alle Winkel ausgedrückt (Abb. 5.4). Somit haben wir nicht nur frühe Ergebnisse [47, 75] für eine Kugel in Kontakt mit einem Substrat reproduziert, sondern auch ein auf alle Abstände erweitertes Model präsentiert. Exponentielle Fitfunktionen nähern die berechneten Kraft-Radius Kurven sehr gut an.

Zum ersten Mal wurden die verschiedenen Beiträge zur Gesamtkraft, die aus dem Laplacen Druck und der Oberflächenspannung der Kontaktlinien resultieren, getrennt für alle Abstände, Kontaktwinkel und für unterschiedlichen Geometrien dargestellt (Abb. 5.5). Diese Farbdiagramme vermitteln nicht nur einen Überblick über das verschiedenen Verhalten aller Kräfte, sondern sie sind auch besonders wichtig für das Verständnis bestimmter Resultate,

wie z.B. die die Erhöhung der Kapillarkraft durch mehrere flüssige Brücken.

Die Ergebnisse einer solchen Kontaktaufspaltung für die Kugel-Platte Geometrie (Abb. 5.8) zeigen, dass eine Erhöhung der Kraft eintritt, diese jedoch reduziert ist im Vergleich zur Geometrie zweier Platten. Auch ist das Maximum der Kraft zu kleineren Winkeln, $\theta \sim 50°$ verschoben.

Zusammengefasst haben wir in diesem Kapitel gezeigt, dass im Falle einer Kugel in Kontakt mit einer Platte nicht nur die Geometrie dieser Konfiguration, sondern auch die Größe der Kugel im Vergleich zur Größe der flüssigen Brücke wichtige Parameter darstellen, die zu Ergebnisse führen, die qualitativ und quantitativ von denen einer Platte-Platte Konfiguration abweichen.

Eine Verstärkung der Kapillarkraft für mehrere kleine Brücken tritt auch in diesem Fall auf, ist aber schwächer ausgeprägt als im Falle zweier Platten.

# References


1. Spolenak, R.; Gorb, S.; Arzt, E., Adhesion design maps for bio-inspired attachment systems. *Acta Biomaterialia* **2005,** 1, (1), 5-13.
2. Spolenak, R.; Gorb, S.; Gao, H. J.; Arzt, E., Effects of contact shape on the scaling of biological attachments. *Proceedings of the Royal Society of London Series a-Mathematical Physical and Engineering Sciences* **2005,** 461, (2054), 305-319.
3. Hanna, G.; Barnes, W. J. P., Adhesion and Detachment of the Toe Pads of Tree Frogs. *Journal of Experimental Biology* **1991,** 155, 103-125.
4. Barnes, W. J. P., Bionics and Wet Grip. *Tire Technology International* **2002**, 56-60.
5. Barnes, W. J. P.; Oines, C.; Smith, J. M., Whole animal measurements of shear and adhesive forces in adult tree frogs: insights into underlying mechanisms of adhesion obtained from studying the effects of size and scale. *Journal of Comparative Physiology a-Neuroethology Sensory Neural and Behavioral Physiology* **2006,** 192, (11), 1179-1191.
6. Walker, G.; Yule, A. B.; Ratcliffe, J., The Adhesive Organ of the Blowfly, Calliphora-Vomitoria - a Functional-Approach (Diptera, Calliphoridae). *Journal of Zoology* **1985,** 205, (Feb), 297-307.
7. Gorb, S. N., The design of the fly adhesive pad: Distal tenent setae are adapted to the delivery of an adhesive secretion. *Proceedings of the Royal Society of London Series B-Biological Sciences* **1998,** 265, (1398), 747-752.
8. Gorb, S., Attachment Devices of Insect Cuticle. In Kluwer Academic Publishers: Dordrecht, The Netherlands, 2001; p 186.
9. Ruibal, R.; Ernst, V., Structure of Digital Setae of Lizards. *Journal of Morphology* **1965,** 117, (3), 271-&.
10. Autumn, K.; Sitti, M.; Liang, Y. C. A.; Peattie, A. M.; Hansen, W. R.; Sponberg, S.; Kenny, T. W.; Fearing, R.; Israelachvili, J. N.; Full, R. J., Evidence for van der Waals adhesion in gecko setae. *Proceedings of the National Academy of Sciences of the United States of America* **2002,** 99, (19), 12252-12256.
11. Huber, G.; Mantz, H.; Spolenak, R.; Mecke, K.; Jacobs, K.; Gorb, S. N.; Arzt, E., Evidence for capillarity contributions to gecko adhesion from single spatula nanomechanical measurements. *Proceedings of the National Academy of Sciences of the United States of America* **2005,** 102, (45), 16293-16296.
12. Israelachvili, J. N., Intermolecular and Surface Forces. In Academic Press: London, 1992; pp 312-337.
13. Taylor, B., Concerning the Ascent of Water between two Glass planes. *Phil. Trans. Roy. Soc. London* **1712,** 27, 538.
14. Segner, J. A., De figuris superficierum fluidarum. *Commentarii Societ. Regiae Scientiarium Gottingensis* **1751,** 1, 301-372.
15. Laplace, P. S., Sur L' Action Capillaire. In *Dixieme Livre du Traite de Mecanique Celeste*, Couveier: Paris, 1805-1806; pp 1-65.
16. Young, T., An Essay on the Cohesion of Fluids. *Phil. Trans. Roy. Soc.* **1805,** 95, 65-87.
17. Gauss, C. F., Allgemeine Grundlagen einer Theorie der Gestalt von Fluessigkeiten im Zustand des Gleichgewichtes. *Commentationes Societatis Regiae Scientiarium Gottingensis Recentiores* **1830,** 7, 1-73.
18. Delaunay, C. E., Sur la surface de revolution dont la courbure moyenne est constante. *J. Math. Pures Appl.* **1841,** 6, 309-315.
19. Plateau, J. A. F., Statique experimentale et theorique des liquids. *Mem. de l' Acad. de Belgique* **1843,** 16.
20. Plateau, J. A. F., Statique des Liquides. *Gauthier-Villars* **1873**, 338-369.

21. Concus, P.; Finn, R., Singular Solution of Capillary Equation .1. Existence. *Inventiones Mathematicae* **1975,** 29, (2), 143-148.
22. Concus, P.; Finn, R., Singular Solution of Capillary Equation .2. Uniqueness. *Inventiones Mathematicae* **1975,** 29, (2), 149-159.
23. Finn, R., Equilibrium Capillary Surfaces. In *Grundlehren der mathematischen Wissenschaften*, Springer: New York, Berlin, Heidelberg, Tokyo, 1986; p 82.
24. Finn, R.; Vogel, T. I., On the Volume Infimum for Liquid Bridges. *Zeitschrift für Analysis und ihre Anwendungen* **1992,** 11, 3-23.
25. Vogel, T. I., Stability of a Liquid Drop Trapped between two Parallel Planes *SIAM Journal on Applied Mathematics* **1987,** 47, (3), 516-525.
26. Vogel, T. I., Types of Instability for the Trapped Drop Problem with Equal Contac Angles. In *Geometric Analysis and Computer Graphics*, Concus, P.; Finn, R.; Hoffman, D. A., Eds. Springer: New York, Berlin, 1988; pp 195-203.
27. Vogel, T. I., Stability of a Liquid Drop Trapped between two Parallel Planes II: General Contact Angles. *SIAM Journal on Applied Mathematics* **1989,** 49, (4), 1009-1028.
28. Langbein, D., Stability of Liquid Bridges between Parallel Plates. *Proceedings VIII th European Symposium on Materials and Fluid Sciences in Microgravity* **1992,** ESA SP-333, 85-93.
29. Langbein, D., Stability of Liquid Bridges between Parallel Plates. *Microgravity Science Technology* **1992,** 1, (5), 2-11.
30. Langbein, D., Capillary Surfaces. In Springer: Berlin, Heidelberg, 2002; pp 61-64.
31. Lowry, B. J., Pressure and stress measurement via image analysis (P-SIA) of axisymmetric drops and liquid bridges. *Journal of Colloid and Interface Science* **1996,** 178, (1), 284-297.
32. Lowry, B. J., Modes of nonaxisymmetry in the stability of fixed contact line liquid bridges and drops. *Journal of Colloid and Interface Science* **2000,** 224, (1), 28-46.
33. Lowry, B. J.; Steen, P. H., Capillary Surfaces - Stability from Families of Equilibria with Application to the Liquid Bridge. *Proceedings of the Royal Society of London Series a-Mathematical and Physical Sciences* **1995,** 449, (1937), 411-439.
34. Coriell, S. R.; Hardy, S. C.; Cordes, M. R., Stability of Liquid Zones. *Journal of Colloid and Interface Science* **1977,** 60, (1), 126-136.
35. Erle, M. A.; Dyson, D. C.; Morrow, N. R., Liquid Bridges between Cylinders, in a Torus, and between Spheres. *Aiche Journal* **1971,** 17, (1), 115-&.
36. Gillette, R. D.; Dyson, D. C., Stability of Fluid Interfaces of Revolution between Equal Solid Circular Plates. *Chemical Engineering Journal* **1971,** 2, 44-54.
37. Michael, D. H., Meniscus Stability. *Annual Review of Fluid Mechanics* **1981,** 13, 189-215.
38. Slobozhanin, L. A.; Alexander, J. I. D.; Patel, V. D., The stability margin for stable weightless liquid bridges. *Physics of Fluids* **2002,** 14, (1), 209-224.
39. Fortes, M. A., Axisymmetric Liquid Bridges between Parallel Plates. *Journal of Colloid and Interface Science* **1982,** 88, (2), 338-352.
40. Carter, W. C., The Forces and Behavior of Fluids Constrained by Solids. *Acta Metallurgica* **1988,** 36, (8), 2283-2292.
41. Zhou, L. M., On the Volume Infimum for Liquid Bridges. *Zeitschrift für Analysis und ihre Anwendungen* **1993,** 12, 629-642.
42. Zhou, L. M., On stability of a catenoidal liquid bridge. *Pacific Journal of Mathematics* **1997,** 178, (1), 185-198.
43. Derjaguin, B., Analysis of friction and adhesion IV The theory of the adhesion of small particles. *Kolloid-Zeitschrift* **1934,** 69, (2), 155-164.
44. Derjaguin.B, Concerning Paper - Effect of Capillary Liquid on Force of Adhesion between Spherical Solid Particles. *Journal of Colloid and Interface Science* **1968,** 26, (2),

253-&.
45. Derjaguin, B. V., Direct Measurement of Molecular Attraction between Solids Separated by a Narrow Gap. *Quarterly Reviews* **1956,** 10, (3), 295-&.
46. Willett, C. D.; Adams, M. J.; Johnson, S. A.; Seville, J. P. K., Capillary bridges between two spherical bodies. *Langmuir* **2000,** 16, (24), 9396-9405.
47. McFarlane, J. S.; Tabor, D., Adhesion of Solids and the Effect of Surface Films. *Proceedings of the Royal Society of London Series a-Mathematical and Physical Sciences* **1950,** 202, (1069), 224-243.
48. Fisher, L. R.; Israelachvili, J. N., Direct Measurement of the Effect of Meniscus Forces on Adhesion - Study of the Applicability of Macroscopic Thermodynamics to Microscopic Liquid Interfaces. *Colloids and Surfaces* **1981,** 3, (4), 303-319.
49. Fisher, L. R.; Israelachvili, J. N., Experimental Studies on the Applicability of the Kelvin Equation to Highly Curved Concave Menisci. *Journal of Colloid and Interface Science* **1981,** 80, (2), 528-541.
50. Christenson, H. K., Adhesion between Surfaces in Undersaturated Vapors - A Reexamination of the influence of Meniscus Curvature and Surface Forces. *Journal of Colloid and Interface Science* **1988,** 121, (1), 170-178.
51. Maeda, N.; Israelachvili, J. N., Nanoscale mechanisms of evaporation, condensation and nucleation in confined geometries. *Journal of Physical Chemistry B* **2002,** 106, (14), 3534-3537.
52. Maeda, N.; Israelachvili, J. N.; Kohonen, M. M., Evaporation and instabilities of microscopic capillary bridges. *Proceedings of the National Academy of Sciences of the United States of America* **2003,** 100, (3), 803-808.
53. Rabinovich, Y. I.; Movchan, T. G.; Churaev, N. V.; Ten, P. G., Phase-Separation of Binary-Mixtures of Polar Liquids Close to Solid-Surfaces. *Langmuir* **1991,** 7, (4), 817-820.
54. Wanless, E. J.; Christenson, H. K., Interaction between Surfaces in Ethanol - Adsorption, Capillary Condensation, and Solvation Forces. *Journal of Chemical Physics* **1994,** 101, (5), 4260-4267.
55. Curry, J. E.; Christenson, H. K., Adsorption, wetting, and capillary condensation of nonpolar fluids in mica slits. *Langmuir* **1996,** 12, (23), 5729-5735.
56. Kohonen, M. M.; Maeda, N.; Christenson, H. K., Kinetics of capillary condensation in a nanoscale pore. *Physical Review Letters* **1999,** 82, (23), 4667-4670.
57. Kohonen, M. M.; Christenson, H. K., Capillary condensation of water between rinsed mica surfaces. *Langmuir* **2000,** 16, (18), 7285-7288.
58. Qiao, Y.; Christenson, H. K., Direct observation of capillary condensation of a solid. *Physical Review Letters* **2001,** 86, (17), 3807-3810.
59. Kohonen, M. M.; Christenson, H. K., Capillary condensation from vapors of n-hexane/perfluoro-n-hexane mixtures. *Journal of Physical Chemistry B* **2002,** 106, (26), 6685-6695.
60. Tian, X. F.; Bhushan, B., The micro-meniscus effect of a thin liquid film on the static friction of rough surface contact. *Journal of Physics D-Applied Physics* **1996,** 29, (1), 163-178.
61. Chilamakuri, S. K.; Bhushan, B., A comprehensive kinetic meniscus model for prediction of long-term static friction. *Journal of Applied Physics* **1999,** 86, (8), 4649-4656.
62. Stifter, T.; Marti, O.; Bhushan, B., Theoretical investigation of the distance dependence of capillary and van der Waals forces in scanning force microscopy. *Physical Review B* **2000,** 62, (20), 13667-13673.
63. Bhushan, B., Adhesion and stiction: Mechanisms, measurement techniques, and methods for reduction. *Journal of Vacuum Science & Technology B* **2003,** 21, (6), 2262-2296.
64. Feiler, A. A.; Stiernstedt, J.; Theander, K.; Jenkins, P.; Rutland, M. W., Effect of capillary condensation on friction force and adhesion. *Langmuir* **2007,** 23, (2), 517-522.

65. Bhushan, B., The Effect of Liquid Capillaries on Adhesion. In *Handbook of Nanotechnology*, 2 ed.; Springer: Heidelberg, 2007; pp 959-964.
66. Malotky, D. L.; Chaudhury, M. K., Investigation of capillary forces using atomic force microscopy. *Langmuir* **2001,** 17, (25), 7823-7829.
67. Jang, J. K.; Schatz, G. C.; Ratner, M. A., Capillary force in atomic force microscopy. *Journal of Chemical Physics* **2004,** 120, (3), 1157-1160.
68. Farshchi-Tabrizi, M.; Kappl, M.; Cheng, Y. J.; Gutmann, J.; Butt, H. J., On the adhesion between fine particles and nanocontacts: An atomic force microscope study. *Langmuir* **2006,** 22, (5), 2171-2184.
69. Zitzler, L.; Herminghaus, S.; Mugele, F., Capillary forces in tapping mode atomic force microscopy. *Physical Review B* **2002,** 66, (15), -.
70. Melrose, J. C., Model Calculations for Capillary Condensation. *Aiche Journal* **1966,** 12, (5), 986-&.
71. Lian, G. P.; Thornton, C.; Adams, M. J., A Theoretical-Study of the Liquid Bridge Forces between 2 Rigid Spherical Bodies. *Journal of Colloid and Interface Science* **1993,** 161, (1), 138-147.
72. Clark, W. C.; Haynes, J. M.; Mason, G., Liquid Bridges between a Sphere and a Plane. *Chemical Engineering Science* **1968,** 23, (7), 810-&.
73. Hotta, K.; Takeda, K.; Iinoya, K., The Capillary Binding Force of a Liquid Bridge. *Powder Technology* **1974,** 10, (4-5), 231-242.
74. Orr, F. M.; Scriven, L. E.; Rivas, A. P., Pendular Rings between Solids - Meniscus Properties and Capillary Force. *Journal of Fluid Mechanics* **1975,** 67, (Feb25), 723-742.
75. O' Brien, W. J.; Hermann, J. J., Strength of Liquid Bridges between Dissimilar Materials. *Journal of Adhesion* **1973,** 5, (2), 91-103.
76. Binggeli, M.; Mate, C. M., Influence of Capillary Condensation of Water on Nanotribology Studied by Force Microscopy. *Applied Physics Letters* **1994,** 65, (4), 415-417.
77. Bhushan, B.; Dandavate, C., Thin-film friction and adhesion studies using atomic force microscopy. *Journal of Applied Physics* **2000,** 87, (3), 1201-1210.
78. Fuji, M.; Machida, K.; Takei, T.; Watanabe, T.; Chikazawa, M., Effect of wettability on adhesion force between silica particles evaluated by atomic force microscopy measurement as a function of relative humidity. *Langmuir* **1999,** 15, (13), 4584-4589.
79. Ouyang, Q.; Ishida, K.; Okada, K., Investigation of micro-adhesion by atomic force microscopy. *Applied Surface Science* **2001,** 169, 644-648.
80. Sedin, D. L.; Rowlen, K. L., Adhesion forces measured by atomic force microscopy in humid air. *Analytical Chemistry* **2000,** 72, (10), 2183-2189.
81. Gulbinski, W.; Pailharey, D.; Suszko, T.; Mathey, Y., Study of the influence of adsorbed water on AFM friction measurements on molybdenum trioxide thin films. *Surface Science* **2001,** 475, (1-3), 149-158.
82. Biggs, S.; Cain, R. G.; Dagastine, R. R.; Page, N. W., Direct measurements of the adhesion between a glass particle and a glass surface in a humid atmosphere. *Journal of Adhesion Science and Technology* **2002,** 16, (7), 869-885.
83. Jones, R.; Pollock, H. M.; Geldart, D.; Verlinden, A., Inter-particle forces in cohesive powders studied by AFM: effects of relative humidity, particle size and wall adhesion. *Powder Technology* **2003,** 132, (2-3), 196-210.
84. Marmur, A., Tip Surface Capillary Interactions. *Langmuir* **1993,** 9, (7), 1922-1926.
85. de Lazzer, A.; Dreyer, M.; Rath, H. J., Particle-surface capillary forces. *Langmuir* **1999,** 15, (13), 4551-4559.
86. Xiao, X. D.; Qian, L. M., Investigation of humidity-dependent capillary force. *Langmuir* **2000,** 16, (21), 8153-8158.
87. Sirghi, L.; Nakagiri, N.; Sugisaki, K.; Sugimura, H.; Takai, O., Effect of sample topography on adhesive force in atomic force spectroscopy measurements in air. *Langmuir*

**2000,** 16, (20), 7796-7800.
88. Yoon, E. S.; Yang, S. H.; Han, H. G.; Kong, H., An experimental study on the adhesion at a nano-contact. *Wear* **2003,** 254, (10), 974-980.
89. Gao, C., Theory of menisci and its applications. *Applied Physics Letters* **1997,** 71, (13), 1801-1803.
90. Bocquet, L.; Charlaix, E.; Ciliberto, S.; Crassous, J., Moisture-induced ageing in granular media and the kinetics of capillary condensation. *Nature* **1998,** 396, (6713), 735-737.
91. Ando, Y., The effect of relative humidity on friction and pull-off forces measured on submicron-size asperity arrays. *Wear* **2000,** 238, (1), 12-19.
92. He, M. Y.; Blum, A. S.; Aston, D. E.; Buenviaje, C.; Overney, R. M.; Luginbuhl, R., Critical phenomena of water bridges in nanoasperity contacts. *Journal of Chemical Physics* **2001,** 114, (3), 1355-1360.
93. Ata, A.; Rabinovich, Y. I.; Singh, R. K., Role of surface roughness in capillary adhesion. *Journal of Adhesion Science and Technology* **2002,** 16, (4), 337-346.
94. Rabinovich, Y. I.; Adler, J. J.; Esayanur, M. S.; Ata, A.; Singh, R. K.; Moudgil, B. M., Capillary forces between surfaces with nanoscale roughness. *Advances in Colloid and Interface Science* **2002,** 96, (1-3), 213-230.
95. Rabinovich, Y. I.; Esayanur, M. S.; Johanson, K. D.; Adler, J. J.; Moudgil, B. M., Measurement of oil-mediated particle adhesion to a silica substrate by atomic force microscopy. *Journal of Adhesion Science and Technology* **2002,** 16, (7), 887-903.
96. Riedo, E.; Levy, F.; Brune, H., Kinetics of capillary condensation in nanoscopic sliding friction. *Physical Review Letters* **2002,** 88, (18), -.
97. Riedo, E.; Pallaci, I.; Boragno, C.; Brune, H., The 2/3 power law dependence of capillary force on normal load in nanoscopic friction. *Journal of Physical Chemistry B* **2004,** 108, (17), 5324-5328.
98. Stone, W., Some phenomena of the contact of solids. *Philosophical Magazine* **1930,** 9, (58), 610-620.
99. Thomson, W., On the Equilibrium of Vapour at a Curved Surface of Liquid. *Proc. Roy. Soc. Edinburgh* **1870,** 7, (63), 448-452.
100. Christenson, H. K., Capillary condensation due to van der Waals attraction in wet slits. *Phys. Rev. Let* **1994,** 73, 1821-1824.
101. Christenson, H. K., Capillary Condensation Due to Van-Der-Waals Attraction in Wet Slits. *Physical Review Letters* **1994,** 73, (13), 1821-1824.
102. Arzt, E.; Gorb, S.; Spolenak, R., From micro to nano contacts in biological attachment devices. *Proceedings of the National Academy of Sciences of the United States of America* **2003,** 100, (19), 10603-10606.
103. Greiner, C.; del Campo, A.; Arzt, E., Adhesion of bioinspired micropatterned surfaces: Effects of pillar radius, aspect ratio, and preload. *Langmuir* **2007,** 23, (7), 3495-3502.
104. Adamson, A. W.; Gast, A. P., Physical Chemistry of Surfaces. In 6 ed.; Wiley-VHC: Weinheim, Germany, 1997; pp 4-49.
105. De Gennes, P. G.; Brochard-Wyart, F.; Quéré, D., Capillarity and Wetting Phenomena. In Springer: New York, 2004; p 30.
106. Neumann, F., Vorlesung über die Theorie der Kapillarität. In Wangerin, A., Ed. B.G.Teubner: Leipzig, 1894; pp 113-116.
107. Aveyard, R.; Clint, J. H.; Paunov, V. N.; Ness, D., Capillary Condensation of Vapours between two Solid Surfaces: Effects of Line Tension and Surface Forces. *Phys. Chem. Chem. Phys* **1998,** 1, 155-163.
108. Brakke, K., The Surface Evolver. **1999,** Version 2.14.
109. Poisson, S. D., Auszug aus Poisson's Nouvelle Theorie de L'Action Capillaire. *Annalen der Physik und Chemie* **1833,** 27, 193-234.
110. Maxwell, J. C., The Scientific Papers of James Clerk Maxwell. In Cambridge

University Press: Cambridge UK, 1890; Vol. 2, pp 541-591.
111. Gibbs, J. W., The Scientific Papers of J. Williard Gibbs. In Longmans, Gree and Company: New York, 1906; Vol. 1, p 55.
112. Ono, S.; Kondo, S., Encyclopedia of Physics (ed. S. Flugge). In Springer: Berlin, 1960; Vol. 10, p 134.
113. Evans, R., Nature of the Liquid-Vapor Interface and Other Topics in the Statistical-Mechanics of Nonuniform, Classical Fluids. *Advances in Physics* **1979,** 28, (2), 143-200.
114. Rowlinson, J. S.; Widom, B., Molecular Theory of Capillarity. In 4 ed.; Dover Publications: Mineola, NY, 2002.
115. Zisman, W. A., Relation of the Equilibrium Contact Angle to Liquid and Solid Constitution. In *The Advances in Chemistry Series: Contact Angle Wettability and Adhesion*, Gould, R. F., Ed. Amer. Chem. Soc.: Washington, D. C., 1964; Vol. 43, pp 1-51.
116. Boucher, E. A., Wettability and Adhesion of Polyethylene. *Nature* **1967,** 215, (5105), 1054-1071.
117. De Gennes, P. G., Wetting - Statics and Dynamics. *Reviews of Modern Physics* **1985,** 57, (3), 827-863.
118. Ishii, S., Adhesion of a Leaf Feeding Ladybird Epilachna-Vigintioctomaculta (Coleoptera, Coccinellidae) on a Vertically Smooth Surface. *Applied Entomology and Zoology* **1987,** 22, (2), 222-228.
119. Edwards, J. S.; Tarkanian, M., Adhesive Pads of Heteroptera - a Re-Examination. *Proceedings of the Royal Entomological Society of London Series a-General Entomology* **1970,** 45, 1-5.
120. Eisner, T.; Aneshansley, D. J., Defense by foot adhesion in a beetle (Hemisphaerota cyanea). *Proceedings of the National Academy of Sciences of the United States of America* **2000,** 97, (12), 6568-6573.
121. Federle, W.; Riehle, M.; Curtis, A. S. G.; Full, R. J., An integrative study of insect adhesion: Mechanics and wet adhesion of pretarsal pads in ants. *Integrative and Comparative Biology* **2002,** 42, (6), 1100-1106.
122. Zayas, F.; Alexander, J. I. D.; Meseguer, J.; Ramus, J. F., On the stability limits of long nonaxisymmetric cylindrical liquid bridges. *Physics of Fluids* **2000,** 12, (5), 979-985.
123. Hilden, J. L.; Trumble, K. P., Numerical analysis of capillarity in packed spheres: Planar hexagonal-packed spheres. *Journal of Colloid and Interface Science* **2003,** 267, (2), 463-474.
124. Dorrer, C.; Ruhe, J., Contact Line Shape on Ultrahydrophobic Post Surfaces *Langmuir* **2007,** 23, (6), 3179-3183.
125. Cross, N. L.; Picknett, R. G., Particle Adhesion in the presence of a liquid film In *The Mechanism of Corrosion by Fuel Impurities*, Johnson. H.R., Littler. D.H.: London. Butterworths, 1963; pp 383-390.
126. Haines, W. B., Studies in the physical properties of soils II. A note on the cohesion developed by capillary forces in an ideal soil. *Journal of Agricultural Science* **1925,** 15, 529-535.
127. Fischer, R. A., On the capillary forces in an ideal soil: correction of formulae given by W.B. Haines. *Journal of Agricultural Science* **1926,** 16, 492-505.
128. Mason, G.; Clark, W. C., Liquid Bridges between Spheres. *Chemical Engineering Science* **1965,** 20, (10), 859-&.
129. Cross, N. L.; Picknett, R. G., The Liquid Layer between a Sphere and a Plane Surface. *Transactions of the Faraday Society* **1963,** 59, (484), 846-855.
130. Gui, J.; Marchon, B., A Stiction Model for a Head-Disk Interface of a Rigid Disk-Drive. *Journal of Applied Physics* **1995,** 78, (6), 4206-4217.
131. Baret, J. C.; Brinkmann, M., Wettability control of droplet deposition and detachment. *Physical Review Letters* **2006,** 96, (14), 1461061-1461064.

132. Rayleigh, L., On the Capillary Phenomena of Jets. *Proceedings of the Royal Society of London A* **1879,** 29, 71-97.
133. Beutel, R. G.; Gorb, S. N., Ultrastructure of attachment specializations of hexapods, (Arthropoda): evolutionary patterns inferred from a revised ordinal phylogeny. *Journal of Zoological Systematics and Evolutionary Research* **2001,** 39, (4), 177-207.
134. Kesel, A. B.; Martin, A.; Seidl, T., Adhesion measurements on the attachment devices of the jumping spider Evarcha arcuata. *Journal of Experimental Biology* **2003,** 206, (16), 2733-2738.
135. Autumn, K.; Peattie, A. M., Mechanisms of adhesion in geckos. *Integrative and Comparative Biology* **2002,** 42, (6), 1081-1090.
136. Persson, B. N. J.; Gorb, S., The effect of surface roughness on the adhesion of elastic plates with application to biological systems. *Journal of Chemical Physics* **2003,** 119, (21), 11437-11444.
137. Irschick, D. J.; Austin, C. C.; Petren, K.; Fisher, R. N.; Losos, J. B.; Ellers, O., A comparative analysis of clinging ability among pad-bearing lizards. *Biological Journal of the Linnean Society* **1996,** 59, (1), 21-35.
138. Autumn, K.; Hansen, W., Ultrahydrophobicity indicates a non-adhesive default state in gecko setae. *Journal of Comparative Physiology a-Neuroethology Sensory Neural and Behavioral Physiology* **2006,** 192, (11), 1205-1212.
139. Drechsler, P.; Federle, W., Biomechanics of smooth adhesive pads in insects: influence of tarsal secretion on attachment performance. *Journal of Comparative Physiology a-Neuroethology Sensory Neural and Behavioral Physiology* **2006,** 192, (11), 1213-1222.
140. Israelachvili, J. N.; Tabor, D., Measurement of van der Waals Dispersion Forces in Range 1.5 to 130 nm. *Proceedings of the Royal Society of London Series a-Mathematical and Physical Sciences* **1972,** 331, (1584), 19-38.
141. Hough, D. B.; White, L. R., The Calculation of Hamaker Constants from Lifshitz Theory with Applications to Wetting Phenomena. *Advances in Colloid and Interface Science* **1980,** 14, (1), 3-41.
142. Tabor, D., Surface Forces and Surface Interactions. *Journal of Colloid and Interface Science* **1977,** 58, (1), 2-13.
143. Owens, D. K.; Wendt, R. C., Estimation of Surface Free Energy of Polymers. *Journal of Applied Polymer Science* **1969,** 13, (8), 1741-&.
144. Koplik, J.; Banavar, J. R.; Willemsen, J. F., Molecular-Dynamics of Poiseuille Flow and Moving Contact Lines. *Physical Review Letters* **1988,** 60, (13), 1282-1285.
145. Rynhart, P. R.; McLachlan, R.; Jones, J. R.; McKibbin, R., Solution of the Young-Laplace Equation for three Particles. *Res. Lett. Inf. Math. Sci.* **2003,** 5, 119-127.
146. Gao, L. C.; McCarthy, T. J., Contact angle hysteresis explained. *Langmuir* **2006,** 22, (14), 6234-6237.
147. Lambert, P.; Delchambre, A., Parameters ruling capillary forces at the submillimetric scale. *Langmuir* **2005,** 21, (21), 9537-9543.
148. Crosby, A. J.; Hageman, M.; Duncan, A., Controlling polymer adhesion with "pancakes". *Langmuir* **2005,** 21, (25), 11738-11743.
149. Greiner, C.; Del Campo, A.; Arzt, E., Adhesion of Bioinspired Micropatterned Surfaces: Effects of Pillar Radius, Aspect Ratio, and Preload. *Langmuir* **2007,** 23, 3495-3502.
150. De Souza, E. J.; Mohrdieck, C.; Brinkmann, M.; Arzt, E., Enhancement of capillary forces by multiple liquid bridges. *Submitted for publication* **2007**.
151. Chen, W.; Fadeev, A. Y.; Hsieh, M. C.; Oner, D.; Youngblood, J.; McCarthy, T. J., Ultrahydrophobic and ultralyophobic surfaces: Some comments and examples. *Langmuir* **1999,** 15, (10), 3395-3399.
152. Fadeev, A. Y.; McCarthy, T. J., Trialkylsilane monolayers covalently attached to silicon surfaces: Wettability studies indicating that molecular topography contributes to

contact angle hysteresis. *Langmuir* **1999,** 15, (11), 3759-3766.
153. Youngblood, J. P.; McCarthy, T. J., Ultrahydrophobic polymer surfaces prepared by simultaneous ablation of polypropylene and sputtering of poly(tetrafluoroethylene) using radio frequency plasma. *Abstracts of Papers of the American Chemical Society* **1999,** 218, U408-U408.
154. Oner, D.; McCarthy, T. J., Ultrahydrophobic surfaces. Effects of topography length scales on wettability. *Langmuir* **2000,** 16, (20), 7777-7782.
155. Gao, L. C.; McCarthy, T. J., A perfectly hydrophobic surface (theta(A)/theta(R)=180 degrees/180 degrees). *Journal of the American Chemical Society* **2006,** 128, (28), 9052-9053.
156. Gao, L. C.; McCarthy, T. J., How Wenzel and Cassie were wrong. *Langmuir* **2007,** 23, (7), 3762-3765.
157. Crassous, J.; Charlaix, E.; Gayvallet, H.; Loubet, J. L., Experimental-Study of a Nanometric Liquid Bridge with a Surface Force Apparatus. *Langmuir* **1993,** 9, (8), 1995-1998.
158. Adams, M. J.; Perchard, V., The Cohesive Forces between Particles with Interstitial Liquid. *I.Chem. Eng. Symp. Series* **1984,** 91, (147), 147-160.
159. Mazzone, D. N.; Tardos, G. I.; Pfeffer, R., The Behavior of Liquid Bridges between 2 Relatively Moving Particles. *Powder Technology* **1987,** 51, (1), 71-83.
160. Ennis, B. J.; Li, J. L.; Tardos, G. I.; Pfeffer, R., The Influence of Viscosity on the Strength of an Axially Strained Pendular Liquid Bridge. *Chemical Engineering Science* **1990,** 45, (10), 3071-3088.
161. Pitois, O.; Moucheront, P.; Chateau, X., Liquid bridge between two moving spheres: An experimental study of viscosity effects. *Journal of Colloid and Interface Science* **2000,** 231, (1), 26-31.
162. Pitois, O.; Moucheront, P.; Chateau, X., Rupture energy of a pendular liquid bridge. *European Physical Journal B* **2001,** 23, (1), 79-86.
163. Stefan, J., Versuche über die scheinbare Adhäsion. *Sitzber. Akad. Wiss. Wien* **1874,** 69, 713-735.
164. Debisschop, F. R. E.; Rigole, W. J. L., A Physical Model for Liquid Capillary Bridges between Adsorptive Solid Spheres - the Nodoid of Plateau. *Journal of Colloid and Interface Science* **1982,** 88, (1), 117-128.
165. De Souza, E. J.; Gao, L. C.; McCarthy, T. J.; Arzt, E.; Crosby, A. J., Effect of contact angle hysteresis on the measurement of capillary forces. *Submitted for publication* **2007**.
166. De Souza, E. J.; Brinkmann, M.; Mohrdieck, C.; Crosby, A. J.; Arzt, E., Capillary forces between chemically different substrates. *Submitted for publication* **2007**.
167. Sirghi, L.; Nakamura, M.; Hatanaka, Y.; Takai, O., Atomic force microscopy study of the hydrophilicity of TiO2 thin films obtained by radio frequency magnetron sputtering and plasma enhanced chemical vapor depositions. *Langmuir* **2001,** 17, (26), 8199-8203.
168. Tselishchev, Y. G.; Val'tsifer, V. A., Influence of the type of contact between particles joined by a liquid bridge on the capillary cohesive forces. *Colloid Journal* **2003,** 65, (3), 385-389.
169. Jones, R.; Pollock, H. M.; Cleaver, J. A. S.; Hodges, C. S., Adhesion forces between glass and silicon surfaces in air studied by AFM: Effects of relative humidity, particle size, roughness, and surface treatment. *Langmuir* **2002,** 18, (21), 8045-8055.
170. Pakarinen, O. H.; Foster, A. S.; Paajanen, M.; Kalinainen, T.; Katainen, J.; Makkonen, I.; Lahtinen, J.; Nieminen, R. M., Towards an accurate description of the capillary force in nanoparticle-surface interactions. *Modelling and Simulation in Materials Science and Engineering* **2005,** 13, (7), 1175-1186.
171. Del Campo, A.; Greiner, C.; Arzt, E., Contact shape controls adhesion of bioinspired fibrillar surfaces. *Submitted for publication* **2007**.
172. Duong, N. H.; Shen, E.; Shinbrot, T.; Muzzio, F., Segregation in granular materials

and the direct measurement of surface forces using atomic force microscopy. *Powder Technology* **2004,** 145, (1), 69-72.

# Appendix

## Scriptum for liquid bridges between two plates

### Definition of parameters:

```
PARAMETER capillary_length=1
PARAMETER length_max=0.020
PARAMETER length_min=0.004
PARAMETER total_volume=4/3*Pi
PARAMETER initial_distance=0.01
PARAMETER initial_radius_substrate=2/sqrt(3*initial_distance)
PARAMETER end_distance=2.5
PARAMETER distance_factor=1.01
PARAMETER old_distance=initial_distance;
PARAMETER new_distance=initial_distance;
PARAMETER distance=initial_distance
PARAMETER contactangle_bottom=120
PARAMETER contactangle_top=60
PARAMETER wetability_bottom=-cos(Pi/180*contactangle_bottom)
PARAMETER wetability_top=-cos(Pi/180*contactangle_top)
```

### definition of diverse energies:

```
quantity interfacial_energy energy global_method edge_scalar_integral
scalar_integrand:  2*Pi*x1
quantity substrate_energy_bottom energy method vertex_scalar_integral
scalar_integrand:  wetability_bottom*Pi*x1*x1
quantity substrate_energy_top energy method vertex_scalar_integral
scalar_integrand:  wetability_top*Pi*x1*x1
quantity gravitation_energy energy global_method edge_vector_integral
vector_integrand:
q1:  -0*Pi*x1*x2*x2/(capillary_length*capillary_length)
q2:  0
q3:  0
quantity drop_volume fixed=total_volume global_method edge_vector_integral
```

```
vector_integrand:
q1:  0
q2:  Pi*x1*x1
q3:  0
quantity substrate_radius info_only method vertex_scalar_integral
scalar_integrand:  x1
```

**constraints:**

```
constraint 1
formula:  x3=0
constraint 2
formula:  x2=0
constraint 3
formula:  x2=distance
constraint 4 nonnegative
formula:  x1
constraint 5 nonpositive
formula:  abs(x2-distance/2)-distance/2
```

**list of vertices:**

```
vertices
1 initial_radius_substrate 0 0 constraint 1 2 4 substrate_energy_bottom substrate_radius
2 initial_radius_substrate initial_distance 0 constraint 1 3 4 substrate_energy_top
```

**list of edges:** `edges 1 1 2 tension 0 constraint 1 4 5`

```
read
gv:= {
U;
r; g;
r; g;
r; g;
filename := sprintf
```

```
"/fux5/scratch/souza/orig_%g_%g.dat",
contactangle_bottom, contactangle_top;
while(old_distance<=end_distance) do {
jj:=0;
while(jj<100) do {
refine edges ee where ee.length > length_max;
g 5;
delete edges ee where ee.length < length_min;
g 5;
jj:=jj+1;
};
minimal_radius:=100;
foreach vertex vv do {if(vv.x1<minimal_radius) then minimal_radius:=vv.x1 };
printf ''%f\t% f\t%f\t%f\n'', distance, minimal_radius, substrate_radius.value,
total_energy >> filename;
new_distance:=old_distance*distance_factor;
jj:=0;
while(jj<100) do {
distance:=distance+(new_distance-old_distance)/100;
g;
refine edges ee where ee.length > length_max;
jj:=jj+1;
};
old_distance:=new_distance;
}; };
```

# Carter's calculation with Mathematica

## Definitions:

Def. of the z-coordinate of the undoloid as a function of the parameters "ro" (rmax) and "ri" (rmin) and the radius r:

$z[\mathbf{ro\_, ri\_, r\_}] = \mathbf{ro} * \mathbf{EllipticE}[k[\mathbf{ro, ri}, r], \mathbf{modul[ro, ri]}] + \mathbf{ri} * \mathbf{EllipticF}[k[\mathbf{ro, ri}, r], \mathbf{modul[ro, ri]}] -$
$1/r * \mathbf{Sqrt}[(\mathbf{ro\text{^}2} - r\text{^}2) * (r\text{^}2 - \mathbf{ri\text{^}2})]$

$$-\frac{\sqrt{\left(r^2-\mathrm{ri}^2\right)\left(-r^2+\mathrm{ro}^2\right)}}{r}+\mathrm{roEllipticE}[k[\mathrm{ro},\mathrm{ri},r],\mathrm{modul}[\mathrm{ro},\mathrm{ri}]]+\mathrm{riEllipticF}[k[\mathrm{ro},\mathrm{ri},r],\mathrm{modul}[\mathrm{ro},\mathrm{ri}]]$$

Def. of the phase "k", appearing in the incomplete elliptic integrals F and E:

$k[\mathbf{ro\_, ri\_, r\_}] = \mathbf{ArcSin}[\mathbf{Sqrt}[\mathbf{ro\text{^}2}(r\text{^}2 - \mathbf{ri\text{^}2})/(r\text{^}2 * (\mathbf{ro\text{^}2} - \mathbf{ri\text{^}2}))]]$

$$\mathrm{ArcSin}\left[\sqrt{\frac{\left(r^2-\mathrm{ri}^2\right)\mathrm{ro}^2}{r^2\left(-\mathrm{ri}^2+\mathrm{ro}^2\right)}}\right]$$

Def. of modul "modul" (!), in F and E:

$\mathbf{modul}[\mathbf{ro\_, ri\_}] = (\mathbf{ro\text{^}2} - \mathbf{ri\text{^}2})/\mathbf{ro\text{^}2}$

$$\frac{-\mathrm{ri}^2+\mathrm{ro}^2}{\mathrm{ro}^2}$$

First derivative "zd"of z with resp. to r (needed for the contact angle later):

$\mathbf{zd}[\mathbf{ro\_, ri\_, r\_}] = (r\text{^}2 + \mathbf{ro} * \mathbf{ri})/\mathbf{Sqrt}[(\mathbf{ro\text{^}2} - r\text{^}2) * (r\text{^}2 - \mathbf{ri\text{^}2})]$

$$\frac{r^2+\mathrm{riro}}{\sqrt{\left(r^2-\mathrm{ri}^2\right)\left(-r^2+\mathrm{ro}^2\right)}}$$

$\mathbf{distsmallthetaneck}[\mathbf{ro\_, rn\_, rs\_, re\_}] = z[\mathbf{ro, rn, rs}] + z[\mathbf{ro, rn, re}]$

$$-\frac{\sqrt{(\mathrm{re}^2-\mathrm{rn}^2)(-\mathrm{re}^2+\mathrm{ro}^2)}}{\mathrm{re}}-\frac{\sqrt{(\mathrm{ro}^2-\mathrm{rs}^2)(-\mathrm{rn}^2+\mathrm{rs}^2)}}{\mathrm{rs}}+$$
$$\mathrm{roEllipticE}\left[\mathrm{ArcSin}\left[\sqrt{\frac{(\mathrm{re}^2-\mathrm{rn}^2)\mathrm{ro}^2}{\mathrm{re}^2(-\mathrm{rn}^2+\mathrm{ro}^2)}}\right],\frac{-\mathrm{rn}^2+\mathrm{ro}^2}{\mathrm{ro}^2}\right]+\mathrm{roEllipticE}\left[\mathrm{ArcSin}\left[\sqrt{\frac{\mathrm{ro}^2(-\mathrm{rn}^2+\mathrm{rs}^2)}{(-\mathrm{rn}^2+\mathrm{ro}^2)\mathrm{rs}^2}}\right],\frac{-\mathrm{rn}^2+\mathrm{ro}^2}{\mathrm{ro}^2}\right]+$$
$$\mathrm{rnEllipticF}\left[\mathrm{ArcSin}\left[\sqrt{\frac{(\mathrm{re}^2-\mathrm{rn}^2)\mathrm{ro}^2}{\mathrm{re}^2(-\mathrm{rn}^2+\mathrm{ro}^2)}}\right],\frac{-\mathrm{rn}^2+\mathrm{ro}^2}{\mathrm{ro}^2}\right]+\mathrm{rnEllipticF}\left[\mathrm{ArcSin}\left[\sqrt{\frac{\mathrm{ro}^2(-\mathrm{rn}^2+\mathrm{rs}^2)}{(-\mathrm{rn}^2+\mathrm{ro}^2)\mathrm{rs}^2}}\right],\frac{-\mathrm{rn}^2+\mathrm{ro}^2}{\mathrm{ro}^2}\right]$$

$\mathbf{distsmallthetanoneck}[\mathbf{ro\_, rn\_, rs\_, re\_}] = z[\mathbf{ro, rn, rs}] - z[\mathbf{ro, rn, re}]$

$$\frac{\sqrt{(\mathrm{re}^2-\mathrm{rn}^2)(-\mathrm{re}^2+\mathrm{ro}^2)}}{\mathrm{re}}-\frac{\sqrt{(\mathrm{ro}^2-\mathrm{rs}^2)(-\mathrm{rn}^2+\mathrm{rs}^2)}}{\mathrm{rs}}-$$
$$\mathrm{roEllipticE}\left[\mathrm{ArcSin}\left[\sqrt{\frac{(\mathrm{re}^2-\mathrm{rn}^2)\mathrm{ro}^2}{\mathrm{re}^2(-\mathrm{rn}^2+\mathrm{ro}^2)}}\right],\frac{-\mathrm{rn}^2+\mathrm{ro}^2}{\mathrm{ro}^2}\right]+\mathrm{roEllipticE}\left[\mathrm{ArcSin}\left[\sqrt{\frac{\mathrm{ro}^2(-\mathrm{rn}^2+\mathrm{rs}^2)}{(-\mathrm{rn}^2+\mathrm{ro}^2)\mathrm{rs}^2}}\right],\frac{-\mathrm{rn}^2+\mathrm{ro}^2}{\mathrm{ro}^2}\right]-$$
$$\mathrm{rnEllipticF}\left[\mathrm{ArcSin}\left[\sqrt{\frac{(\mathrm{re}^2-\mathrm{rn}^2)\mathrm{ro}^2}{\mathrm{re}^2(-\mathrm{rn}^2+\mathrm{ro}^2)}}\right],\frac{-\mathrm{rn}^2+\mathrm{ro}^2}{\mathrm{ro}^2}\right]+\mathrm{rnEllipticF}\left[\mathrm{ArcSin}\left[\sqrt{\frac{\mathrm{ro}^2(-\mathrm{rn}^2+\mathrm{rs}^2)}{(-\mathrm{rn}^2+\mathrm{ro}^2)\mathrm{rs}^2}}\right],\frac{-\mathrm{rn}^2+\mathrm{ro}^2}{\mathrm{ro}^2}\right]$$

$\mathbf{distlargethetaneck}[\mathbf{ro\_, rn\_, rs\_, re\_}] = 2 * z[\mathbf{ro, rn, ro}] - z[\mathbf{ro, rn, rs}] + z[\mathbf{ro, rn, re}]$

$$-\frac{\sqrt{(\mathrm{re}^2-\mathrm{rn}^2)(-\mathrm{re}^2+\mathrm{ro}^2)}}{\mathrm{re}}+\frac{\sqrt{(\mathrm{ro}^2-\mathrm{rs}^2)(-\mathrm{rn}^2+\mathrm{rs}^2)}}{\mathrm{rs}}+\mathrm{roEllipticE}\left[\mathrm{ArcSin}\left[\sqrt{\frac{(\mathrm{re}^2-\mathrm{rn}^2)\mathrm{ro}^2}{\mathrm{re}^2(-\mathrm{rn}^2+\mathrm{ro}^2)}}\right],\frac{-\mathrm{rn}^2+\mathrm{ro}^2}{\mathrm{ro}^2}\right]-$$
$$\mathrm{roEllipticE}\left[\mathrm{ArcSin}\left[\sqrt{\frac{\mathrm{ro}^2(-\mathrm{rn}^2+\mathrm{rs}^2)}{(-\mathrm{rn}^2+\mathrm{ro}^2)\mathrm{rs}^2}}\right],\frac{-\mathrm{rn}^2+\mathrm{ro}^2}{\mathrm{ro}^2}\right]+\mathrm{rnEllipticF}\left[\mathrm{ArcSin}\left[\sqrt{\frac{(\mathrm{re}^2-\mathrm{rn}^2)\mathrm{ro}^2}{\mathrm{re}^2(-\mathrm{rn}^2+\mathrm{ro}^2)}}\right],\frac{-\mathrm{rn}^2+\mathrm{ro}^2}{\mathrm{ro}^2}\right]-$$

$$\text{rnEllipticF}\left[\text{ArcSin}\left[\sqrt{\frac{\text{ro}^2(-\text{rn}^2+\text{rs}^2)}{(-\text{rn}^2+\text{ro}^2)\text{rs}^2}}\right],\frac{-\text{rn}^2+\text{ro}^2}{\text{ro}^2}\right]+2\left(\text{roEllipticE}\left[\frac{-\text{rn}^2+\text{ro}^2}{\text{ro}^2}\right]+\text{rnEllipticK}\left[\frac{-\text{rn}^2+\text{ro}^2}{\text{ro}^2}\right]\right)$$

**distlargethetanoneck[ro_, rn_, rs_, re_] =**

**2 * z[ro, rn, ro] − z[ro, rn, rs] − z[ro, rn, re]**

$$\frac{\sqrt{(\text{re}^2-\text{rn}^2)(-\text{re}^2+\text{ro}^2)}}{\text{re}}+\frac{\sqrt{(\text{ro}^2-\text{rs}^2)(-\text{rn}^2+\text{rs}^2)}}{\text{rs}}-\text{roEllipticE}\left[\text{ArcSin}\left[\sqrt{\frac{(\text{re}^2-\text{rn}^2)\text{ro}^2}{\text{re}^2(-\text{rn}^2+\text{ro}^2)}}\right],\frac{-\text{rn}^2+\text{ro}^2}{\text{ro}^2}\right]-$$
$$\text{roEllipticE}\left[\text{ArcSin}\left[\sqrt{\frac{\text{ro}^2(-\text{rn}^2+\text{rs}^2)}{(-\text{rn}^2+\text{ro}^2)\text{rs}^2}}\right],\frac{-\text{rn}^2+\text{ro}^2}{\text{ro}^2}\right]-\text{rnEllipticF}\left[\text{ArcSin}\left[\sqrt{\frac{(\text{re}^2-\text{rn}^2)\text{ro}^2}{\text{re}^2(-\text{rn}^2+\text{ro}^2)}}\right],\frac{-\text{rn}^2+\text{ro}^2}{\text{ro}^2}\right]-$$

$$\text{rnEllipticF}\left[\text{ArcSin}\left[\sqrt{\frac{\text{ro}^2(-\text{rn}^2+\text{rs}^2)}{(-\text{rn}^2+\text{ro}^2)\text{rs}^2}}\right],\frac{-\text{rn}^2+\text{ro}^2}{\text{ro}^2}\right]+2\left(\text{roEllipticE}\left[\frac{-\text{rn}^2+\text{ro}^2}{\text{ro}^2}\right]+\text{rnEllipticK}\left[\frac{-\text{rn}^2+\text{ro}^2}{\text{ro}^2}\right]\right)$$

**area[ro_, ri_, r_] = 2 * Pi * ro * (ro + ri) * EllipticE[k[ro, ri, r], modul[ro, ri]]−**

**2 * Pi * (ro + ri) * Sqrt[(ro^2 − r^2) * (r^2 − ri^2)]/r**

$$-\frac{2\pi(\text{ri}+\text{ro})\sqrt{\left(r^2-\text{ri}^2\right)(-r^2+\text{ro}^2)}}{r}+2\pi\text{ro}(\text{ri}+\text{ro})\text{EllipticE}\left[\text{ArcSin}\left[\sqrt{\frac{\left(r^2-\text{ri}^2\right)\text{ro}^2}{r^2\left(-\text{ri}^2+\text{ro}^2\right)}}\right],\frac{-\text{ri}^2+\text{ro}^2}{\text{ro}^2}\right]$$

**areasmallthetanoneck[ro_, rn_, rs_, re_] = area[ro, rn, rs] − area[ro, rn, re]**

$$\frac{2\pi(\text{rn}+\text{ro})\sqrt{(\text{re}^2-\text{rn}^2)(-\text{re}^2+\text{ro}^2)}}{\text{re}}-\frac{2\pi(\text{rn}+\text{ro})\sqrt{(\text{ro}^2-\text{rs}^2)(-\text{rn}^2+\text{rs}^2)}}{\text{rs}}-$$
$$2\pi\text{ro}(\text{rn}+\text{ro})\text{EllipticE}\left[\text{ArcSin}\left[\sqrt{\frac{(\text{re}^2-\text{rn}^2)\text{ro}^2}{\text{re}^2(-\text{rn}^2+\text{ro}^2)}}\right],\frac{-\text{rn}^2+\text{ro}^2}{\text{ro}^2}\right]+$$
$$2\pi\text{ro}(\text{rn}+\text{ro})\text{EllipticE}\left[\text{ArcSin}\left[\sqrt{\frac{\text{ro}^2(-\text{rn}^2+\text{rs}^2)}{(-\text{rn}^2+\text{ro}^2)\text{rs}^2}}\right],\frac{-\text{rn}^2+\text{ro}^2}{\text{ro}^2}\right]$$

**areasmallthetaneck[ro_, rn_, rs_, re_] = area[ro, rn, rs] + area[ro, rn, re]**

$$-\frac{2\pi(\text{rn}+\text{ro})\sqrt{(\text{re}^2-\text{rn}^2)(-\text{re}^2+\text{ro}^2)}}{\text{re}}-\frac{2\pi(\text{rn}+\text{ro})\sqrt{(\text{ro}^2-\text{rs}^2)(-\text{rn}^2+\text{rs}^2)}}{\text{rs}}+$$
$$2\pi\text{ro}(\text{rn}+\text{ro})\text{EllipticE}\left[\text{ArcSin}\left[\sqrt{\frac{(\text{re}^2-\text{rn}^2)\text{ro}^2}{\text{re}^2(-\text{rn}^2+\text{ro}^2)}}\right],\frac{-\text{rn}^2+\text{ro}^2}{\text{ro}^2}\right]+$$
$$2\pi\text{ro}(\text{rn}+\text{ro})\text{EllipticE}\left[\text{ArcSin}\left[\sqrt{\frac{\text{ro}^2(-\text{rn}^2+\text{rs}^2)}{(-\text{rn}^2+\text{ro}^2)\text{rs}^2}}\right],\frac{-\text{rn}^2+\text{ro}^2}{\text{ro}^2}\right]$$

**arealargethetanoneck[ro_, rn_, rs_, re_] = 2 * area[ro, rn, ro] − area[ro, rn, rs] − area[ro, rn, re]**

$$\frac{2\pi(\text{rn}+\text{ro})\sqrt{(\text{re}^2-\text{rn}^2)(-\text{re}^2+\text{ro}^2)}}{\text{re}}+\frac{2\pi(\text{rn}+\text{ro})\sqrt{(\text{ro}^2-\text{rs}^2)(-\text{rn}^2+\text{rs}^2)}}{\text{rs}}+$$
$$4\pi\text{ro}(\text{rn}+\text{ro})\text{EllipticE}\left[\frac{-\text{rn}^2+\text{ro}^2}{\text{ro}^2}\right]-2\pi\text{ro}(\text{rn}+\text{ro})\text{EllipticE}\left[\text{ArcSin}\left[\sqrt{\frac{(\text{re}^2-\text{rn}^2)\text{ro}^2}{\text{re}^2(-\text{rn}^2+\text{ro}^2)}}\right],\frac{-\text{rn}^2+\text{ro}^2}{\text{ro}^2}\right]-$$

$$2\pi\text{ro}(\text{rn}+\text{ro})\text{EllipticE}\left[\text{ArcSin}\left[\sqrt{\frac{\text{ro}^2(-\text{rn}^2+\text{rs}^2)}{(-\text{rn}^2+\text{ro}^2)\text{rs}^2}}\right],\frac{-\text{rn}^2+\text{ro}^2}{\text{ro}^2}\right]$$

**arealargethetaneck[ro_, rn_, rs_, re_] = 2 * area[ro, rn, ro] − area[ro, rn, rs] + area[ro, rn, re]**

$$-\frac{2\pi(\text{rn}+\text{ro})\sqrt{(\text{re}^2-\text{rn}^2)(-\text{re}^2+\text{ro}^2)}}{\text{re}}+\frac{2\pi(\text{rn}+\text{ro})\sqrt{(\text{ro}^2-\text{rs}^2)(-\text{rn}^2+\text{rs}^2)}}{\text{rs}}+$$
$$4\pi\text{ro}(\text{rn}+\text{ro})\text{EllipticE}\left[\frac{-\text{rn}^2+\text{ro}^2}{\text{ro}^2}\right]+2\pi\text{ro}(\text{rn}+\text{ro})\text{EllipticE}\left[\text{ArcSin}\left[\sqrt{\frac{(\text{re}^2-\text{rn}^2)\text{ro}^2}{\text{re}^2(-\text{rn}^2+\text{ro}^2)}}\right],\frac{-\text{rn}^2+\text{ro}^2}{\text{ro}^2}\right]-$$

$$2\pi\text{ro}(\text{rn}+\text{ro})\text{EllipticE}\left[\text{ArcSin}\left[\sqrt{\frac{\text{ro}^2(-\text{rn}^2+\text{rs}^2)}{(-\text{rn}^2+\text{ro}^2)\text{rs}^2}}\right],\frac{-\text{rn}^2+\text{ro}^2}{\text{ro}^2}\right]$$

Volume "V" of the undoloid between ri and r

**vol[ro_, ri_, r_] =**

**Pi/3 * ((2 * ro^3 + 2 * ri^2 * ro + 3 * ro^2 * ri) * EllipticE[k[ro, ri, r], modul[ro, ri]]−**

$$\mathbf{ro * ri\text{^}2 * EllipticF[}k\mathbf{[ro, ri,}\, r\mathbf{], modul[ro, ri]]} -$$

$$\mathbf{(}r\mathbf{\text{^}2 + 2 * ro\text{^}2 + 2 * ri\text{^}2 + 3 * ro * ri) * Sqrt[(ro\text{^}2 - }r\mathbf{\text{^}2) * (}r\mathbf{\text{^}2 - ri\text{^}2)]/}r\mathbf{)}$$

$$\frac{1}{3}\pi\left(-\frac{\sqrt{\left(r^2-\mathbf{ri}^2\right)(-r^2+\mathbf{ro}^2)}\left(r^2+2\mathbf{ri}^2+3\mathbf{riro}+2\mathbf{ro}^2\right)}{r}+\left(2\mathbf{ri}^2\mathbf{ro}+3\mathbf{riro}^2+2\mathbf{ro}^3\right)\right.$$

$$\left.\mathbf{EllipticE}\left[\mathbf{ArcSin}\left[\sqrt{\frac{\left(r^2-\mathbf{ri}^2\right)\mathbf{ro}^2}{r^2\left(-\mathbf{ri}^2+\mathbf{ro}^2\right)}}\right],\frac{-\mathbf{ri}^2+\mathbf{ro}^2}{\mathbf{ro}^2}\right]-\mathbf{ri}^2\mathbf{roEllipticF}\left[\mathbf{ArcSin}\left[\sqrt{\frac{\left(r^2-\mathbf{ri}^2\right)\mathbf{ro}^2}{r^2\left(-\mathbf{ri}^2+\mathbf{ro}^2\right)}}\right],\frac{-\mathbf{ri}^2+\mathbf{ro}^2}{\mathbf{ro}^2}\right]\right)$$

$$\mathbf{volsmallthetaneck[ro\_, rn\_, rs\_, re\_] = vol[ro, rn, rs] + vol[ro, rn, re]}$$

$$\frac{1}{3}\pi\left(-\frac{\sqrt{(\mathbf{re}^2-\mathbf{rn}^2)(-\mathbf{re}^2+\mathbf{ro}^2)}\left(\mathbf{re}^2+2\mathbf{rn}^2+3\mathbf{rnro}+2\mathbf{ro}^2\right)}{\mathbf{re}}+(2\mathbf{rn}^2\mathbf{ro}+3\mathbf{rnro}^2+2\mathbf{ro}^3)\right.$$

$$\left.\mathbf{EllipticE}\left[\mathbf{ArcSin}\left[\sqrt{\frac{(\mathbf{re}^2-\mathbf{rn}^2)\mathbf{ro}^2}{\mathbf{re}^2(-\mathbf{rn}^2+\mathbf{ro}^2)}}\right],\frac{-\mathbf{rn}^2+\mathbf{ro}^2}{\mathbf{ro}^2}\right]-\mathbf{rn}^2\mathbf{roEllipticF}\left[\mathbf{ArcSin}\left[\sqrt{\frac{(\mathbf{re}^2-\mathbf{rn}^2)\mathbf{ro}^2}{\mathbf{re}^2(-\mathbf{rn}^2+\mathbf{ro}^2)}}\right],\frac{-\mathbf{rn}^2+\mathbf{ro}^2}{\mathbf{ro}^2}\right]\right)$$

$$\frac{1}{3}\pi\left(-\frac{\sqrt{(\mathbf{ro}^2-\mathbf{rs}^2)(-\mathbf{rn}^2+\mathbf{rs}^2)}\left(2\mathbf{rn}^2+3\mathbf{rnro}+2\mathbf{ro}^2+\mathbf{rs}^2\right)}{\mathbf{rs}}+(2\mathbf{rn}^2\mathbf{ro}+3\mathbf{rnro}^2+2\mathbf{ro}^3)\right.$$

$$\left.\mathbf{EllipticE}\left[\mathbf{ArcSin}\left[\sqrt{\frac{\mathbf{ro}^2(-\mathbf{rn}^2+\mathbf{rs}^2)}{(-\mathbf{rn}^2+\mathbf{ro}^2)\mathbf{rs}^2}}\right],\frac{-\mathbf{rn}^2+\mathbf{ro}^2}{\mathbf{ro}^2}\right]-\mathbf{rn}^2\mathbf{roEllipticF}\left[\mathbf{ArcSin}\left[\sqrt{\frac{\mathbf{ro}^2(-\mathbf{rn}^2+\mathbf{rs}^2)}{(-\mathbf{rn}^2+\mathbf{ro}^2)\mathbf{rs}^2}}\right],\frac{-\mathbf{rn}^2+\mathbf{ro}^2}{\mathbf{ro}^2}\right]\right)$$

$$\mathbf{volsmallthetanoneck[ro\_, rn\_, rs\_, re\_] = vol[ro, rn, rs] - vol[ro, rn, re]}$$

$$-\frac{1}{3}\pi\left(-\frac{\sqrt{(\mathbf{re}^2-\mathbf{rn}^2)(-\mathbf{re}^2+\mathbf{ro}^2)}\left(\mathbf{re}^2+2\mathbf{rn}^2+3\mathbf{rnro}+2\mathbf{ro}^2\right)}{\mathbf{re}}+(2\mathbf{rn}^2\mathbf{ro}+3\mathbf{rnro}^2+2\mathbf{ro}^3)\right.$$

$$\left.\mathbf{EllipticE}\left[\mathbf{ArcSin}\left[\sqrt{\frac{(\mathbf{re}^2-\mathbf{rn}^2)\mathbf{ro}^2}{\mathbf{re}^2(-\mathbf{rn}^2+\mathbf{ro}^2)}}\right],\frac{-\mathbf{rn}^2+\mathbf{ro}^2}{\mathbf{ro}^2}\right]-\mathbf{rn}^2\mathbf{roEllipticF}\left[\mathbf{ArcSin}\left[\sqrt{\frac{(\mathbf{re}^2-\mathbf{rn}^2)\mathbf{ro}^2}{\mathbf{re}^2(-\mathbf{rn}^2+\mathbf{ro}^2)}}\right],\frac{-\mathbf{rn}^2+\mathbf{ro}^2}{\mathbf{ro}^2}\right]\right)$$

$$\frac{1}{3}\pi\left(-\frac{\sqrt{(\mathbf{ro}^2-\mathbf{rs}^2)(-\mathbf{rn}^2+\mathbf{rs}^2)}\left(2\mathbf{rn}^2+3\mathbf{rnro}+2\mathbf{ro}^2+\mathbf{rs}^2\right)}{\mathbf{rs}}+(2\mathbf{rn}^2\mathbf{ro}+3\mathbf{rnro}^2+2\mathbf{ro}^3)\right.$$

$$\left.\mathbf{EllipticE}\left[\mathbf{ArcSin}\left[\sqrt{\frac{\mathbf{ro}^2(-\mathbf{rn}^2+\mathbf{rs}^2)}{(-\mathbf{rn}^2+\mathbf{ro}^2)\mathbf{rs}^2}}\right],\frac{-\mathbf{rn}^2+\mathbf{ro}^2}{\mathbf{ro}^2}\right]-\mathbf{rn}^2\mathbf{roEllipticF}\left[\mathbf{ArcSin}\left[\sqrt{\frac{\mathbf{ro}^2(-\mathbf{rn}^2+\mathbf{rs}^2)}{(-\mathbf{rn}^2+\mathbf{ro}^2)\mathbf{rs}^2}}\right],\frac{-\mathbf{rn}^2+\mathbf{ro}^2}{\mathbf{ro}^2}\right]\right)$$

$$\mathbf{vollargethetaneck[ro\_, rn\_, rs\_, re\_] = 2 * vol[ro, rn, ro] - vol[ro, rn, rs] + vol[ro, rn, re]}$$

$$\frac{1}{3}\pi\left(-\frac{\sqrt{(\mathbf{re}^2-\mathbf{rn}^2)(-\mathbf{re}^2+\mathbf{ro}^2)}\left(\mathbf{re}^2+2\mathbf{rn}^2+3\mathbf{rnro}+2\mathbf{ro}^2\right)}{\mathbf{re}}+(2\mathbf{rn}^2\mathbf{ro}+3\mathbf{rnro}^2+2\mathbf{ro}^3)\right.$$

$$\left.\mathbf{EllipticE}\left[\mathbf{ArcSin}\left[\sqrt{\frac{(\mathbf{re}^2-\mathbf{rn}^2)\mathbf{ro}^2}{\mathbf{re}^2(-\mathbf{rn}^2+\mathbf{ro}^2)}}\right],\frac{-\mathbf{rn}^2+\mathbf{ro}^2}{\mathbf{ro}^2}\right]-\mathbf{rn}^2\mathbf{roEllipticF}\left[\mathbf{ArcSin}\left[\sqrt{\frac{(\mathbf{re}^2-\mathbf{rn}^2)\mathbf{ro}^2}{\mathbf{re}^2(-\mathbf{rn}^2+\mathbf{ro}^2)}}\right],\frac{-\mathbf{rn}^2+\mathbf{ro}^2}{\mathbf{ro}^2}\right]\right)$$

$$\frac{1}{3}\pi\left(-\frac{\sqrt{(\mathbf{ro}^2-\mathbf{rs}^2)(-\mathbf{rn}^2+\mathbf{rs}^2)}\left(2\mathbf{rn}^2+3\mathbf{rnro}+2\mathbf{ro}^2+\mathbf{rs}^2\right)}{\mathbf{rs}}+(2\mathbf{rn}^2\mathbf{ro}+3\mathbf{rnro}^2+2\mathbf{ro}^3)\right.$$

$$\left.\mathbf{EllipticE}\left[\mathbf{ArcSin}\left[\sqrt{\frac{\mathbf{ro}^2(-\mathbf{rn}^2+\mathbf{rs}^2)}{(-\mathbf{rn}^2+\mathbf{ro}^2)\mathbf{rs}^2}}\right],\frac{-\mathbf{rn}^2+\mathbf{ro}^2}{\mathbf{ro}^2}\right]-\mathbf{rn}^2\mathbf{roEllipticF}\left[\mathbf{ArcSin}\left[\sqrt{\frac{\mathbf{ro}^2(-\mathbf{rn}^2+\mathbf{rs}^2)}{(-\mathbf{rn}^2+\mathbf{ro}^2)\mathbf{rs}^2}}\right],\frac{-\mathbf{rn}^2+\mathbf{ro}^2}{\mathbf{ro}^2}\right]\right)$$

$$\frac{2}{3}\pi\left((2\mathbf{rn}^2\mathbf{ro}+3\mathbf{rnro}^2+2\mathbf{ro}^3)\,\mathbf{EllipticE}\left[\frac{-\mathbf{rn}^2+\mathbf{ro}^2}{\mathbf{ro}^2}\right]-\mathbf{rn}^2\mathbf{roEllipticK}\left[\frac{-\mathbf{rn}^2+\mathbf{ro}^2}{\mathbf{ro}^2}\right]\right)$$

$$\mathbf{vollargethetanoneck[ro\_, rn\_, rs\_, re\_] = 2 * vol[ro, rn, ro] - vol[ro, rn, rs] - vol[ro, rn, re]}$$

$$-\frac{1}{3}\pi\left(-\frac{\sqrt{(\mathbf{re}^2-\mathbf{rn}^2)(-\mathbf{re}^2+\mathbf{ro}^2)}\left(\mathbf{re}^2+2\mathbf{rn}^2+3\mathbf{rnro}+2\mathbf{ro}^2\right)}{\mathbf{re}}+(2\mathbf{rn}^2\mathbf{ro}+3\mathbf{rnro}^2+2\mathbf{ro}^3)\right.$$

$$\left.\mathbf{EllipticE}\left[\mathbf{ArcSin}\left[\sqrt{\frac{(\mathbf{re}^2-\mathbf{rn}^2)\mathbf{ro}^2}{\mathbf{re}^2(-\mathbf{rn}^2+\mathbf{ro}^2)}}\right],\frac{-\mathbf{rn}^2+\mathbf{ro}^2}{\mathbf{ro}^2}\right]-\mathbf{rn}^2\mathbf{roEllipticF}\left[\mathbf{ArcSin}\left[\sqrt{\frac{(\mathbf{re}^2-\mathbf{rn}^2)\mathbf{ro}^2}{\mathbf{re}^2(-\mathbf{rn}^2+\mathbf{ro}^2)}}\right],\frac{-\mathbf{rn}^2+\mathbf{ro}^2}{\mathbf{ro}^2}\right]\right)$$

$$\frac{1}{3}\pi\left(-\frac{\sqrt{(\mathbf{ro}^2-\mathbf{rs}^2)(-\mathbf{rn}^2+\mathbf{rs}^2)}\left(2\mathbf{rn}^2+3\mathbf{rnro}+2\mathbf{ro}^2+\mathbf{rs}^2\right)}{\mathbf{rs}}+(2\mathbf{rn}^2\mathbf{ro}+3\mathbf{rnro}^2+2\mathbf{ro}^3)\right.$$

$$\left.\mathbf{EllipticE}\left[\mathbf{ArcSin}\left[\sqrt{\frac{\mathbf{ro}^2(-\mathbf{rn}^2+\mathbf{rs}^2)}{(-\mathbf{rn}^2+\mathbf{ro}^2)\mathbf{rs}^2}}\right],\frac{-\mathbf{rn}^2+\mathbf{ro}^2}{\mathbf{ro}^2}\right]-\mathbf{rn}^2\mathbf{roEllipticF}\left[\mathbf{ArcSin}\left[\sqrt{\frac{\mathbf{ro}^2(-\mathbf{rn}^2+\mathbf{rs}^2)}{(-\mathbf{rn}^2+\mathbf{ro}^2)\mathbf{rs}^2}}\right],\frac{-\mathbf{rn}^2+\mathbf{ro}^2}{\mathbf{ro}^2}\right]\right)$$

$$\frac{2}{3}\pi\left((2\text{rn}^2\text{ro}+3\text{rnro}^2+2\text{ro}^3)\,\text{EllipticE}\left[\frac{-\text{rn}^2+\text{ro}^2}{\text{ro}^2}\right]-\text{rn}^2\text{roEllipticK}\left[\frac{-\text{rn}^2+\text{ro}^2}{\text{ro}^2}\right]\right)$$

**Solve[Tan[$\theta$]^2 − (x + ro ∗ ri)^2/(ro^2 − x)/(x − ri^2) == 0, x]**

$$\left\{\left\{x\to\frac{1}{2(-1-\text{Tan}[\theta]^2)}\left(2\text{riro}-\text{ri}^2\text{Tan}[\theta]^2-\text{ro}^2\text{Tan}[\theta]^2-\right.\right.\right.$$
$$\left.\left.\left.(\text{ri}+\text{ro})\text{Tan}[\theta]\sqrt{-4\text{riro}+\text{ri}^2\text{Tan}[\theta]^2-2\text{riro}\text{Tan}[\theta]^2+\text{ro}^2\text{Tan}[\theta]^2}\right)\right\},$$
$$\left\{x\to\frac{1}{2(-1-\text{Tan}[\theta]^2)}\left(2\text{riro}-\text{ri}^2\text{Tan}[\theta]^2-\text{ro}^2\text{Tan}[\theta]^2+\right.\right.$$
$$\left.\left.\left.(\text{ri}+\text{ro})\text{Tan}[\theta]\sqrt{-4\text{riro}+\text{ri}^2\text{Tan}[\theta]^2-2\text{riro}\text{Tan}[\theta]^2+\text{ro}^2\text{Tan}[\theta]^2}\right)\right\}\right\}$$

**rsup[ro_, ri_, theta_] =**

**Sqrt[**

$$\frac{1}{2(-1-\text{Tan}[\theta]^2)}$$
$$\left(2\text{riro}-\text{ri}^2\text{Tan}[\theta]^2-\text{ro}^2\text{Tan}[\theta]^2-\right.$$
$$\left.(\text{ri}+\text{ro})\text{Tan}[\theta]\sqrt{-4\text{riro}+\text{ri}^2\text{Tan}[\theta]^2-2\text{riro}\text{Tan}[\theta]^2+\text{ro}^2\text{Tan}[\theta]^2}\right)\Bigg]$$
$$\frac{\sqrt{\frac{2\text{riro}-\text{ri}^2\text{Tan}[\theta]^2-\text{ro}^2\text{Tan}[\theta]^2-(\text{ri}+\text{ro})\text{Tan}[\theta]\sqrt{-4\text{riro}+\text{ri}^2\text{Tan}[\theta]^2-2\text{riro}\text{Tan}[\theta]^2+\text{ro}^2\text{Tan}[\theta]^2}}{-1-\text{Tan}[\theta]^2}}}{\sqrt{2}}$$

**rsdown[ro_, ri_, theta_] =**

**Sqrt[**

$$\frac{1}{2(-1-\text{Tan}[\theta]^2)}$$
$$\left(2\text{riro}-\text{ri}^2\text{Tan}[\theta]^2-\text{ro}^2\text{Tan}[\theta]^2+\right.$$
$$\left.(\text{ri}+\text{ro})\text{Tan}[\theta]\sqrt{-4\text{riro}+\text{ri}^2\text{Tan}[\theta]^2-2\text{riro}\text{Tan}[\theta]^2+\text{ro}^2\text{Tan}[\theta]^2}\right)\Bigg]$$
$$\frac{\sqrt{\frac{2\text{riro}-\text{ri}^2\text{Tan}[\theta]^2-\text{ro}^2\text{Tan}[\theta]^2+(\text{ri}+\text{ro})\text{Tan}[\theta]\sqrt{-4\text{riro}+\text{ri}^2\text{Tan}[\theta]^2-2\text{riro}\text{Tan}[\theta]^2+\text{ro}^2\text{Tan}[\theta]^2}}{-1-\text{Tan}[\theta]^2}}}{\sqrt{2}}$$

**romin[theta_] = ((1 + Abs[Cos[$\theta$]])/Sin[$\theta$])^2**

$$(1+\text{Abs}[\text{Cos}[\theta]])^2\text{Csc}[\theta]^2$$

**distlargethetaup[ro_, ri_, theta_] = 2 ∗ distlargethetanoneck[ro, ri, ro, rsup[ro, ri, $\theta$]]**

$$2\left(-\text{roEllipticE}\left[\frac{-\text{ri}^2+\text{ro}^2}{\text{ro}^2}\right]-\right.$$
$$\text{roEllipticE}\left[\text{ArcSin}\left[\sqrt{2}\sqrt{\left(\left(\text{ro}^2\left(-1-\text{Tan}[\theta]^2\right)\left(-\text{ri}^2+\frac{1}{2(-1-\text{Tan}[\theta]^2)}\left(2\text{riro}-\text{ri}^2\text{Tan}[\theta]^2-\text{ro}^2\right.\right.\right.\right.\right.$$
$$\left.\left.\left.\left.\left.\text{Tan}[\theta]^2-(\text{ri}+\text{ro})\text{Tan}[\theta]\sqrt{-4\text{riro}+\text{ri}^2\text{Tan}[\theta]^2-2\text{riro}\text{Tan}[\theta]^2+\text{ro}^2\text{Tan}[\theta]^2}\right)\right)\right)\Big/$$
$$\left(\left(-\text{ri}^2+\text{ro}^2\right)\left(2\text{riro}-\text{ri}^2\text{Tan}[\theta]^2-\text{ro}^2\text{Tan}[\theta]^2-(\text{ri}+\text{ro})\text{Tan}[\theta]\right.\right.$$
$$\left.\left.\left.\sqrt{-4\text{riro}+\text{ri}^2\text{Tan}[\theta]^2-2\text{riro}\text{Tan}[\theta]^2+\text{ro}^2\text{Tan}[\theta]^2}\right)\right)\right)\Bigg],\frac{-\text{ri}^2+\text{ro}^2}{\text{ro}^2}\Bigg]-$$
$$\text{riEllipticF}\left[\text{ArcSin}\left[\sqrt{2}\sqrt{\left(\left(\text{ro}^2\left(-1-\text{Tan}[\theta]^2\right)\left(-\text{ri}^2+\frac{1}{2(-1-\text{Tan}[\theta]^2)}\left(2\text{riro}-\text{ri}^2\text{Tan}[\theta]^2-\text{ro}^2\right.\right.\right.\right.\right.$$
$$\left.\left.\left.\left.\left.\text{Tan}[\theta]^2-(\text{ri}+\text{ro})\text{Tan}[\theta]\sqrt{-4\text{riro}+\text{ri}^2\text{Tan}[\theta]^2-2\text{riro}\text{Tan}[\theta]^2+\text{ro}^2\text{Tan}[\theta]^2}\right)\right)\right)\Big/$$

$$\left(\left(-\mathbf{ri}^2+\mathbf{ro}^2\right)\left(2\mathbf{riro}-\mathbf{ri}^2\mathbf{Tan}[\theta]^2-\mathbf{ro}^2\mathbf{Tan}[\theta]^2-(\mathbf{ri}+\mathbf{ro})\mathbf{Tan}[\theta]\right.\right.$$
$$\left.\left.\sqrt{-4\mathbf{riro}+\mathbf{ri}^2\mathbf{Tan}[\theta]^2-2\mathbf{riro}\mathbf{Tan}[\theta]^2+\mathbf{ro}^2\mathbf{Tan}[\theta]^2}\right)\right)\Big],\tfrac{-\mathbf{ri}^2+\mathbf{ro}^2}{\mathbf{ro}^2}\Big]-$$
$$\mathbf{riEllipticK}\left[\tfrac{-\mathbf{ri}^2+\mathbf{ro}^2}{\mathbf{ro}^2}\right]+2\left(\mathbf{roEllipticE}\left[\tfrac{-\mathbf{ri}^2+\mathbf{ro}^2}{\mathbf{ro}^2}\right]+\mathbf{riEllipticK}\left[\tfrac{-\mathbf{ri}^2+\mathbf{ro}^2}{\mathbf{ro}^2}\right]\right)+$$
$$\left(\sqrt{2}\right.$$
$$\sqrt{\left(\left(\mathbf{ro}^2-\tfrac{1}{2(-1-\mathbf{Tan}[\theta]^2)}\left(2\mathbf{riro}-\mathbf{ri}^2\mathbf{Tan}[\theta]^2-\mathbf{ro}^2\mathbf{Tan}[\theta]^2-\right.\right.\right.}$$
$$\left.\left.\left.(\mathbf{ri}+\mathbf{ro})\mathbf{Tan}[\theta]\sqrt{-4\mathbf{riro}+\mathbf{ri}^2\mathbf{Tan}[\theta]^2-2\mathbf{riro}\mathbf{Tan}[\theta]^2+\mathbf{ro}^2\mathbf{Tan}[\theta]^2}\right)\right)$$
$$\left(-\mathbf{ri}^2+\tfrac{1}{2(-1-\mathbf{Tan}[\theta]^2)}\left(2\mathbf{riro}-\mathbf{ri}^2\mathbf{Tan}[\theta]^2-\mathbf{ro}^2\mathbf{Tan}[\theta]^2-(\mathbf{ri}+\mathbf{ro})\mathbf{Tan}[\theta]\right.\right.$$
$$\left.\left.\left.\sqrt{-4\mathbf{riro}+\mathbf{ri}^2\mathbf{Tan}[\theta]^2-2\mathbf{riro}\mathbf{Tan}[\theta]^2+\mathbf{ro}^2\mathbf{Tan}[\theta]^2}\right)\right)\right)\Big/$$
$$\left(\sqrt{\left(\tfrac{1}{-1-\mathbf{Tan}[\theta]^2}\left(2\mathbf{riro}-\mathbf{ri}^2\mathbf{Tan}[\theta]^2-\mathbf{ro}^2\mathbf{Tan}[\theta]^2-(\mathbf{ri}+\mathbf{ro})\mathbf{Tan}[\theta]\right.\right.\right.$$
$$\left.\left.\left.\sqrt{-4\mathbf{riro}+\mathbf{ri}^2\mathbf{Tan}[\theta]^2-2\mathbf{riro}\mathbf{Tan}[\theta]^2+\mathbf{ro}^2\mathbf{Tan}[\theta]^2}\right)\right)\right)\right)$$

$$\mathbf{distlargethetadown}[\mathbf{ro\_},\mathbf{ri\_},\mathbf{theta\_}]=2*\mathbf{distlargethetanoneck}[\mathbf{ro},\mathbf{ri},\mathbf{ro},\mathbf{rsdown}[\mathbf{ro},\mathbf{ri},\theta]]$$

$$2\left(-\mathbf{roEllipticE}\left[\tfrac{-\mathbf{ri}^2+\mathbf{ro}^2}{\mathbf{ro}^2}\right]-\right.$$
$$\mathbf{roEllipticE}\left[\mathbf{ArcSin}\left[\sqrt{2}\sqrt{\left(\left(\mathbf{ro}^2\left(-1-\mathbf{Tan}[\theta]^2\right)\left(-\mathbf{ri}^2+\tfrac{1}{2(-1-\mathbf{Tan}[\theta]^2)}\left(2\mathbf{riro}-\mathbf{ri}^2\mathbf{Tan}[\theta]^2-\mathbf{ro}^2\right.\right.\right.\right.\right.\right.$$
$$\left.\left.\left.\left.\left.\left.\mathbf{Tan}[\theta]^2+(\mathbf{ri}+\mathbf{ro})\mathbf{Tan}[\theta]\sqrt{-4\mathbf{riro}+\mathbf{ri}^2\mathbf{Tan}[\theta]^2-2\mathbf{riro}\mathbf{Tan}[\theta]^2+\mathbf{ro}^2\mathbf{Tan}[\theta]^2}\right)\right)\right)\Big/$$
$$\left(\left(-\mathbf{ri}^2+\mathbf{ro}^2\right)\left(2\mathbf{riro}-\mathbf{ri}^2\mathbf{Tan}[\theta]^2-\mathbf{ro}^2\mathbf{Tan}[\theta]^2+(\mathbf{ri}+\mathbf{ro})\mathbf{Tan}[\theta]\right.\right.$$
$$\left.\left.\sqrt{-4\mathbf{riro}+\mathbf{ri}^2\mathbf{Tan}[\theta]^2-2\mathbf{riro}\mathbf{Tan}[\theta]^2+\mathbf{ro}^2\mathbf{Tan}[\theta]^2}\right)\right)\Big],\tfrac{-\mathbf{ri}^2+\mathbf{ro}^2}{\mathbf{ro}^2}\Big]-$$
$$\mathbf{riEllipticF}\left[\mathbf{ArcSin}\left[\sqrt{2}\sqrt{\left(\left(\mathbf{ro}^2\left(-1-\mathbf{Tan}[\theta]^2\right)\left(-\mathbf{ri}^2+\tfrac{1}{2(-1-\mathbf{Tan}[\theta]^2)}\left(2\mathbf{riro}-\mathbf{ri}^2\mathbf{Tan}[\theta]^2-\mathbf{ro}^2\right.\right.\right.\right.\right.\right.$$
$$\left.\left.\left.\left.\left.\left.\mathbf{Tan}[\theta]^2+(\mathbf{ri}+\mathbf{ro})\mathbf{Tan}[\theta]\sqrt{-4\mathbf{riro}+\mathbf{ri}^2\mathbf{Tan}[\theta]^2-2\mathbf{riro}\mathbf{Tan}[\theta]^2+\mathbf{ro}^2\mathbf{Tan}[\theta]^2}\right)\right)\right)\Big/$$
$$\left(\left(-\mathbf{ri}^2+\mathbf{ro}^2\right)\left(2\mathbf{riro}-\mathbf{ri}^2\mathbf{Tan}[\theta]^2-\mathbf{ro}^2\mathbf{Tan}[\theta]^2+(\mathbf{ri}+\mathbf{ro})\mathbf{Tan}[\theta]\right.\right.$$
$$\left.\left.\sqrt{-4\mathbf{riro}+\mathbf{ri}^2\mathbf{Tan}[\theta]^2-2\mathbf{riro}\mathbf{Tan}[\theta]^2+\mathbf{ro}^2\mathbf{Tan}[\theta]^2}\right)\right)\Big],\tfrac{-\mathbf{ri}^2+\mathbf{ro}^2}{\mathbf{ro}^2}\Big]-$$
$$\mathbf{riEllipticK}\left[\tfrac{-\mathbf{ri}^2+\mathbf{ro}^2}{\mathbf{ro}^2}\right]+2\left(\mathbf{roEllipticE}\left[\tfrac{-\mathbf{ri}^2+\mathbf{ro}^2}{\mathbf{ro}^2}\right]+\mathbf{riEllipticK}\left[\tfrac{-\mathbf{ri}^2+\mathbf{ro}^2}{\mathbf{ro}^2}\right]\right)+$$
$$\left(\sqrt{2}\right.$$
$$\sqrt{\left(\left(\mathbf{ro}^2-\tfrac{1}{2(-1-\mathbf{Tan}[\theta]^2)}\left(2\mathbf{riro}-\mathbf{ri}^2\mathbf{Tan}[\theta]^2-\mathbf{ro}^2\mathbf{Tan}[\theta]^2+\right.\right.\right.}$$
$$\left.\left.\left.(\mathbf{ri}+\mathbf{ro})\mathbf{Tan}[\theta]\sqrt{-4\mathbf{riro}+\mathbf{ri}^2\mathbf{Tan}[\theta]^2-2\mathbf{riro}\mathbf{Tan}[\theta]^2+\mathbf{ro}^2\mathbf{Tan}[\theta]^2}\right)\right)$$
$$\left(-\mathbf{ri}^2+\tfrac{1}{2(-1-\mathbf{Tan}[\theta]^2)}\left(2\mathbf{riro}-\mathbf{ri}^2\mathbf{Tan}[\theta]^2-\mathbf{ro}^2\mathbf{Tan}[\theta]^2+(\mathbf{ri}+\mathbf{ro})\mathbf{Tan}[\theta]\right.\right.$$
$$\left.\left.\left.\sqrt{-4\mathbf{riro}+\mathbf{ri}^2\mathbf{Tan}[\theta]^2-2\mathbf{riro}\mathbf{Tan}[\theta]^2+\mathbf{ro}^2\mathbf{Tan}[\theta]^2}\right)\right)\right)\Big/$$
$$\left(\sqrt{\left(\tfrac{1}{-1-\mathbf{Tan}[\theta]^2}\left(2\mathbf{riro}-\mathbf{ri}^2\mathbf{Tan}[\theta]^2-\mathbf{ro}^2\mathbf{Tan}[\theta]^2+(\mathbf{ri}+\mathbf{ro})\mathbf{Tan}[\theta]\right.\right.\right.$$
$$\left.\left.\left.\sqrt{-4\mathbf{riro}+\mathbf{ri}^2\mathbf{Tan}[\theta]^2-2\mathbf{riro}\mathbf{Tan}[\theta]^2+\mathbf{ro}^2\mathbf{Tan}[\theta]^2}\right)\right)\right)\right)$$

$$\mathbf{vollargethetaup}[\mathbf{ro\_},\mathbf{ri\_},\mathbf{theta\_}]=2*\mathbf{vollargethetanoneck}[\mathbf{ro},\mathbf{ri},\mathbf{ro},\mathbf{rsup}[\mathbf{ro},\mathbf{ri},\theta]]$$

$$2\left(\frac{1}{3}\pi\left(\left(2\mathbf{ri}^2\mathbf{ro}+3\mathbf{riro}^2+2\mathbf{ro}^3\right)\mathbf{EllipticE}\left[\frac{-\mathbf{ri}^2+\mathbf{ro}^2}{\mathbf{ro}^2}\right]-\mathbf{ri}^2\mathbf{roEllipticK}\left[\frac{-\mathbf{ri}^2+\mathbf{ro}^2}{\mathbf{ro}^2}\right]\right)-\right.$$
$$\frac{1}{3}\pi\left(\left(2\mathbf{ri}^2\mathbf{ro}+3\mathbf{riro}^2+2\mathbf{ro}^3\right)\mathbf{EllipticE}[\right.$$
$$\mathbf{ArcSin}\left[\sqrt{2}\sqrt{\left(\left(\mathbf{ro}^2\left(-1-\mathbf{Tan}[\theta]^2\right)\left(-\mathbf{ri}^2+\frac{1}{2(-1-\mathbf{Tan}[\theta]^2)}\left(2\mathbf{riro}-\mathbf{ri}^2\mathbf{Tan}[\theta]^2-\mathbf{ro}^2\mathbf{Tan}[\theta]^2-\right.\right.\right.\right.\right.$$
$$\left.\left.\left.\left.\left.(\mathbf{ri}+\mathbf{ro})\mathbf{Tan}[\theta]\sqrt{-4\mathbf{riro}+\mathbf{ri}^2\mathbf{Tan}[\theta]^2-2\mathbf{riro}\mathbf{Tan}[\theta]^2+\mathbf{ro}^2\mathbf{Tan}[\theta]^2}\right)\right)\right)\right)\Big/$$
$$\left(\left(-\mathbf{ri}^2+\mathbf{ro}^2\right)\left(2\mathbf{riro}-\mathbf{ri}^2\mathbf{Tan}[\theta]^2-\mathbf{ro}^2\mathbf{Tan}[\theta]^2-(\mathbf{ri}+\mathbf{ro})\mathbf{Tan}[\theta]\right.\right.$$
$$\left.\left.\sqrt{-4\mathbf{riro}+\mathbf{ri}^2\mathbf{Tan}[\theta]^2-2\mathbf{riro}\mathbf{Tan}[\theta]^2+\mathbf{ro}^2\mathbf{Tan}[\theta]^2}\right)\right)\Big]\Big,\frac{-\mathbf{ri}^2+\mathbf{ro}^2}{\mathbf{ro}^2}\Big]-$$
$$\mathbf{ri}^2\mathbf{roEllipticF}\left[\mathbf{ArcSin}\left[\sqrt{2}\sqrt{\left(\left(\mathbf{ro}^2\left(-1-\mathbf{Tan}[\theta]^2\right)\left(-\mathbf{ri}^2+\frac{1}{2(-1-\mathbf{Tan}[\theta]^2)}\left(2\mathbf{riro}-\mathbf{ri}^2\mathbf{Tan}[\theta]^2-\mathbf{ro}^2\mathbf{Tan}[\right.\right.\right.\right.\right.\right.$$
$$\left.\left.\left.\left.\left.\theta]^2-(\mathbf{ri}+\mathbf{ro})\mathbf{Tan}[\theta]\sqrt{-4\mathbf{riro}+\mathbf{ri}^2\mathbf{Tan}[\theta]^2-2\mathbf{riro}\mathbf{Tan}[\theta]^2+\mathbf{ro}^2\mathbf{Tan}[\theta]^2}\right)\right)\right)\right)\Big/$$
$$\left(\left(-\mathbf{ri}^2+\mathbf{ro}^2\right)\left(2\mathbf{riro}-\mathbf{ri}^2\mathbf{Tan}[\theta]^2-\mathbf{ro}^2\mathbf{Tan}[\theta]^2-(\mathbf{ri}+\mathbf{ro})\mathbf{Tan}[\theta]\right.\right.$$
$$\left.\left.\sqrt{-4\mathbf{riro}+\mathbf{ri}^2\mathbf{Tan}[\theta]^2-2\mathbf{riro}\mathbf{Tan}[\theta]^2+\mathbf{ro}^2\mathbf{Tan}[\theta]^2}\right)\right)\Big]\Big,\frac{-\mathbf{ri}^2+\mathbf{ro}^2}{\mathbf{ro}^2}\Big]-$$
$$\left(\sqrt{2}\sqrt{\left(\left(\mathbf{ro}^2-\frac{1}{2(-1-\mathbf{Tan}[\theta]^2)}\left(2\mathbf{riro}-\mathbf{ri}^2\mathbf{Tan}[\theta]^2-\mathbf{ro}^2\mathbf{Tan}[\theta]^2-(\mathbf{ri}+\mathbf{ro})\mathbf{Tan}[\theta]\right.\right.\right.\right.$$
$$\left.\left.\left.\left.\sqrt{-4\mathbf{riro}+\mathbf{ri}^2\mathbf{Tan}[\theta]^2-2\mathbf{riro}\mathbf{Tan}[\theta]^2+\mathbf{ro}^2\mathbf{Tan}[\theta]^2}\right)\right)\right)$$
$$\left(-\mathbf{ri}^2+\frac{1}{2(-1-\mathbf{Tan}[\theta]^2)}\left(2\mathbf{riro}-\mathbf{ri}^2\mathbf{Tan}[\theta]^2-\mathbf{ro}^2\mathbf{Tan}[\theta]^2-(\mathbf{ri}+\mathbf{ro})\mathbf{Tan}[\theta]\right.\right.$$
$$\left.\left.\sqrt{-4\mathbf{riro}+\mathbf{ri}^2\mathbf{Tan}[\theta]^2-2\mathbf{riro}\mathbf{Tan}[\theta]^2+\mathbf{ro}^2\mathbf{Tan}[\theta]^2}\right)\right)\Big)$$
$$\left(2\mathbf{ri}^2+3\mathbf{riro}+2\mathbf{ro}^2+\frac{1}{2(-1-\mathbf{Tan}[\theta]^2)}\left(2\mathbf{riro}-\mathbf{ri}^2\mathbf{Tan}[\theta]^2-\mathbf{ro}^2\mathbf{Tan}[\theta]^2-\right.\right.$$
$$\left.\left.(\mathbf{ri}+\mathbf{ro})\mathbf{Tan}[\theta]\sqrt{-4\mathbf{riro}+\mathbf{ri}^2\mathbf{Tan}[\theta]^2-2\mathbf{riro}\mathbf{Tan}[\theta]^2+\mathbf{ro}^2\mathbf{Tan}[\theta]^2}\right)\right)\Big/$$
$$\left(\sqrt{\left(\frac{1}{-1-\mathbf{Tan}[\theta]^2}\left(2\mathbf{riro}-\mathbf{ri}^2\mathbf{Tan}[\theta]^2-\mathbf{ro}^2\mathbf{Tan}[\theta]^2-(\mathbf{ri}+\mathbf{ro})\mathbf{Tan}[\theta]\right.\right.\right.$$
$$\left.\left.\left.\sqrt{-4\mathbf{riro}+\mathbf{ri}^2\mathbf{Tan}[\theta]^2-2\mathbf{riro}\mathbf{Tan}[\theta]^2+\mathbf{ro}^2\mathbf{Tan}[\theta]^2}\right)\right)}\right)\Big)\Big)$$

$$\mathbf{vollargethetadown[ro\_, ri\_, theta\_] = 2 * vollargethetanoneck[ro, ri, ro, rsdown[ro, ri, \theta]]}$$

$$2\left(\frac{1}{3}\pi\left(\left(2\mathbf{ri}^2\mathbf{ro}+3\mathbf{riro}^2+2\mathbf{ro}^3\right)\mathbf{EllipticE}\left[\frac{-\mathbf{ri}^2+\mathbf{ro}^2}{\mathbf{ro}^2}\right]-\mathbf{ri}^2\mathbf{roEllipticK}\left[\frac{-\mathbf{ri}^2+\mathbf{ro}^2}{\mathbf{ro}^2}\right]\right)-\right.$$
$$\frac{1}{3}\pi\left(\left(2\mathbf{ri}^2\mathbf{ro}+3\mathbf{riro}^2+2\mathbf{ro}^3\right)\mathbf{EllipticE}[\right.$$
$$\mathbf{ArcSin}\left[\sqrt{2}\sqrt{\left(\left(\mathbf{ro}^2\left(-1-\mathbf{Tan}[\theta]^2\right)\left(-\mathbf{ri}^2+\frac{1}{2(-1-\mathbf{Tan}[\theta]^2)}\left(2\mathbf{riro}-\mathbf{ri}^2\mathbf{Tan}[\theta]^2-\mathbf{ro}^2\mathbf{Tan}[\theta]^2+\right.\right.\right.\right.\right.$$
$$\left.\left.\left.\left.\left.(\mathbf{ri}+\mathbf{ro})\mathbf{Tan}[\theta]\sqrt{-4\mathbf{riro}+\mathbf{ri}^2\mathbf{Tan}[\theta]^2-2\mathbf{riro}\mathbf{Tan}[\theta]^2+\mathbf{ro}^2\mathbf{Tan}[\theta]^2}\right)\right)\right)\right)\Big/$$
$$\left(\left(-\mathbf{ri}^2+\mathbf{ro}^2\right)\left(2\mathbf{riro}-\mathbf{ri}^2\mathbf{Tan}[\theta]^2-\mathbf{ro}^2\mathbf{Tan}[\theta]^2+(\mathbf{ri}+\mathbf{ro})\mathbf{Tan}[\theta]\right.\right.$$
$$\left.\left.\sqrt{-4\mathbf{riro}+\mathbf{ri}^2\mathbf{Tan}[\theta]^2-2\mathbf{riro}\mathbf{Tan}[\theta]^2+\mathbf{ro}^2\mathbf{Tan}[\theta]^2}\right)\right)\Big]\Big,\frac{-\mathbf{ri}^2+\mathbf{ro}^2}{\mathbf{ro}^2}\Big]-$$
$$\mathbf{ri}^2\mathbf{roEllipticF}\left[\mathbf{ArcSin}\left[\sqrt{2}\sqrt{\left(\left(\mathbf{ro}^2\left(-1-\mathbf{Tan}[\theta]^2\right)\left(-\mathbf{ri}^2+\frac{1}{2(-1-\mathbf{Tan}[\theta]^2)}\left(2\mathbf{riro}-\mathbf{ri}^2\mathbf{Tan}[\theta]^2-\mathbf{ro}^2\mathbf{Tan}[\right.\right.\right.\right.\right.\right.$$
$$\left.\left.\left.\left.\left.\theta]^2+(\mathbf{ri}+\mathbf{ro})\mathbf{Tan}[\theta]\sqrt{-4\mathbf{riro}+\mathbf{ri}^2\mathbf{Tan}[\theta]^2-2\mathbf{riro}\mathbf{Tan}[\theta]^2+\mathbf{ro}^2\mathbf{Tan}[\theta]^2}\right)\right)\right)\right)\Big/$$
$$\left(\left(-\mathbf{ri}^2+\mathbf{ro}^2\right)\left(2\mathbf{riro}-\mathbf{ri}^2\mathbf{Tan}[\theta]^2-\mathbf{ro}^2\mathbf{Tan}[\theta]^2+(\mathbf{ri}+\mathbf{ro})\mathbf{Tan}[\theta]\right.\right.$$
$$\left.\left.\sqrt{-4\mathbf{riro}+\mathbf{ri}^2\mathbf{Tan}[\theta]^2-2\mathbf{riro}\mathbf{Tan}[\theta]^2+\mathbf{ro}^2\mathbf{Tan}[\theta]^2}\right)\right)\Big]\Big,\frac{-\mathbf{ri}^2+\mathbf{ro}^2}{\mathbf{ro}^2}\Big]-$$

$$\left(\sqrt{2}\sqrt{}\left(\left(\mathbf{ro}^2-\frac{1}{2(-1-\mathbf{Tan}[\theta]^2)}\left(2\mathbf{riro}-\mathbf{ri}^2\mathbf{Tan}[\theta]^2-\mathbf{ro}^2\mathbf{Tan}[\theta]^2+(\mathbf{ri}+\mathbf{ro})\mathbf{Tan}[\theta]\right.\right.\right.\right.$$

$$\left.\left.\sqrt{-4\mathbf{riro}+\mathbf{ri}^2\mathbf{Tan}[\theta]^2-2\mathbf{riroTan}[\theta]^2+\mathbf{ro}^2\mathbf{Tan}[\theta]^2}\right)\right)$$

$$\left(-\mathbf{ri}^2+\frac{1}{2(-1-\mathbf{Tan}[\theta]^2)}\left(2\mathbf{riro}-\mathbf{ri}^2\mathbf{Tan}[\theta]^2-\mathbf{ro}^2\mathbf{Tan}[\theta]^2+(\mathbf{ri}+\mathbf{ro})\mathbf{Tan}[\theta]\right.\right.$$

$$\left.\left.\left.\sqrt{-4\mathbf{riro}+\mathbf{ri}^2\mathbf{Tan}[\theta]^2-2\mathbf{riroTan}[\theta]^2+\mathbf{ro}^2\mathbf{Tan}[\theta]^2}\right)\right)\right)$$

$$\left(2\mathbf{ri}^2+3\mathbf{riro}+2\mathbf{ro}^2+\frac{1}{2(-1-\mathbf{Tan}[\theta]^2)}\left(2\mathbf{riro}-\mathbf{ri}^2\mathbf{Tan}[\theta]^2-\mathbf{ro}^2\mathbf{Tan}[\theta]^2+\right.\right.$$

$$\left.\left.\left.(\mathbf{ri}+\mathbf{ro})\mathbf{Tan}[\theta]\sqrt{-4\mathbf{riro}+\mathbf{ri}^2\mathbf{Tan}[\theta]^2-2\mathbf{riroTan}[\theta]^2+\mathbf{ro}^2\mathbf{Tan}[\theta]^2}\right)\right)\right)\Big/$$

$$\left(\sqrt{}\left(\frac{1}{-1-\mathbf{Tan}[\theta]^2}\left(2\mathbf{riro}-\mathbf{ri}^2\mathbf{Tan}[\theta]^2-\mathbf{ro}^2\mathbf{Tan}[\theta]^2+(\mathbf{ri}+\mathbf{ro})\mathbf{Tan}[\theta]\right.\right.\right.$$

$$\left.\left.\left.\sqrt{-4\mathbf{riro}+\mathbf{ri}^2\mathbf{Tan}[\theta]^2-2\mathbf{riroTan}[\theta]^2+\mathbf{ro}^2\mathbf{Tan}[\theta]^2}\right)\right)\right)\Big)\Big)$$

**resdistlargethetaup[ro_, ri_, theta_] =**

**(3 * vollargethetaup[ro, ri, *θ*]/(4 * Pi))^(−1/3) * distlargethetaup[ro, ri, *θ*]**

$$\left(2\left(\frac{2\pi}{3}\right)^{1/3}\left(-\mathbf{roEllipticE}\left[\frac{-\mathbf{ri}^2+\mathbf{ro}^2}{\mathbf{ro}^2}\right]-\right.\right.$$

$$\mathbf{roEllipticE}\Big[\mathbf{ArcSin}\Big[\sqrt{2}\sqrt{}\Big(\Big(\mathbf{ro}^2\left(-1-\mathbf{Tan}[\theta]^2\right)\Big(-\mathbf{ri}^2+\frac{1}{2(-1-\mathbf{Tan}[\theta]^2)}\Big(2\mathbf{riro}-\mathbf{ri}^2\mathbf{Tan}[\theta]^2-\mathbf{ro}^2$$

$$\mathbf{Tan}[\theta]^2-(\mathbf{ri}+\mathbf{ro})\mathbf{Tan}[\theta]\sqrt{-4\mathbf{riro}+\mathbf{ri}^2\mathbf{Tan}[\theta]^2-2\mathbf{riroTan}[\theta]^2+\mathbf{ro}^2\mathbf{Tan}[\theta]^2}\Big)\Big)\Big)\Big/$$

$$\left(\left(-\mathbf{ri}^2+\mathbf{ro}^2\right)\left(2\mathbf{riro}-\mathbf{ri}^2\mathbf{Tan}[\theta]^2-\mathbf{ro}^2\mathbf{Tan}[\theta]^2-(\mathbf{ri}+\mathbf{ro})\mathbf{Tan}[\theta]\right.\right.$$

$$\left.\left.\sqrt{-4\mathbf{riro}+\mathbf{ri}^2\mathbf{Tan}[\theta]^2-2\mathbf{riroTan}[\theta]^2+\mathbf{ro}^2\mathbf{Tan}[\theta]^2}\right)\right)\Big)\Big],\frac{-\mathbf{ri}^2+\mathbf{ro}^2}{\mathbf{ro}^2}\Big]-$$

$$\mathbf{riEllipticF}\Big[\mathbf{ArcSin}\Big[\sqrt{2}\sqrt{}\Big(\Big(\mathbf{ro}^2\left(-1-\mathbf{Tan}[\theta]^2\right)\Big(-\mathbf{ri}^2+\frac{1}{2(-1-\mathbf{Tan}[\theta]^2)}\Big(2\mathbf{riro}-\mathbf{ri}^2\mathbf{Tan}[\theta]^2-\mathbf{ro}^2$$

$$\mathbf{Tan}[\theta]^2-(\mathbf{ri}+\mathbf{ro})\mathbf{Tan}[\theta]\sqrt{-4\mathbf{riro}+\mathbf{ri}^2\mathbf{Tan}[\theta]^2-2\mathbf{riroTan}[\theta]^2+\mathbf{ro}^2\mathbf{Tan}[\theta]^2}\Big)\Big)\Big)\Big/$$

$$\left(\left(-\mathbf{ri}^2+\mathbf{ro}^2\right)\left(2\mathbf{riro}-\mathbf{ri}^2\mathbf{Tan}[\theta]^2-\mathbf{ro}^2\mathbf{Tan}[\theta]^2-(\mathbf{ri}+\mathbf{ro})\mathbf{Tan}[\theta]\right.\right.$$

$$\left.\left.\sqrt{-4\mathbf{riro}+\mathbf{ri}^2\mathbf{Tan}[\theta]^2-2\mathbf{riroTan}[\theta]^2+\mathbf{ro}^2\mathbf{Tan}[\theta]^2}\right)\right)\Big)\Big],\frac{-\mathbf{ri}^2+\mathbf{ro}^2}{\mathbf{ro}^2}\Big]-$$

$$\mathbf{riEllipticK}\left[\frac{-\mathbf{ri}^2+\mathbf{ro}^2}{\mathbf{ro}^2}\right]+2\left(\mathbf{roEllipticE}\left[\frac{-\mathbf{ri}^2+\mathbf{ro}^2}{\mathbf{ro}^2}\right]+\mathbf{riEllipticK}\left[\frac{-\mathbf{ri}^2+\mathbf{ro}^2}{\mathbf{ro}^2}\right]\right)+$$

$$\left(\sqrt{2}\sqrt{}\left(\left(\mathbf{ro}^2-\frac{1}{2(-1-\mathbf{Tan}[\theta]^2)}\left(2\mathbf{riro}-\mathbf{ri}^2\mathbf{Tan}[\theta]^2-\mathbf{ro}^2\mathbf{Tan}[\theta]^2-\right.\right.\right.\right.$$

$$\left.\left.(\mathbf{ri}+\mathbf{ro})\mathbf{Tan}[\theta]\sqrt{-4\mathbf{riro}+\mathbf{ri}^2\mathbf{Tan}[\theta]^2-2\mathbf{riroTan}[\theta]^2+\mathbf{ro}^2\mathbf{Tan}[\theta]^2}\right)\right)$$

$$\left(-\mathbf{ri}^2+\frac{1}{2(-1-\mathbf{Tan}[\theta]^2)}\left(2\mathbf{riro}-\mathbf{ri}^2\mathbf{Tan}[\theta]^2-\mathbf{ro}^2\mathbf{Tan}[\theta]^2-(\mathbf{ri}+\mathbf{ro})\mathbf{Tan}[\theta]\right.\right.$$

$$\left.\left.\sqrt{-4\mathbf{riro}+\mathbf{ri}^2\mathbf{Tan}[\theta]^2-2\mathbf{riroTan}[\theta]^2+\mathbf{ro}^2\mathbf{Tan}[\theta]^2}\right)\right)\Big)\Big)\Big/$$

$$\left(\sqrt{}\left(\frac{1}{-1-\mathbf{Tan}[\theta]^2}\left(2\mathbf{riro}-\mathbf{ri}^2\mathbf{Tan}[\theta]^2-\mathbf{ro}^2\mathbf{Tan}[\theta]^2-(\mathbf{ri}+\mathbf{ro})\mathbf{Tan}[\theta]\right.\right.\right.$$

$$\left.\left.\left.\sqrt{-4\mathbf{riro}+\mathbf{ri}^2\mathbf{Tan}[\theta]^2-2\mathbf{riroTan}[\theta]^2+\mathbf{ro}^2\mathbf{Tan}[\theta]^2}\right)\right)\right)\Big)\Big)\Big/$$

$$\left(\frac{1}{3}\pi\left(\left(2\mathbf{ri}^2\mathbf{ro}+3\mathbf{riro}^2+2\mathbf{ro}^3\right)\mathbf{EllipticE}\left[\frac{-\mathbf{ri}^2+\mathbf{ro}^2}{\mathbf{ro}^2}\right]-\mathbf{ri}^2\mathbf{roEllipticK}\left[\frac{-\mathbf{ri}^2+\mathbf{ro}^2}{\mathbf{ro}^2}\right]\right)-\right.$$

$$\frac{1}{3}$$

$$\pi$$

$$\left(\left(2\mathbf{ri}^2\mathbf{ro}+3\mathbf{riro}^2+2\mathbf{ro}^3\right)\mathbf{EllipticE}\left[\right.\right.$$

$$\mathbf{ArcSin}\left[\sqrt{2}\sqrt{\left(\left(\mathbf{ro}^2\left(-1-\mathbf{Tan}[\theta]^2\right)\left(-\mathbf{ri}^2+\frac{1}{2(-1-\mathbf{Tan}[\theta]^2)}\left(2\mathbf{riro}-\mathbf{ri}^2\mathbf{Tan}[\theta]^2-\mathbf{ro}^2\mathbf{Tan}[\theta]^2-\right.\right.\right.\right.\right.$$

$$\left.\left.\left.\left.\left.(\mathbf{ri}+\mathbf{ro})\mathbf{Tan}[\theta]\sqrt{-4\mathbf{riro}+\mathbf{ri}^2\mathbf{Tan}[\theta]^2-2\mathbf{riro}\mathbf{Tan}[\theta]^2+\mathbf{ro}^2\mathbf{Tan}[\theta]^2}\right)\right)\right)\right/$$

$$\left(\left(-\mathbf{ri}^2+\mathbf{ro}^2\right)\left(2\mathbf{riro}-\mathbf{ri}^2\mathbf{Tan}[\theta]^2-\mathbf{ro}^2\mathbf{Tan}[\theta]^2-(\mathbf{ri}+\mathbf{ro})\mathbf{Tan}[\theta]\right.\right.$$

$$\left.\left.\left.\sqrt{-4\mathbf{riro}+\mathbf{ri}^2\mathbf{Tan}[\theta]^2-2\mathbf{riro}\mathbf{Tan}[\theta]^2+\mathbf{ro}^2\mathbf{Tan}[\theta]^2}\right)\right)\right)\left.\right],\frac{-\mathbf{ri}^2+\mathbf{ro}^2}{\mathbf{ro}^2}\left.\right]-\mathbf{ri}^2\mathbf{roEllipticF}\left[\right.$$

$$\mathbf{ArcSin}\left[\sqrt{2}\sqrt{\left(\left(\mathbf{ro}^2\left(-1-\mathbf{Tan}[\theta]^2\right)\left(-\mathbf{ri}^2+\frac{1}{2(-1-\mathbf{Tan}[\theta]^2)}\left(2\mathbf{riro}-\mathbf{ri}^2\mathbf{Tan}[\theta]^2-\mathbf{ro}^2\mathbf{Tan}[\theta]^2-\right.\right.\right.\right.\right.$$

$$\left.\left.\left.\left.\left.(\mathbf{ri}+\mathbf{ro})\mathbf{Tan}[\theta]\sqrt{-4\mathbf{riro}+\mathbf{ri}^2\mathbf{Tan}[\theta]^2-2\mathbf{riro}\mathbf{Tan}[\theta]^2+\mathbf{ro}^2\mathbf{Tan}[\theta]^2}\right)\right)\right)\right/$$

$$\left(\left(-\mathbf{ri}^2+\mathbf{ro}^2\right)\left(2\mathbf{riro}-\mathbf{ri}^2\mathbf{Tan}[\theta]^2-\mathbf{ro}^2\mathbf{Tan}[\theta]^2-(\mathbf{ri}+\mathbf{ro})\mathbf{Tan}[\theta]\right.\right.$$

$$\left.\left.\left.\sqrt{-4\mathbf{riro}+\mathbf{ri}^2\mathbf{Tan}[\theta]^2-2\mathbf{riro}\mathbf{Tan}[\theta]^2+\mathbf{ro}^2\mathbf{Tan}[\theta]^2}\right)\right)\right)\left.\right],\frac{-\mathbf{ri}^2+\mathbf{ro}^2}{\mathbf{ro}^2}\left.\right]-$$

$$\left(\sqrt{2}\sqrt{\left(\left(\mathbf{ro}^2-\frac{1}{2(-1-\mathbf{Tan}[\theta]^2)}\left(2\mathbf{riro}-\mathbf{ri}^2\mathbf{Tan}[\theta]^2-\mathbf{ro}^2\mathbf{Tan}[\theta]^2-(\mathbf{ri}+\mathbf{ro})\mathbf{Tan}[\theta]\right.\right.\right.\right.$$

$$\left.\left.\left.\left.\sqrt{-4\mathbf{riro}+\mathbf{ri}^2\mathbf{Tan}[\theta]^2-2\mathbf{riro}\mathbf{Tan}[\theta]^2+\mathbf{ro}^2\mathbf{Tan}[\theta]^2}\right)\right)\right)$$

$$\left(-\mathbf{ri}^2+\frac{1}{2(-1-\mathbf{Tan}[\theta]^2)}\left(2\mathbf{riro}-\mathbf{ri}^2\mathbf{Tan}[\theta]^2-\mathbf{ro}^2\mathbf{Tan}[\theta]^2-(\mathbf{ri}+\mathbf{ro})\mathbf{Tan}[\theta]\right.\right.$$

$$\left.\left.\left.\sqrt{-4\mathbf{riro}+\mathbf{ri}^2\mathbf{Tan}[\theta]^2-2\mathbf{riro}\mathbf{Tan}[\theta]^2+\mathbf{ro}^2\mathbf{Tan}[\theta]^2}\right)\right)\right)$$

$$\left(2\mathbf{ri}^2+3\mathbf{riro}+2\mathbf{ro}^2+\frac{1}{2(-1-\mathbf{Tan}[\theta]^2)}\left(2\mathbf{riro}-\mathbf{ri}^2\mathbf{Tan}[\theta]^2-\mathbf{ro}^2\mathbf{Tan}[\theta]^2-\right.\right.$$

$$\left.\left.\left.(\mathbf{ri}+\mathbf{ro})\mathbf{Tan}[\theta]\sqrt{-4\mathbf{riro}+\mathbf{ri}^2\mathbf{Tan}[\theta]^2-2\mathbf{riro}\mathbf{Tan}[\theta]^2+\mathbf{ro}^2\mathbf{Tan}[\theta]^2}\right)\right)\right)\Big/$$

$$\left(\sqrt{\left(\frac{1}{-1-\mathbf{Tan}[\theta]^2}\left(2\mathbf{riro}-\mathbf{ri}^2\mathbf{Tan}[\theta]^2-\mathbf{ro}^2\mathbf{Tan}[\theta]^2-(\mathbf{ri}+\mathbf{ro})\mathbf{Tan}[\theta]\right.\right.\right.$$

$$\left.\left.\left.\sqrt{-4\mathbf{riro}+\mathbf{ri}^2\mathbf{Tan}[\theta]^2-2\mathbf{riro}\mathbf{Tan}[\theta]^2+\mathbf{ro}^2\mathbf{Tan}[\theta]^2}\right)\right)}\right)\Big)\Big)\Big)\Big)^{1/3}$$

$$\mathbf{resdistlargethetadown[ro\_,ri\_,theta\_]=}$$

$$\mathbf{(3*vollargethetadown[ro,ri,\theta]/(4*Pi))\text{\^{}}(-1/3)*distlargethetadown[ro,ri,\theta]}$$

$$\left(2\left(\frac{2\pi}{3}\right)^{1/3}\left(-\mathbf{roEllipticE}\left[\frac{-\mathbf{ri}^2+\mathbf{ro}^2}{\mathbf{ro}^2}\right]-\right.\right.$$

$$\mathbf{roEllipticE}\left[\mathbf{ArcSin}\left[\sqrt{2}\sqrt{\left(\left(\mathbf{ro}^2\left(-1-\mathbf{Tan}[\theta]^2\right)\left(-\mathbf{ri}^2+\frac{1}{2(-1-\mathbf{Tan}[\theta]^2)}\left(2\mathbf{riro}-\mathbf{ri}^2\mathbf{Tan}[\theta]^2-\mathbf{ro}^2\right.\right.\right.\right.\right.\right.$$

$$\left.\left.\left.\left.\left.\left.\mathbf{Tan}[\theta]^2+(\mathbf{ri}+\mathbf{ro})\mathbf{Tan}[\theta]\sqrt{-4\mathbf{riro}+\mathbf{ri}^2\mathbf{Tan}[\theta]^2-2\mathbf{riro}\mathbf{Tan}[\theta]^2+\mathbf{ro}^2\mathbf{Tan}[\theta]^2}\right)\right)\right)\right/$$

$$\left(\left(-\mathbf{ri}^2+\mathbf{ro}^2\right)\left(2\mathbf{riro}-\mathbf{ri}^2\mathbf{Tan}[\theta]^2-\mathbf{ro}^2\mathbf{Tan}[\theta]^2+(\mathbf{ri}+\mathbf{ro})\mathbf{Tan}[\theta]\right.\right.$$

$$\left.\left.\left.\sqrt{-4\mathbf{riro}+\mathbf{ri}^2\mathbf{Tan}[\theta]^2-2\mathbf{riro}\mathbf{Tan}[\theta]^2+\mathbf{ro}^2\mathbf{Tan}[\theta]^2}\right)\right)\right)\left.\right],\frac{-\mathbf{ri}^2+\mathbf{ro}^2}{\mathbf{ro}^2}\left.\right]-$$

$$\mathbf{riEllipticF}\left[\mathbf{ArcSin}\left[\sqrt{2}\sqrt{\left(\left(\mathbf{ro}^2\left(-1-\mathbf{Tan}[\theta]^2\right)\left(-\mathbf{ri}^2+\frac{1}{2(-1-\mathbf{Tan}[\theta]^2)}\left(2\mathbf{riro}-\mathbf{ri}^2\mathbf{Tan}[\theta]^2-\mathbf{ro}^2\right.\right.\right.\right.\right.\right.$$

$$\left.\left.\left.\left.\left.\left.\mathbf{Tan}[\theta]^2+(\mathbf{ri}+\mathbf{ro})\mathbf{Tan}[\theta]\sqrt{-4\mathbf{riro}+\mathbf{ri}^2\mathbf{Tan}[\theta]^2-2\mathbf{riro}\mathbf{Tan}[\theta]^2+\mathbf{ro}^2\mathbf{Tan}[\theta]^2}\right)\right)\right)\right/$$

$$\left(\left(-\mathbf{ri}^2+\mathbf{ro}^2\right)\left(2\mathbf{riro}-\mathbf{ri}^2\mathbf{Tan}[\theta]^2-\mathbf{ro}^2\mathbf{Tan}[\theta]^2+(\mathbf{ri}+\mathbf{ro})\mathbf{Tan}[\theta]\right.\right.$$

$$\left.\left.\left.\sqrt{-4\mathbf{riro}+\mathbf{ri}^2\mathbf{Tan}[\theta]^2-2\mathbf{riro}\mathbf{Tan}[\theta]^2+\mathbf{ro}^2\mathbf{Tan}[\theta]^2}\right)\right)\right)\left.\right],\frac{-\mathbf{ri}^2+\mathbf{ro}^2}{\mathbf{ro}^2}\left.\right]-$$

$$\mathbf{riEllipticK}\left[\frac{-\mathbf{ri}^2+\mathbf{ro}^2}{\mathbf{ro}^2}\right]+2\left(\mathbf{roEllipticE}\left[\frac{-\mathbf{ri}^2+\mathbf{ro}^2}{\mathbf{ro}^2}\right]+\mathbf{riEllipticK}\left[\frac{-\mathbf{ri}^2+\mathbf{ro}^2}{\mathbf{ro}^2}\right]\right)+$$
$$\left(\sqrt{2}\sqrt{\left(\left(\mathbf{ro}^2-\frac{1}{2(-1-\mathbf{Tan}[\theta]^2)}\left(2\mathbf{riro}-\mathbf{ri}^2\mathbf{Tan}[\theta]^2-\mathbf{ro}^2\mathbf{Tan}[\theta]^2+\right.\right.\right.\right.$$
$$\left.\left.\left.\left.(\mathbf{ri}+\mathbf{ro})\mathbf{Tan}[\theta]\sqrt{-4\mathbf{riro}+\mathbf{ri}^2\mathbf{Tan}[\theta]^2-2\mathbf{riro}\mathbf{Tan}[\theta]^2+\mathbf{ro}^2\mathbf{Tan}[\theta]^2}\right)\right)\right.$$
$$\left.\left(-\mathbf{ri}^2+\frac{1}{2(-1-\mathbf{Tan}[\theta]^2)}\left(2\mathbf{riro}-\mathbf{ri}^2\mathbf{Tan}[\theta]^2-\mathbf{ro}^2\mathbf{Tan}[\theta]^2+(\mathbf{ri}+\mathbf{ro})\mathbf{Tan}[\theta]\right.\right.\right.$$
$$\left.\left.\left.\left.\sqrt{-4\mathbf{riro}+\mathbf{ri}^2\mathbf{Tan}[\theta]^2-2\mathbf{riro}\mathbf{Tan}[\theta]^2+\mathbf{ro}^2\mathbf{Tan}[\theta]^2}\right)\right)\right)\right)\Big/$$
$$\left(\sqrt{\left(\frac{1}{-1-\mathbf{Tan}[\theta]^2}\left(2\mathbf{riro}-\mathbf{ri}^2\mathbf{Tan}[\theta]^2-\mathbf{ro}^2\mathbf{Tan}[\theta]^2+(\mathbf{ri}+\mathbf{ro})\mathbf{Tan}[\theta]\right.\right.\right.$$
$$\left.\left.\left.\left.\sqrt{-4\mathbf{riro}+\mathbf{ri}^2\mathbf{Tan}[\theta]^2-2\mathbf{riro}\mathbf{Tan}[\theta]^2+\mathbf{ro}^2\mathbf{Tan}[\theta]^2}\right)\right)\right)\right)\Big/$$
$$\left(\frac{1}{3}\pi\left(\left(2\mathbf{ri}^2\mathbf{ro}+3\mathbf{riro}^2+2\mathbf{ro}^3\right)\mathbf{EllipticE}\left[\frac{-\mathbf{ri}^2+\mathbf{ro}^2}{\mathbf{ro}^2}\right]-\mathbf{ri}^2\mathbf{roEllipticK}\left[\frac{-\mathbf{ri}^2+\mathbf{ro}^2}{\mathbf{ro}^2}\right]\right)-\right.$$
$$\frac{1}{3}$$
$$\pi$$
$$\left(\left(2\mathbf{ri}^2\mathbf{ro}+3\mathbf{riro}^2+2\mathbf{ro}^3\right)\mathbf{EllipticE}[\right.$$
$$\mathbf{ArcSin}\left[\sqrt{2}\sqrt{\left(\left(\mathbf{ro}^2\left(-1-\mathbf{Tan}[\theta]^2\right)\left(-\mathbf{ri}^2+\frac{1}{2(-1-\mathbf{Tan}[\theta]^2)}\left(2\mathbf{riro}-\mathbf{ri}^2\mathbf{Tan}[\theta]^2-\mathbf{ro}^2\mathbf{Tan}[\theta]^2+\right.\right.\right.\right.\right.$$
$$\left.\left.\left.\left.\left.(\mathbf{ri}+\mathbf{ro})\mathbf{Tan}[\theta]\sqrt{-4\mathbf{riro}+\mathbf{ri}^2\mathbf{Tan}[\theta]^2-2\mathbf{riro}\mathbf{Tan}[\theta]^2+\mathbf{ro}^2\mathbf{Tan}[\theta]^2}\right)\right)\right)\Big/\right.$$
$$\left.\left.\left.\left.\left.\left(\left(-\mathbf{ri}^2+\mathbf{ro}^2\right)\left(2\mathbf{riro}-\mathbf{ri}^2\mathbf{Tan}[\theta]^2-\mathbf{ro}^2\mathbf{Tan}[\theta]^2+(\mathbf{ri}+\mathbf{ro})\mathbf{Tan}[\theta]\right.\right.\right.\right.\right.\right.$$
$$\left.\left.\left.\left.\left.\left.\sqrt{-4\mathbf{riro}+\mathbf{ri}^2\mathbf{Tan}[\theta]^2-2\mathbf{riro}\mathbf{Tan}[\theta]^2+\mathbf{ro}^2\mathbf{Tan}[\theta]^2}\right)\right)\right)\right)\right],\frac{-\mathbf{ri}^2+\mathbf{ro}^2}{\mathbf{ro}^2}\right]-\mathbf{ri}^2\mathbf{roEllipticF}[$$
$$\mathbf{ArcSin}\left[\sqrt{2}\sqrt{\left(\left(\mathbf{ro}^2\left(-1-\mathbf{Tan}[\theta]^2\right)\left(-\mathbf{ri}^2+\frac{1}{2(-1-\mathbf{Tan}[\theta]^2)}\left(2\mathbf{riro}-\mathbf{ri}^2\mathbf{Tan}[\theta]^2-\mathbf{ro}^2\mathbf{Tan}[\theta]^2+\right.\right.\right.\right.\right.$$
$$\left.\left.\left.\left.\left.(\mathbf{ri}+\mathbf{ro})\mathbf{Tan}[\theta]\sqrt{-4\mathbf{riro}+\mathbf{ri}^2\mathbf{Tan}[\theta]^2-2\mathbf{riro}\mathbf{Tan}[\theta]^2+\mathbf{ro}^2\mathbf{Tan}[\theta]^2}\right)\right)\right)\Big/\right.$$
$$\left.\left.\left.\left.\left.\left(\left(-\mathbf{ri}^2+\mathbf{ro}^2\right)\left(2\mathbf{riro}-\mathbf{ri}^2\mathbf{Tan}[\theta]^2-\mathbf{ro}^2\mathbf{Tan}[\theta]^2+(\mathbf{ri}+\mathbf{ro})\mathbf{Tan}[\theta]\right.\right.\right.\right.\right.\right.$$
$$\left.\left.\left.\left.\left.\left.\sqrt{-4\mathbf{riro}+\mathbf{ri}^2\mathbf{Tan}[\theta]^2-2\mathbf{riro}\mathbf{Tan}[\theta]^2+\mathbf{ro}^2\mathbf{Tan}[\theta]^2}\right)\right)\right)\right)\right],\frac{-\mathbf{ri}^2+\mathbf{ro}^2}{\mathbf{ro}^2}\right]-$$
$$\left(\sqrt{2}\sqrt{\left(\left(\mathbf{ro}^2-\frac{1}{2(-1-\mathbf{Tan}[\theta]^2)}\left(2\mathbf{riro}-\mathbf{ri}^2\mathbf{Tan}[\theta]^2-\mathbf{ro}^2\mathbf{Tan}[\theta]^2+(\mathbf{ri}+\mathbf{ro})\mathbf{Tan}[\theta]\right.\right.\right.\right.$$
$$\left.\left.\left.\left.\sqrt{-4\mathbf{riro}+\mathbf{ri}^2\mathbf{Tan}[\theta]^2-2\mathbf{riro}\mathbf{Tan}[\theta]^2+\mathbf{ro}^2\mathbf{Tan}[\theta]^2}\right)\right)\right)$$
$$\left.\left(-\mathbf{ri}^2+\frac{1}{2(-1-\mathbf{Tan}[\theta]^2)}\left(2\mathbf{riro}-\mathbf{ri}^2\mathbf{Tan}[\theta]^2-\mathbf{ro}^2\mathbf{Tan}[\theta]^2+(\mathbf{ri}+\mathbf{ro})\mathbf{Tan}[\theta]\right.\right.\right.$$
$$\left.\left.\left.\sqrt{-4\mathbf{riro}+\mathbf{ri}^2\mathbf{Tan}[\theta]^2-2\mathbf{riro}\mathbf{Tan}[\theta]^2+\mathbf{ro}^2\mathbf{Tan}[\theta]^2}\right)\right)\right)$$
$$\left(2\mathbf{ri}^2+3\mathbf{riro}+2\mathbf{ro}^2+\frac{1}{2(-1-\mathbf{Tan}[\theta]^2)}\left(2\mathbf{riro}-\mathbf{ri}^2\mathbf{Tan}[\theta]^2-\mathbf{ro}^2\mathbf{Tan}[\theta]^2+\right.\right.$$
$$\left.\left.(\mathbf{ri}+\mathbf{ro})\mathbf{Tan}[\theta]\sqrt{-4\mathbf{riro}+\mathbf{ri}^2\mathbf{Tan}[\theta]^2-2\mathbf{riro}\mathbf{Tan}[\theta]^2+\mathbf{ro}^2\mathbf{Tan}[\theta]^2}\right)\right)\Big/$$
$$\left(\sqrt{\left(\frac{1}{-1-\mathbf{Tan}[\theta]^2}\left(2\mathbf{riro}-\mathbf{ri}^2\mathbf{Tan}[\theta]^2-\mathbf{ro}^2\mathbf{Tan}[\theta]^2+(\mathbf{ri}+\mathbf{ro})\mathbf{Tan}[\theta]\right.\right.\right.\right.$$
$$\left.\left.\left.\left.\sqrt{-4\mathbf{riro}+\mathbf{ri}^2\mathbf{Tan}[\theta]^2-2\mathbf{riro}\mathbf{Tan}[\theta]^2+\mathbf{ro}^2\mathbf{Tan}[\theta]^2}\right)\right)\right)\right)^{1/3}$$

$$\mathbf{resdistplotup[theta\_]:=Plot[resdistlargethetaup[ro,1,\theta],\{ro,romin[\theta],romin[\theta]+2000\}]}$$

```
resdistplotdown[theta_]:=Plot[resdistlargethetadown[ro, 1, θ], {ro, romin[θ], romin[θ] + 2000}]
resforcelargethetaup[ro_, ri_, theta_] =
2 * Pi(Sin[θ] * rsup[ro, ri, θ] - rsup[ro, ri, θ]^2/(ro + ri))*
(3 * vollargethetaup[ro, ri, θ]/(4 * Pi))^(-1/3);
resforcelargethetadown[ro_, ri_, theta_] =
2 * Pi(Sin[θ] * rsdown[ro, ri, θ] - rsdown[ro, ri, θ]^2/(ro + ri))*
(3 * vollargethetadown[ro, ri, θ]/(4 * Pi))^(-1/3);
θ = Pi * 179/180;
distforcelist = {};
For[ro = 1.001, ro ≤ 25 * romin[Pi - θ], ro = ro * 1.01,
distforcelist =
```

# Liquid bridge between a sphere and a plate

**Definition of parameters:**

```
PARAMETER length_max=0.005
PARAMETER length_min=0.001
PARAMETER ini_sep=0.0
PARAMETER end_sep=2.4
PARAMETER sep=ini_sep
PARAMETER sep_step=(end_sep-ini_sep)/480;
PARAMETER ini_radius=2
PARAMETER end_radius=10
PARAMETER radius=ini_radius;
PARAMETER radius_factor=1.0092529;
PARAMETER vol=4*Pi/3
PARAMETER theta=60
PARAMETER alpha=50
#define wet cos(Pi*theta/180)
#define ca cos(Pi*alpha/180)
#define sa sin(Pi*alpha/180)
```

**Definition of interfacial energies:**

```
quantity int_energy energy method edge_scalar_integral
scalar_integrand:  2*Pi*x1
quantity sub_energy_bottom energy method vertex_scalar_integral
scalar_integrand:  -wet*Pi*x1*x1
quantity sub_energy_top energy method vertex_scalar_integral
scalar_integrand:  -wet*2*Pi*(x2-sep)*radius
quantity wet_radius_bottom info_only method vertex_scalar_integral
scalar_integrand:  x1
quantity wet_radius_top info_only method vertex_scalar_integral
scalar_integrand:  x1
quantity height info_only method vertex_scalar_integral
```

```
scalar_integrand:  x2
```

**Computes volume of liquid bridge:**

```
method_instance main_volume method edge_vector_integral
vector_integrand:
q1:  0
q2:  Pi*x1*x1
q3:  0
method_instance vol_correction_top method vertex_scalar_integral
scalar_integrand:  -Pi*(x2-sep)*(x2-sep)*(3*radius-x2+sep)/3.0
quantity drop_volume fixed=vol method main_volume method vol_correction_top
```

**Constraints:**

```
constraint 1
formula:  x3=0                                          // cutting plane
constraint 2
formula:  x2=0                                          // bottom plane
constraint 3
formula:  sqrt(x1*x1+(x2-radius-sep)*(x2-radius-sep))=radius // top sphere
constraint 4 nonnegative                                  // axis
formula:  x1
constraint 5 nonnegative
formula:  x2
constraint 6 nonnegative
formula:  sqrt(x1*x1+(x2-radius-sep)*(x2-radius-sep))-radius
```

**List of vertices:**

```
vertices
1 1.5*sa*radius -1.5*(1-ca)*radius 0 constraint 1 2 4 sub_energy_bottom wet_radius_botton
2 radius 0 0 constraint 1 3 4 sub_energy_top wet_radius_top vol_correction_top height
//3 0 0 0 fixed constraint 1 2
//4 radius 0 0 fixed constraint 1 2
```

```
//5 0 0 0 fixed constraint 1 3
//6 radius radius 0 fixed constraint 1 3
//7 0 0 0 fixed
//8 5 0 0 fixed
//9 5 5 0 fixed
//10 0 5 0 fixed
```

**List of edges:**

```
edges
1 1 2 tension 0 constraint 1 4 5 6 int_energy main_volume
//2 3 4 tension 0 fixed constraint 1 2
//3 5 6 tension 0 fixed constraint 1 3
//4 7 8 fixed
//5 8 9 fixed
//6 9 10 fixed
//7 10 7 fixed

read
gv:= {
r; g;
r; g;
U;
filename :=
sprintf"/jupiter/home/souza/sp_%g_R%g.dat",
theta, end_radius;
printf"# parameter:  \n" ≫ filename;
printf"# theta:  %g \t vol:  %g \t inisep:  %g \t endsep:  %g \t radius:  %g \ n",
theta, vol, ini_sep, end_sep, end_radius >> filename; printf"# output format:  \n"
≫ filename; printf"# separation total_energy pressure beta r_min r_max r_bottom
r_top ls-area_bottom ls-area_top lv-area height total_force \n" ≫ filename; // g
250;
jjmax:=20;
```

```
jj:=0;
while(jj<jjmax) do {
g 5;
refine edges ee where not fixed and ee.length > 3*length_max;
g 5;
delete edges ee where not fixed and ee.length < 3*length_min;
jj:=jj+1;
};
while(radius<end_radius) do {
g 5;
refine edges ee where not fixed and ee.length > 3*length_max;
g 5;
delete edges ee where not fixed and ee.length < 3*length_min;
radius:=radius*radius_factor;
};
radius:=end_radius;
jjmax:=150;
jj:=0;
while(jj<jjmax) do {
g 5;
refine edges ee where not fixed and ee.length > 2*length_max;
g 5;
delete edges ee where not fixed and ee.length < 2*length_min;
jj:=jj+1;
};
while(sep<end_sep)do {
jjmax:=20;
jj:=0;
while(jj<jjmax) do {
g 5;
refine edges ee where not fixed and ee.length > length_max;
g 5;
```

```
delete edges ee where not fixed and ee.length < length_min;
jj:=jj+1;
};
jjmax:=250;
jj:=0;
prun:=0;
while(jj<jjmax) do {
g 5;
refine edges ee where not fixed and ee.length > length_max;
g 5;
delete edges ee where not fixed and ee.length < length_min;
jj:=jj+1;
prun:=prun+drop_volume.pressure;
};
rmax:=0.0;
rmin:=1000.0;
foreach vertex vv where not fixed do {
if(rmin>vv.x1) then rmin:=vv.x1;
if(rmax<vv.x1) then rmax:=vv.x1;
};
prun:=prun/jjmax;
printf"%f \t %f \t %f \t %f \t %f \t %f \t %f \t %f \t %f \t %f \t %f \t %f
\n", sep,
total_energy,
prun,
acos(1+sub_energy_top.value/(2*Pi*cos(Pi*theta/180)*radius*radius)),
rmax,
rmin,
wet_radius_bottom.value,
wet_radius_top.value,
sub_energy_bottom.value/(cos(Pi*theta/180)),
sub_energy_top.value/(cos(Pi*theta/180)),
```

```
int_energy.value,
height.value-sep,
-Pi*wet_radius_bottom.value*(wet_radius_bottom.value*prun-2*sin(Pi*theta/180))
≫ filename;
sep:=sep+sep_step;
};
};
```